

# POLITECNICO DI TORINO

## Master's Degree in Aerospace Engineering



**Politecnico  
di Torino**

Master's Degree Thesis

# Experimental analysis of linear and non-linear sloshing in cryogenic fluids with damping estimation

Supervisors

Prof. SANDRA PIERACCINI

Prof. MIGUEL ALFONSO MENDEZ

Dr. ALESSIA SIMONINI

Candidate

DOMIZIANA MENEGHELLA

APRIL 2022



# Abstract

Nowadays, the success of space activities and exploration missions is conditioned by the operation of spacecrafts in compliance with the mission specifications. In particular, the operating conditions are strongly influenced by the management of the conventional and cryogenic propellants. In the case of the upper stages of launchers and satellites, the tank with its ancillary systems is the central equipment involved in complex propellant handling operations performed in various mission phases. Consequently, the design process relies on the understanding of the propellant's behaviour inside the tank, which requires knowledge about the propellant position, its time evolving topology and thermodynamic state.

The purpose of this master thesis project is to characterize the behaviour of the liquid phase under excitation in a reservoir at saturation conditions with final application to a cryogenic system. Of particular interest is the determination of the non-linear conditions (chaos and swirling) resulting from particular external excitations and the damping measurements obtained from such conditions.

The experimental characterization is performed by optical techniques and sensors. Particle Image Velocimetry is used to characterize the transient velocity field during damping. The damping coefficients are estimated first by classic methods applied directly to the temporal evolution of the velocity field, then using decomposition methods such as the Dynamic Mode Decomposition (DMD) and Proper Orthogonal Decomposition (POD). These allow the identification of coherent structures called modes, and the related spatial and temporal structures. Depending on the decomposition used, the most relevant modes are considered according to their frequency content (DMD) or energy content (POD). A comparison with theoretical results of the damping coefficient is shown, and an interpretation of the results is given.



# Table of Contents

|   |     |
|---|-----|
| <b>List of Tables</b>   | VI  |
| <b>List of Figures</b>  | VII |
| <b>1 Introduction</b>   | 1   |
| 1.1 Framework . . . . .                                       | 1   |
| 1.2 Motivation and objectives . . . . .                       | 2   |
| <b>2 Theoretical background</b>                               | 3   |
| 2.1 State of the art . . . . .                                | 3   |
| 2.2 Theoretical background . . . . .                          | 5   |
| 2.2.1 Governing equations . . . . .                           | 6   |
| 2.3 Linearised incompressible potential flow theory . . . . . | 7   |
| 2.4 Equivalent mechanical approach . . . . .                  | 9   |
| 2.5 Theoretical model . . . . .                               | 11  |
| 2.6 Sloshing regimes . . . . .                                | 13  |
| 2.7 Scaling the problem . . . . .                             | 16  |
| 2.7.1 Scaling of equations method . . . . .                   | 17  |
| 2.7.2 Buckingham’s theorem . . . . .                          | 19  |
| <b>3 Experimental activity</b>                                | 22  |
| 3.1 Experimental methodology . . . . .                        | 22  |
| 3.1.1 PIV technique . . . . .                                 | 25  |
| 3.1.2 LEDAR technique . . . . .                               | 26  |
| 3.1.3 Dimensionless parameters . . . . .                      | 29  |
| 3.1.4 Experimental matrix . . . . .                           | 31  |
| 3.2 Experimental facility . . . . .                           | 32  |
| 3.2.1 SHAKESPARE sloshing table . . . . .                     | 33  |
| 3.2.2 Displacement sensor . . . . .                           | 35  |
| 3.2.3 Accelerometer . . . . .                                 | 35  |
| 3.2.4 Laser . . . . .   | 36  |

|          |   |            |
|----------|---|------------|
| 3.2.5    | Optics . . . . .                            | 36         |
| 3.2.6    | Camera . . . . .                            | 36         |
| 3.2.7    | Acquisition system . . . . .                | 37         |
| 3.2.8    | Particles . . . . .                         | 37         |
| 3.2.9    | Liquid . . . . .                            | 38         |
| 3.2.10   | Sloshing cell . . . . .                     | 38         |
| 3.2.11   | Cryostat . . . . .                          | 38         |
| 3.3      | Experimental procedure . . . . .            | 41         |
| <b>4</b> | <b>Data treatment</b>                       | <b>42</b>  |
| 4.1      | Image processing . . . . .                  | 42         |
| 4.2      | Post-processing . . . . .                   | 44         |
| 4.3      | Logarithmic decrement method . . . . .      | 44         |
| 4.4      | Data driven decomposition methods . . . . . | 48         |
| <b>5</b> | <b>Results</b>                              | <b>51</b>  |
| 5.1      | Test matrix . . . . .                       | 51         |
| 5.2      | Planar mode . . . . .                       | 53         |
| 5.2.1    | Damping maps . . . . .                      | 53         |
| 5.2.2    | POD . . . . .                               | 55         |
| 5.2.3    | DMD . . . . .                               | 64         |
| 5.3      | Swirl mode . . . . .                        | 66         |
| 5.3.1    | Damping maps . . . . .                      | 66         |
| 5.3.2    | POD . . . . .                               | 68         |
| 5.4      | Cryogenics . . . . .                        | 72         |
| <b>6</b> | <b>Conclusions</b>                          | <b>75</b>  |
| <b>A</b> | <b>Measurements repeatability</b>           | <b>76</b>  |
| A.1      | Planar mode . . . . .                       | 76         |
| A.2      | POD . . . . .                               | 79         |
| A.3      | Swirl mode . . . . .                        | 93         |
| A.4      | POD . . . . .                               | 94         |
|          | <b>Bibliography</b>                         | <b>101</b> |

# List of Tables

|     |  |    |
|-----|--|----|
| 2.1 | Reference parameters used for the scaling analysis . . . . .   | 17 |
| 3.1 | Particles used for the non-cryogenic experiments . . . . .   | 23 |
| 3.2 | Seeding particles in the cryogenic experiment . . . . .  | 23 |
| 3.3 | Fluid's properties . . . . .   | 29 |
| 3.4 | Dimensionless parameters . . . . .   | 30 |
| 3.5 | Tested fluids . . . . .  | 32 |
| 3.6 | Camera settings for the different experiments . . . . .  | 37 |
| 3.7 | Example of the first rows of a <code>.lvm</code> file in output from a Labview acquisition . . . . . | 37 |
| 4.1 | Calibrations . . . . .   | 44 |
| 5.1 | Tested fluids . . . . .  | 51 |
| 5.2 | Peaks in the frequency spectrum for both liquids . . . . .   | 61 |
| 5.3 | Damping ratios obtained applying POD to a single mode . . . . .                                      | 62 |
| 5.4 | Damping ratios . . . . .   | 64 |

# List of Figures

|      |   |    |
|------|---|----|
| 2.1  | Cylindrical container sketch involved in the study of the sloshing problem [22] . . . . .   | 5  |
| 2.2  | Sketch depicting how the cylindrical container is modelled using a mechanical approach . . . . .  | 9  |
| 2.3  | The red dot indicates the liquid fill ratio under exam. However in order to test the limits of the theoretical model others experimental points are verified (yellow dots) . . . . .                | 14 |
| 2.4  | Comparison between the experimental liquids, and the real one (purple line). It is evident a good agreement between Abramson’s law (continuous lines) and Utsumi’s variational method (stars) . . . | 15 |
| 2.5  | Phase diagram for different sloshing regimes . . . . .  | 16 |
| 3.1  | Snapshots of the planar mode initial transient . . . . .  | 24 |
| 3.2  | Mutual camera and sloshing cell position for the planar mode . . .  | 27 |
| 3.3  | Mutual camera and sloshing cell position for the swirl mode . . . .   | 27 |
| 3.4  | Example of Radon transform [22] . . . . .   | 28 |
| 3.5  | Final result of the LeDaR technique [22] . . . . .  | 28 |
| 3.6  | Comparison between the laboratory case and the real one in terms of Reynolds number . . . . .   | 32 |
| 3.7  | Comparison between the laboratory case and the real one in terms of Weber number . . . . .  | 33 |
| 3.8  | Tested points in Miles’ phase diagram . . . . .   | 34 |
| 3.9  | SHAKESPEARE sloshing table used at the Von Karman Institute .   | 34 |
| 3.10 | ODS measuring the sloshing table’s motion along the x-axis . . . .  | 35 |
| 3.11 | Technical drawing of the quartz sloshing cells. . . . .   | 38 |
| 3.12 | Scheme of the sloshing isothermal experiment with optical equipment. Modified sketch from ref. [25] . . . . .   | 39 |
| 3.13 | Sketch of the cryostat with the main components highlighted . . . .   | 40 |
| 3.14 | Cryostat mounted on the top of the sloshing table during the experimental cryogenic campaign . . . . .  | 40 |

|      |  |    |
|------|--|----|
| 4.1  | Cropped image to analyse the planar mode . . . . .   | 43 |
| 4.2  | Snapshots of the first time instants of $u$ and $v$ component in the planar mode . . . . .                               | 45 |
| 4.3  | Selection of the point located at $x = R/4$ . . . . .  | 46 |
| 4.4  | Temporal evolution of the velocity magnitude at the point located at $x = R/4$ . HFE7200 planar mode test 1 . . . . .    | 47 |
| 4.5  | Damping ratio calculated at point located at $x = R/4$ . HFE7200 planar mode test 1 . . . . .                            | 47 |
| 5.1  | Tested points. The HFE points implicitly indicate the tests performed with LN <sub>2</sub> . . . . .                     | 52 |
| 5.2  | Damping maps. On the left, HFE7200 test 1. On the right, water test 1 . . . . .  | 53 |
| 5.3  | Modes' amplitude . . . . .   | 55 |
| 5.4  | Spatial structures planar mode. On the left HFE7200 test 1, on the right water test 1 . . . . .                          | 56 |
| 5.5  | Spatial structures planar mode. On the left HFE7200 test 1, on the right water test 1 . . . . .                          | 57 |
| 5.6  | Temporal structures planar mode. On the left HFE7200 test 1, on the right water test 1 . . . . .                         | 58 |
| 5.7  | Temporal structures planar mode. On the left HFE7200 test 1, on the right water test 1 . . . . .                         | 59 |
| 5.8  | Temporal structures' Fast Fourier Transform planar mode. On the left HFE7200 test 1, on the right water test 1 . . . . . | 60 |
| 5.9  | Temporal structures' Fast Fourier Transform planar mode. On the left HFE7200 test 1, on the right water test 1 . . . . . | 61 |
| 5.10 | Logarithmic decrement method. On the left HFE7200 test 1, on the right water test 1 . . . . .                            | 62 |
| 5.11 | Eigenvalues in the unit complex circle . . . . .   | 65 |
| 5.12 | Snapshots of the first time instants of $u$ and $v$ component in the swirl mode . . . . .                                | 66 |
| 5.13 | Damping maps HFE7200 swirl mode . . . . .  | 67 |
| 5.14 | Modes amplitude swirl mode HFE7200 . . . . .   | 68 |
| 5.15 | Spatial structures HFE7200 swirl mode . . . . .  | 69 |
| 5.16 | Temporal structures HFE7200 swirl mode . . . . .   | 70 |
| 5.17 | Logarithmic decrement method applied to the temporal structures of HFE7200 swirl mode . . . . .                          | 71 |
| 5.18 | Spectra related to the temporal structures HFE7200 swirl mode . . . . .  | 72 |
| 5.19 | Snapshots of LN <sub>2</sub> giving in input two different signal, the planar the chaos . . . . .                        | 74 |

|      |  |    |
|------|--|----|
| A.1  | Damping maps HFE7200 planar mode, $ \vec{V} $ velocity magnitude . . .   | 76 |
| A.2  | Damping maps water planar mode, $\vec{V}$ velocity magnitude . . . . .   | 77 |
| A.3  | Modes' amplitude . . . . .   | 79 |
| A.4  | Spatial structures planar mode. On the left HFE7200 test 1, on the right HFE7200 test 2 . . . . .                          | 80 |
| A.5  | Spatial structures planar mode. On the left HFE7200 test 1, on the right HFE7200 test 2 . . . . .                          | 81 |
| A.6  | Temporal structures planar mode. On the left HFE7200 test 1, on the right HFE720 test 2 . . . . .                          | 82 |
| A.7  | Temporal structures planar mode. On the left HFE7200 test 1, on the right HFE720 test 2 . . . . .                          | 83 |
| A.8  | Temporal structures' Fast Fourier Transform planar mode. On the left HFE7200 test 1, on the right HFE7200 test 2 . . . . . | 84 |
| A.9  | Logarithmic decrement method. On the left HFE7200 test 1, on the right HFE7200 test 2 . . . . .                            | 85 |
| A.10 | Modes' amplitude . . . . .   | 86 |
| A.11 | Spatial structures planar mode. On the left water test 2, on the right water test 3 . . . . .                              | 87 |
| A.12 | Spatial structures planar mode. On the left water test 2, on the right water test 3 . . . . .                              | 88 |
| A.13 | Temporal structures planar mode. On the left water test 2, on the right water test 3 . . . . .                             | 89 |
| A.14 | Temporal structures planar mode. On the left water test 2, on the right water test 3 . . . . .                             | 90 |
| A.15 | Temporal structures' Fast Fourier Transform planar mode. On the left water test 2, on the right water test 3 . . . . .     | 91 |
| A.16 | Logarithmic decrement method. On the left water test 2, on the right water test 3 . . . . .                                | 92 |
| A.17 | Damping maps HFE7200 swirl mode, $\vec{V}$ velocity magnitude . . . .  | 93 |
| A.18 | Modes' amplitude . . . . .   | 94 |
| A.19 | Spatial structures swirl mode. On the left HFE7200 test 1, on the right HFE7200 test 2 . . . . .                           | 95 |
| A.20 | Spatial structures swirl mode. On the left HFE7200 test 1, on the right HFE7200 test 2 . . . . .                           | 96 |
| A.21 | Temporal structures swirl mode. On the left HFE7200 test 1, on the right HFE720 test 2 . . . . .                           | 97 |
| A.22 | Temporal structures swirl mode. On the left HFE7200 test 1, on the right HFE720 test 2 . . . . .                           | 98 |
| A.23 | Temporal structures' Fast Fourier Transform swirl mode. On the left HFE7200 test 1, on the right HFE7200 test 2 . . . . .  | 99 |

A.24 Logarithmic decrement method. On the left HFE7200 test 1, on the  
right HFE7200 test 2 . . . . . 100

# Chapter 1

## Introduction

### 1.1 Framework

Fluid sloshing is defined as the motion of the free liquid surface inside its partially filled when subjected to external excitations. Sloshing can be triggered by a variety of forces, including vibrations, acceleration changes, pitch, yaw, or roll motions, and so on. The prediction and the understanding of sloshing are of essential importance in the space field since the great majority of rockets has liquid-based propulsion systems. The latters are based on the release of a large amount of energy from the combustion of fuel and oxidizer. During the propelled launch phase, sloshing motion is critical because the characteristic frequencies of this phenomenon can match the resonance ones, causing increasing oscillations. The attitude control system must counteract the forces and moments created by fluid displacement on the tank.

Concerning the loss of control caused by sloshing motion, some relevant examples from previous space missions are worth mentioning. One of the most popular ones is the Apollo-11 Lunar Module in 1969. During the final seconds of the first lunar landing, the remaining propellant sloshed onto the Lunar Module, causing an oscillatory motion. This motion hampered the ability to control the module during the crucial landing manoeuvre. As the propellant level decreased to about fifty per cent, the fluid gained more space to slosh, yet retained enough mass to generate strong forces and moments, demanding harsher control requirements. As a consequence, the landing location was not the designated target one [1]. During the 60s, the Émeraude VE121, a french sounding rocket experienced three ruinous launches because of propellant sloshing due to pogo oscillation, a problem that was fixed before the fourth launch [2]. In 1957, the missile Jupiter AM1's flight was a failure due to propellant slosh bending modes induced by the steering manoeuvres of the flight trajectory. The solution to this problem involved testing several types

of baffles in a Jupiter centre section until a suitable type for both the LOX and fuel tanks was discovered [3]. A more recent case took place on March 21st, 2007. During its second flight, the SpaceX Falcon-1 launcher lost control for about 2 minutes 10 seconds into the vehicle's second stage burn and, as a result, failed to reach orbit. After investigating the mission failure, it was found that propellant sloshing caused the oscillation. LOX sloshing had been initiated by the contact during staging, specifically by the subsequent second stage "hard slew" required to restore the rocket's orientation after its Kestrel engine ignited. The LOX slosh frequency, coupled with the thrust vectoring control system, gradually amplified the vehicle's oscillations until flight control was completely lost [4].

Furthermore, liquid sloshing constitutes a problem also in the aeronautical field because it usually couples with other well-known aircraft dynamics problems. For example, the motion in wing fuel tanks couples with the wing vibration modes so as to modify the flutter characteristics [5], or even the overall aircraft dynamic stability [6].

## 1.2 Motivation and objectives

The goal of this work is to experimentally characterize the damping of liquid sloshing in the framework of space propulsion. A gravity dominated environment is simulated by the use of appropriate reservoir geometry and laboratory replacement fluids for space propellants. The main research question to which this master thesis tries to answer is "how does viscosity affect damping?". In order to make light on this question, different fluids having different viscosity are used. The selection of the fluid takes into account the fundamental dimensionless parameters that describe the damping problem for space propellants. Moreover, analytical models predicting damping rates available in literature are used as a comparison with the experimental results.

The focus is to understand the limits of theoretical models that should be able to predict a damping ratio quantifying how much damping the fluid experiences once the external excitation is stopped. The cylindrical sloshing problem's theory and the related mechanical models are outlined in chapter 2. The experimental campaign is performed in an "ad-hoc" facility described in chapter 3, together with all the instrumentation used to carry out the Particle Image Velocimetry. From the fluid velocity fields obtained as an output of the PIV technique, damping maps are assessed through the logarithmic decrement method. Moreover, two data driven decomposition methods are applied to the fluid velocity fields in chapter 4. Finally, a comparison among the results obtained from the logarithmic decrement method, the data driven decompositions and the results predicted by the theoretical model are discussed in chapter 5.

# Chapter 2

## Theoretical background

### 2.1 State of the art

Due to the increasing demand for structural reliability of liquid storage tanks during the space race in the 1960s, the National Aeronautics and Space Administration (NASA) focused its attention on liquid sloshing in space vehicles. Bauer (1964) and Abramson (1966) collected the work done up to that point regarding analytical and mechanical models to describe liquid sloshing for several container configurations [7, 8].

Regarding the existence of different sloshing regimes, Miles (1984) developed a theoretical model, suited for cylindrical containers, to study the effect of the excitation parameters in the expected fluid response [9]. The different sloshing regimes (planar, non-planar swirl, and chaotic) were found to depend on the frequency offset parameter  $\beta_i$ . This parameter is a measure of the proximity to resonance conditions and is a function of the excitation amplitude, the excitation frequency, the natural frequencies, as well as the tank radius  $\beta_i(X_0, \Omega, \omega_{mn}, R)$  [10]. The system's external excitation frequency can often reach its first natural frequency, this situation is defined as resonance. In such conditions, accurate knowledge of the first damping ratio is crucial to estimate the decay of the sloshing force and the wave height. The latter would surely lead to a more reliable tank design from a structural point of view. Both experimental and theoretical methods have been approached in the research of natural frequencies: while several experimental studies were conducted, theoretical investigations for the damping ratio have been scarce.

Concerning the experimental part, Abramson compiled a large amount of experimental data to complement and validate the theoretical models [8]. Stephens conducted a parametric experiment to determine the effects of basic variables on the first damping ratio (such as liquid depth, efflux rate, liquid amplitude, kinematic

viscosity, and tank size) [11]. The individual effects of each of the variables were experimentally investigated comparing results with the theoretical relationship for damping developed by Miles [10] and may be summarized:

- a. the first damping ratio increases when the liquid fill depth parameter is  $h/R < 1$ , instead, it is independent of  $h/R$  when  $h/R \gg 1$ ,
- b. damping increases with the kinematic viscosity,
- c. a time-variant liquid depth  $h$  does not have effects on damping,
- d. damping is independent of liquid amplitude.

Similar parametric work was conducted by Mieda [12], this time results were compared to a theoretical solution proposed by Case and Parker [13]. The experimental investigations mentioned so far are based only on upright cylindrical containers, however, Abramson has also focused his attention on compartmented cylindrical tanks [14]; in this work the effects of different compartment shapes are investigated on the damping ratio. The principal drawback of all the mentioned experimental campaigns is that a large amount of time and cost was required to perform parametric studies over a wide range of system parameters. This leads to the need for a theoretical method able to predict the sloshing damping ratio.

Moreover, slosh damping arises from a very thin viscous boundary layer. It is therefore difficult to capture the damping phenomenon by means of a CFD mesh applied over the whole fluid domain. To avoid this problem and to determine the damping ratio, Utsumi has developed a theoretical damping estimation method based on the mode decomposition approach [15]. In particular, a semi-analytical method based on a variational principle is proposed and applied to cylindrical and arbitrary axisymmetric tanks. For viscous sloshing in cylindrical tanks, several theoretical studies have been conducted by using a vector potential [13], a complex velocity [16, 17] and a stream function [18]. Theoretical studies for arbitrary axisymmetric tanks, on the other hand, are scarce.

Moreover, Hortsman has presented a new model describing gravity-capillary waves in orbitally shaken cylindrical containers which allows calculating phase shifts. The incompressible potential flow theory is applied and a set of modal equations is provided, it is complemented with viscous damping rates in order to take into account energy dissipation [19].

As previously stated, the study of liquid sloshing has significant implications not only in the space field but also in the naval and automotive one. Indeed, Zheng has conducted a study on the effect of fuel sloshing on vehicles' roll stability. The importance of this research consists in preventing traffic safety problems that tank vehicles can cause. These eventualities could have bad consequences from a safety, environmental and economic point of view. It is interesting that

in this work are presented some analytical and mechanical models able to predict sloshing [20]. Martinez has focused his research on studying fluid behaviour and understanding the damping provided by the fuel under the loading frequencies commonly experienced during driving [21]. Finally, concerning damping caused by viscous effects, Miles has analyzed the free oscillations of a slightly viscous liquid in a cylindrical tank of arbitrary cross-section. The focus is on the damping of motion caused by laminar boundary-layer friction and time-varying depth draining some liquid during the sloshing [9].

## 2.2 Theoretical background

The case under exam is a partially-filled upright cylindrical container of circular cross-section placed in a gravity dominated environment. As seen in figure (2.1), the reservoir has a radius  $R$ , a height  $H$ , and a fluid level  $h$ .

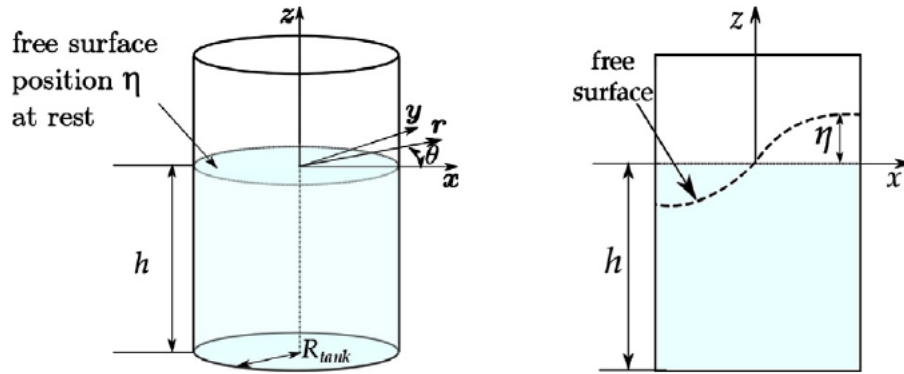


**Figure 2.1:** Cylindrical container sketch involved in the study of the sloshing problem [22]

Let us assume that this container is subjected to an harmonic lateral excitation of amplitude  $X_0$  and frequency  $\Omega$ , as a consequence its position, velocity and acceleration are respectively:

$$\begin{aligned}
 X(t) &= X_0 \sin(\Omega t), \\
 \dot{X}(t) &= X_0 \Omega \cos, \\
 \ddot{X}(t) &= -X_0 \Omega^2 \sin(\Omega t). \quad (2.1)
 \end{aligned}$$

The sloshing motion can be modelled considering an inertial reference frame in which lateral excitations are imposed through a rigid body motion. Here will be

presented the equations and the related boundary conditions essential to solving the isothermal sloshing. Usually, fluid motion problems can be solved through a set made up of three equations:

1. mass balance,
2. momentum balance,
3. energy balance.

### 2.2.1 Governing equations

In the case of isothermal sloshing, the governing equations consist only of the mass balance and the momentum balance. Moreover, both the liquid and the gas phases are considered incompressible. This means that the density is assumed to be constant  $\rho = \text{const.}$  As a consequence, the mass balance equation turns into

$$\nabla \cdot \vec{V} = \frac{\partial u}{\partial x} + \frac{\partial v}{\partial y} + \frac{\partial w}{\partial z} = 0, \quad (2.2)$$

where  $\vec{V}$  is the flow velocity vector. The momentum balance equation is derived from Newton's second law, which expresses the relationship between the momentum variation of the fluid and the sum of the external forces applied to the control volume.

$$\rho \frac{\partial \vec{V}}{\partial t} + \rho \vec{V}(\nabla \cdot \vec{V}) = -\nabla p + \nabla \cdot \tau + \rho g, \quad (2.3)$$

where  $p$  is the pressure,  $\tau$  is the shear stress tensor,  $g$  is the imposed acceleration on the fluid. The term  $\nabla p$  represents the normal stresses applied on the fluid,  $\nabla \cdot \tau$  is the viscous dissipation and  $\rho g$  represents the volume forces acting on the control volume. Considering an inertial reference frame  $\vec{g} = (0, 0, -g)^T$  this means that only the gravitational acceleration acts on the fluid domain. The shear stress tensor has the following expression considering an incompressible fluid

$$\tau = \mu[\nabla \vec{V} + (\nabla \vec{V})^T]. \quad (2.4)$$

The flow is assumed irrotational, thus  $\nabla \times \vec{V} = 0$ . The velocity field can be described using the potential function  $\nabla \Phi = \vec{V}$ . The preceding equations (which apply to both phases) must be combined with appropriate boundary conditions expressible in terms of potential function:

- no-slip conditions, that is the fluid normal velocity at the walls (bottom and lateral) must match walls' velocity itself

$$\left. \frac{\partial \tilde{\Phi}}{\partial r} \right|_{r=R} = 0, \quad \left. \frac{\partial \tilde{\Phi}}{\partial z} \right|_{z=-h} = 0, \quad (2.5)$$

- the vertical velocity of the gas and of the liquid phase at the interface  $z = \eta(r, \theta, t) = \eta(x, y, z)$  must match the free surface vertical velocity itself. This condition is known as the kinematic free-surface boundary condition and is given by the following expression

$$-\frac{\partial \Phi}{\partial z} = \frac{D\eta}{Dt} \quad (2.6)$$

where  $\eta(r, \theta, t) = \eta_0 + \tilde{\eta}(r, \theta, t)$  is the free surface elevation, with  $\eta_0$  indicating its position at rest conditions, while  $\tilde{\eta}$  is the disturbance to take into account in motion conditions. It is worth noting that this condition involves the Lagrangian derivative since the free surface elevation is a function of time  $\eta(r, \theta, t)$ .

- the pressure difference between the two phases must be balanced by the surface tension  $\sigma$ . This is guaranteed by the Young-Laplace equation

$$\Delta p = p_{liq} - p_{gas} = -\sigma \kappa,$$

where  $p_{liq}$  and  $p_{gas}$  are the liquid and the gas pressure respectively,  $\sigma$  is the surface tension and  $\kappa$  is the free surface curvature.

## 2.3 Linearised incompressible potential flow theory

The main purpose of the theory of liquid sloshing is to study the natural frequencies and the corresponding mode shapes related to sloshing. Several experiments have been conducted to find out this information. The theoretical concepts that are presented in the following chapter are based on the works of Ibrahim [23] and Miles [10]. Here are explained some basic models of liquid sloshing. Through a series of approximations, the previous equations are simplified. This theory is linearised because it is only valid for oscillations far from the resonance conditions. When the latter is achieved, the motion can become chaotic or the planar wave turns into a swirl motion. The hypothesis adopted for this theory are the following:

- the flow is assumed irrotational,

- the fluid is assumed incompressible,
- small displacements and velocities, thus velocity gradients are small,
- gravity dominated flow,
- rigid cylindrical container's walls,
- harmonic excitations  $X(t) = X_0 \sin(\Omega t)$ .

The linearised potential equation can be obtained by applying these hypotheses to (2.3)

$$\frac{\partial \Phi}{\partial t} + \frac{p}{\rho} - gz = 0. \quad (2.7)$$

The equation for the velocity potential function is given below; the complete derivation is presented in Ibrahim's work

$$\Phi(r, \theta, z, t) = \sum_{m=0}^{\infty} \sum_{n=1}^{\infty} \alpha_{mn}(t) \cos(m\theta) J_m(\lambda_{mn}r) \frac{\cosh[\lambda_{mn}(z+h)]}{\cosh \lambda_{mn}h}. \quad (2.8)$$

Where  $\alpha_{mn}$  is a time dependent coefficient to be determined from the free-surface initial conditions,  $J_m(\cdot)$  is the Bessel function of the first kind of order  $m$ ,  $\lambda_{mn} = \xi_{mn}/R$  where  $\xi_{mn}$  are the roots of  $\partial J_m(\lambda_{mn}r)/\partial r|_{r=R} = 0$ . The expression (2.8) highlights that the sloshing response is made up of an infinite sum of harmonic modes. For a cylindrical container of radius  $R$ , fill ratio  $h$  and subjected to lateral harmonic oscillations, the natural frequencies can be derived by solving the following expression

$$\omega_{mn}^2 = \left( \frac{g\xi_{mn}}{R} + \frac{\sigma \xi_{mn}^3}{\rho R^3} \right) \tanh\left( \xi_{mn} \frac{h}{R} \right). \quad (2.9)$$

In a gravity-dominated domain  $\frac{g\xi_{mn}}{R} \gg \frac{\sigma \xi_{mn}^3}{\rho R^3}$ , thus the natural frequencies are independent of the fluid properties.

$$\omega_{mn}^2 = \left( \frac{g\xi_{mn}}{R} \right) \tanh\left( \xi_{mn} \frac{h}{R} \right). \quad (2.10)$$

Moreover, if  $h/R \gg 1$  the natural frequencies become independent of this parameter too. In conclusion, for highly filled containers placed in a gravity dominated domain, the natural frequencies can be calculated as

$$\omega_{mn}^2 = \frac{g\xi_{mn}}{R}. \quad (2.11)$$

## 2.4 Equivalent mechanical approach

Several mechanical models can be adopted in order to describe the sloshing dynamics. These models approximate the oscillating bulk as spring-mass or pendulum-mass systems. Using these approximations has the advantage of including viscous effects in the sloshing response, unlike the linearised potential theory. Mechanical models consider the whole fluid mass  $m$  to be composed of a fixed mass  $m_0$  and several masses  $m_n$  that are excited during the sloshing.

$$m = m_0 + \sum_{n=1}^{\infty} m_n. \quad (2.12)$$

For the first asymmetrical sloshing mode  $m = 1$ , the  $n$  sloshing masses are a function of the geometry and the excitation conditions. Both models (spring-mass and pendulum-mass) give similar results but have different physical interpretations. It should be highlighted that these models are only valid for linear sloshing and the first asymmetrical mode  $m = 1$ .

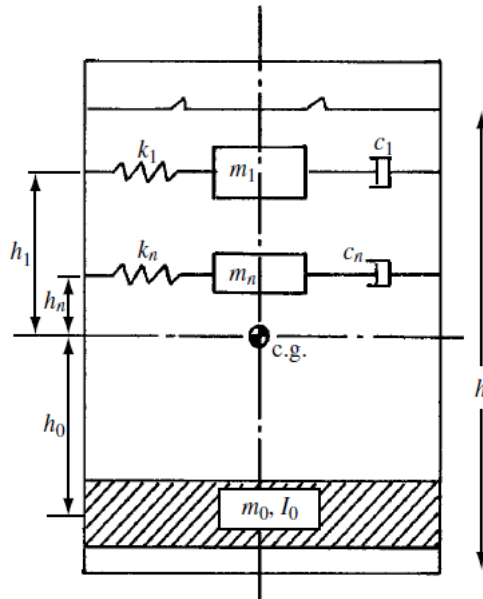


**Figure 2.2:** Sketch depicting how the cylindrical container is modelled using a mechanical approach

## SPRING-MASS MODEL

The motion is described through a second-order ODE

$$m_n \ddot{x}_n = -k_n x_n - d_n \dot{x}_n + F(t), \quad (2.13)$$

where  $k_n = m_n \omega_{1n}^2$  is the spring's stiffness,  $d_n = 2m_n \gamma \omega_{1n}$  is the damping ratio,  $\gamma$  is the damping ratio and  $F(t)$  is the external forcing, that for lateral conditions has the form

$$F(t) = m_n X_0 \Omega^2 \cos(\Omega t). \quad (2.14)$$

For the first asymmetrical mode, the damping ratio is given by an empirical relation

$$\gamma = C_1 \left( \frac{\nu}{R^{3/2} g^{1/2}} \right)^{n_1} \left( 1 + \frac{0.318}{\sinh(\xi_{1n} h/R)} \left( 1 + \frac{1 - h/R}{\cosh(\xi_{1n} h/R)} \right) \right), \quad (2.15)$$

where  $\nu$  is the kinematic viscosity,  $C_1$  and  $n_1$  are parameters depending on the problem's geometry. For a cylindrical container without baffles,  $C_1 = 0.79$  and  $n_1 = 1/2$  [8]. The solution of (2.13) is given by the superposition of the homogeneous solution  $x_{n_h}$  to the particular one  $x_{n_p}$

$$x_n(t) = x_{n_h}(t) + x_{n_p}(t). \quad (2.16)$$

The particular solution is the steady-state response to the lateral excitation that occurs after the initial transient

$$x_{n_p}(t) = \frac{X_0}{\sqrt{\left[ \left( \frac{\omega_{1n}}{\Omega} \right)^2 - 1 \right]^2 + 4\gamma^2 \left( \frac{\omega_{1n}}{\Omega} \right)^2}} \cos(\Omega t - \phi). \quad (2.17)$$

The related phase is

$$\phi = \arctan \left( \frac{2\gamma (\omega_{1n}/\Omega)}{(\omega_{1n}/\Omega)^2 - 1} \right). \quad (2.18)$$

The homogeneous solution represents the initial transient displacement. During this transient regime, the natural frequencies are excited, leading to an additional oscillatory contribution that is exponentially damped during the first moments of the motion

$$x_{n_h}(t) \propto e^{-\gamma \omega_{1n} t} \cos \left( \omega_{1n} \sqrt{1 - \gamma^2} t \right). \quad (2.19)$$

The duration of this initial transient phase depends on the damping ratio of the system and on the natural frequency being excited. After the external excitation,

when the tank is stopped, it begins the free damping condition. The fluid displacement is described by a damped oscillatory motion that satisfies (2.19). As the amplitude's motion decreases, also the free surface elevation and the sloshing force will decay following an exponential trend

$$\eta(t) \propto e^{-\omega_{1n}t} \text{ and } F_x(t) \propto e^{-\omega_{1n}t}. \quad (2.20)$$

The term ‘‘damping’’ is generally employed to describe the energy dissipation that occurs during fluid oscillations due to viscous friction. When a system oscillates in one of its natural modes with no energy input, the amplitude of successive oscillations decreases as a result of energy dissipation. The decreasing amplitude can be described by the logarithmic decrement  $\Lambda$ . This parameter measures the ratio between the peak amplitude of a signal for two sequential time periods

$$\Lambda = \ln \left( \frac{\text{Current Peak Response}}{\text{Next Peak Response}} \right). \quad (2.21)$$

Significant variables for viscous damping are:

- liquid height
- liquid kinematic viscosity
- tank size

In conclusion, the damping ratio can be indirectly measured as

$$\gamma = \frac{\Lambda}{\sqrt{4\pi^2 + \Lambda^2}}. \quad (2.22)$$

This estimation is obtained applying equation (2.19) to (2.21)

## 2.5 Theoretical model

This work focuses on the estimation of the first damping ratio because it is related to the first natural frequency, which is the most energetic one and the most likely excited. A theoretical damping estimation method based on the mode decomposition approach is presented next [15]. In particular, a semianalytical method based on a variational principle is proposed and applied to cylindrical tanks. In this study, the linear damping ratio is calculated under the following assumptions:

- the main flow is inviscid and irrotational, and therefore the damping is produced by the boundary layer,

- rigid tank,
- incompressible fluid.

This damping analysis method is based on the following principle: the time integral of the flow velocity represents a finite displacement from the equilibrium position in the fluid vibration problem and can be used to estimate the virtual work due to the Navier–Stokes equations’ viscous terms for theoretically determining the damping ratio. First of all, the modal equation for non-viscous sloshing is essential to define which are the terms involved in the damping ratio calculation. Using the variational principle it has the following expression

$$(-M_s\ddot{q} - K_s q) \delta q = 0, \quad (2.23)$$

where  $M_s$ ,  $K_s$  and  $q$  are the mass matrix, the stiffness matrix and the modal coordinate respectively. They are given by the following expressions:

$$\begin{aligned} M_s &= \rho_f \lambda_1 \tanh(\lambda_1 h) \pi \int_0^R J_1(\lambda_1 r)^2 r dr \\ &= \rho_f \lambda_1 \tanh(\lambda_1 h) \pi \frac{R^2}{2} \left(1 - \frac{1}{\lambda_1^2 R^2}\right) [J_1(\lambda_1 R)]^2, \end{aligned} \quad (2.24)$$

$$K_s = \omega^2 M_s, \quad (2.25)$$

$$\omega^2 = g \lambda_1 \tanh(\lambda_1 h), \quad (2.26)$$

where  $\omega$  is the first natural frequency of the cylindrical sloshing problem. The modal coordinates  $q$  do not describe a physical displacement, but they indicate which modes are dominant in the system. An advantage of using modal coordinates is that the mass and stiffness matrices are diagonal, in particular the stiffness matrix has on the main diagonal the eigenvalues of the problem, that are the natural frequencies squared. As a result, the expression of the first damping ratio is presented in equation (2.27). Here the definition of damping ratio is applied: it is the ratio between the damping and the critic damping ( $2\sqrt{M \cdot K}$ )

$$\begin{aligned} \zeta_d &= \frac{C_{s,R}}{2\left(M_s + \frac{1}{\omega} C_{s,I}\right)^{1/2} K_s^{-1/2}} = \frac{C_{s,R}}{2M_s^{1/2} K_s^{1/2} \left(1 + \frac{1}{\omega} \frac{C_{s,I}}{M_s}\right)^{1/2}} \\ &\cong \frac{C_{s,R}}{2(M_s K_s)^{1/2}}. \end{aligned} \quad (2.27)$$

Where  $C_{s,R}$  and  $C_{s,I}$  are the real and imaginary parts of  $C_s^{(1)} + C_s^{(2)}$  respectively, they physically represent the damping and the oscillation of the motion. They

are constants arising from the integration of the virtual work done by the viscous forces in the boundary layer. It can be shown that  $|C_{s,I}/M_s\omega| \ll 1$  by making an analysis of orders of magnitude. Introducing the following parameter as a measure of the boundary layer's thickness:

$$t_b = (\nu/\omega)^{1/2}. \quad (2.28)$$

A series of substitutions lead to this final result  $\zeta_d \propto \nu^{1/2}a^{-3/4}g^{-1/4}$ . In conclusion the damping ratio is dependent only on the geometry of the problem (tank's radius  $a$ ) and on the fluid's properties under exam (kinematic viscosity  $\nu$ ). A similar result in terms of proportionality was empirically obtained in [8] by Abramson

$$\delta_d = 0.56 \cdot 2\pi\nu^{1/2}R^{-3/4}g^{-1/4}\tanh^{-1/4}\left(1.84\frac{h}{R}\right)\left[1 + \frac{2[1 - (h/R)]}{\sinh(3.68h/R)}\right]. \quad (2.29)$$

The only difference is that here the damping ratio is rescaled by a  $2\pi$  factor to obtain the so called logarithmic decrement:  $\delta_d = 2\pi\zeta_d$ . In conclusion, the empirical result presented by Abramson can be theoretically explained through the damping analysis method proposed by Utsumi. Moreover, it is confirmed that  $|C_{s,I}/M_s\omega| \ll 1$  because through the analysis of orders of magnitude it is obtained that  $C_{s,I}/M_s\omega \propto \nu^{1/2}\omega^{-3/4}g^{-1/4}$ . This quantity is smaller than unity because the kinematic viscosity is a small number. Moreover, this ratio recalls the fourth root of the inverse of the Reynolds number. Since Reynolds numbers are of orders of  $10^2$  in the sloshing laboratory case, as will be further explained in chapter 3, it is evident that the ratio  $C_{s,I}/M_s\omega$  is much smaller than unity.

## 2.6 Sloshing regimes

According to Miles' weakly non-linear theory, the fluid response to a forced lateral motion is strongly dependent on the excitation parameters: the amplitude  $X_0$ , and frequency  $\Omega$  of the movement. Three different sloshing regimes may be observed, depending on the selection of these two parameters:

1. **linear sloshing** (planar waves): observed for low amplitudes and frequencies very far from resonance. Characterized by a steady harmonic motion where the peak wave height is constant over time. The free surface remains planar, the nodal diameter is fixed and perpendicular to the direction of excitation, and the oscillation frequency is equal to the excitation frequency. This is the regime that is characterized by potential and mechanical models outlined throughout this chapter
2. **chaotic sloshing**: typically takes place near resonance conditions. Characterized by a rotary motion that never becomes constant or harmonic. Peak

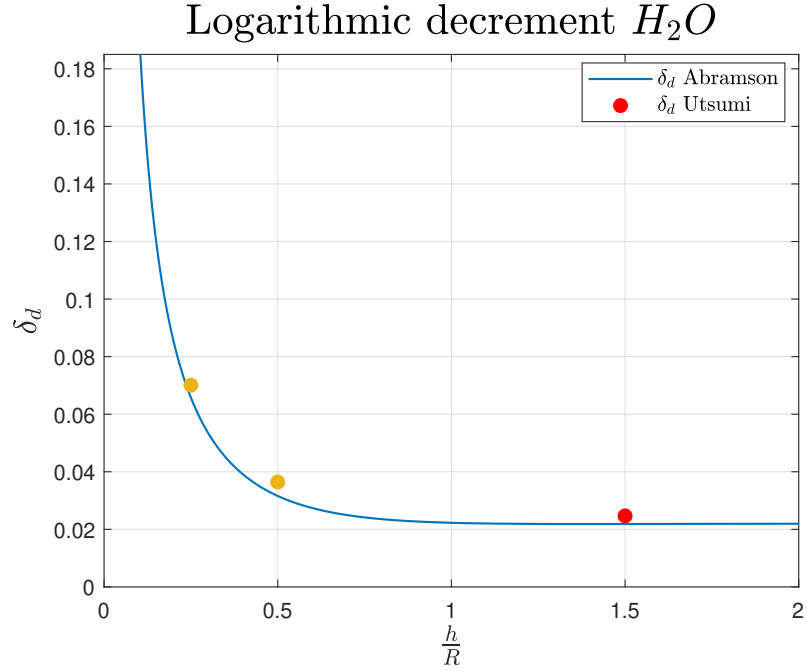


**Figure 2.3:** The red dot indicates the liquid fill ratio under exam. However in order to test the limits of the theoretical model others experimental points are verified (yellow dots)

wave height and nodal diameter change with time. Wave height increases until the moving wave's acceleration equals the gravitational forces. After wave breaking, the process restarts until the critical amplitude is reached again

3. **swirl wave:** very stable regime that typically develops when the excitation frequency is higher than resonance conditions. It is a constant rotary motion of the free surface along the axial direction. Nodal diameter rotates with constant angular velocity

For lateral sloshing, deep waters ( $h/R > 1$ ) and low damping conditions, Miles determined that the boundaries between these regimes are defined by the following equation

$$\frac{X_0}{R} = \frac{1}{1.684} \left( \frac{(\Omega/\omega_{11})^2 - 1}{\beta_i} \right)^{3/2}, \quad (2.30)$$

where  $\beta_i$  are the fixed values of the frequency offset parameter that separate the different sloshing regimes and  $\omega_{11}$  is the first natural frequency of the first asymmetrical mode  $m = 1$ ,  $n = 1$ . Figure (2.5) shows the phase diagram for

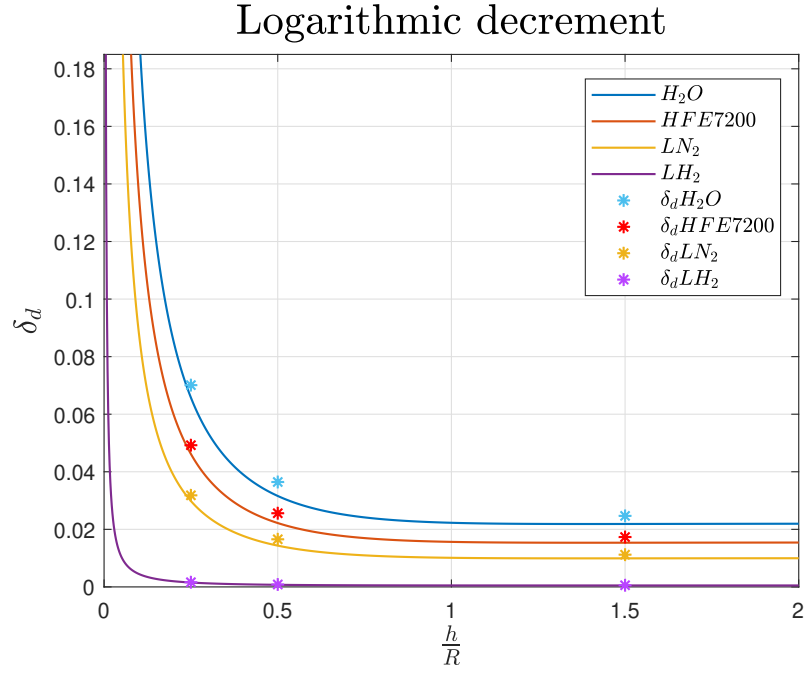


**Figure 2.4:** Comparison between the experimental liquids, and the real one (purple line). It is evident a good agreement between Abramson's law (continuous lines) and Utsumi's variational method (stars)

the different sloshing regimes that can be obtained by varying the dimensionless excitation amplitude and frequency.

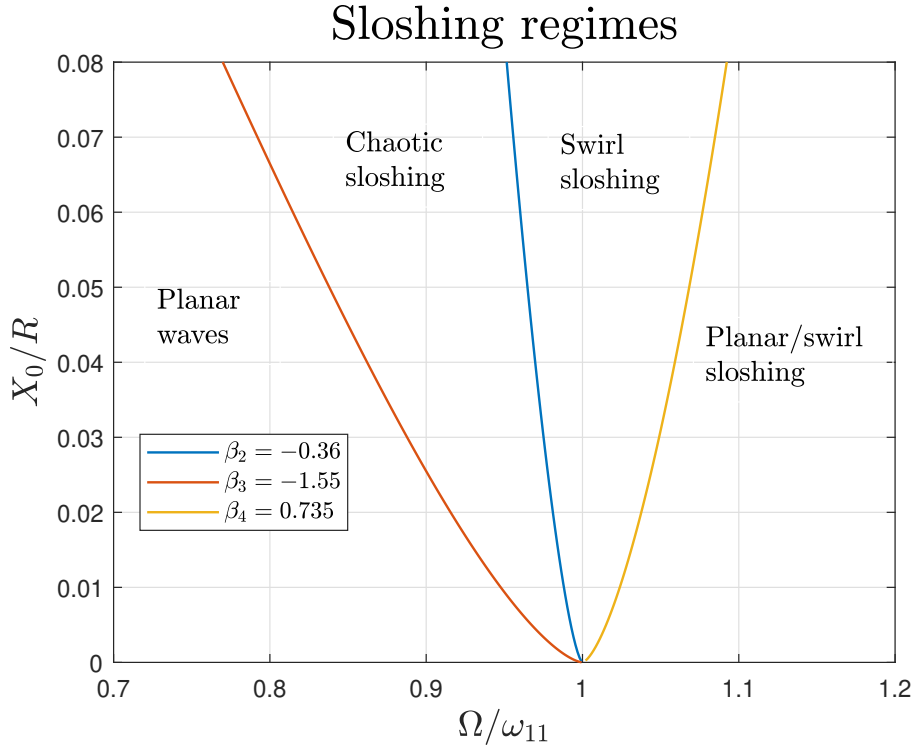


**Figure 2.5:** Phase diagram for different sloshing regimes

## 2.7 Scaling the problem

The study of a physical phenomenon involves the introduction of dimensionless parameters that describe the problem. One advantage is that through fluid dynamics similarity the full-scale problem can be studied and reproduced in the laboratory on a smaller scale, involving lower costs. The physical similarity consists of the correspondence in geometry, kinematics, dynamics, etc. Fluid dynamics similarity is assured if the dimensionless parameters are the same in the full scale and the resized problem. There are two methods that allow finding the characteristic dimensionless parameters:

1. the Buckingham's theorem,
2. the scaling of equations method.

Both methods have their drawbacks, which will be discussed and compared in the following.

### 2.7.1 Scaling of equations method

Starting from the scaling of equations method, for the isothermal case, as previously stated, both the liquid and the gas phase are considered incompressible. Thus the parameters are obtained by making the motion equations and the boundary conditions dimensionless. The following equations are dimensional, as presented in the previous chapter

$$\nabla \cdot \vec{V} = 0, \quad (2.31)$$

$$\rho \frac{\partial \vec{V}}{\partial t} + \rho \vec{V}(\nabla \cdot \vec{V}) = -\nabla p + \nabla \cdot \tau + \rho g, \quad (2.32)$$

$$\Delta p = p_{liq} - p_{gas} = -\sigma \kappa. \quad (2.33)$$

The adimensionalization consists in dividing the equation for a combination of reference quantities. The latter adopted for the isothermal case are listed in the table below (2.1).

| Physical parameters | Reference quantities    | Definition                             |
|---------------------|-------------------------|--|
| Length              | R                       | Container radius                       |
| Velocity            | $X_0 \Omega$            | External excitation velocity           |
| Time                | $R/(X_0 \Omega)$        | Length scale divided by velocity scale |
| Acceleration        | g                       | Gravitational acceleration             |
| Pressure            | $\rho_0 (X_0 \Omega)^2$ | Dynamic pressure scaling               |

**Table 2.1:** Reference parameters used for the scaling analysis

The procedure is outlined in detail below. The continuity equation can be scaled in one step

$$\nabla \cdot \vec{V}^* = 0 \quad \text{with} \quad \vec{V}^* = \frac{\vec{V}}{X_0 \Omega}. \quad (2.34)$$

For the momentum balance it is useful to consider each term separately

$$\begin{aligned} \rho \frac{\partial \vec{V}}{\partial t} \cdot \frac{\rho_0}{\rho_0} \cdot \frac{X_0 \Omega}{X_0 \Omega} \cdot \frac{R/(X_0 \Omega)}{R/(X_0 \Omega)} &\rightarrow \rho^* \frac{\partial \vec{V}^*}{\partial t^*} \rho_0 \frac{(X_0 \Omega)^2}{R}, \\ \rho \vec{V}(\nabla \cdot \vec{V}) \cdot \frac{\rho_0}{\rho_0} \cdot \frac{(X_0 \Omega)^2}{(X_0 \Omega)^2} \cdot \frac{R}{R} &\rightarrow \rho^* \vec{V}^*(\nabla^* \cdot \vec{V}^*) \rho_0 \frac{(X_0 \Omega)^2}{R}, \\ \nabla p \cdot \frac{\rho_0 (X_0 \Omega)^2}{\rho_0 (X_0 \Omega)^2} \cdot \frac{R}{R} &\rightarrow \nabla^* p^* \cdot \rho_0 \frac{(X_0 \Omega)^2}{R}, \end{aligned}$$

$$\nabla \cdot \tau = \nabla \cdot \mu[\nabla \vec{V} + (\nabla \vec{V})^T] = \mu \nabla^2 \vec{V} \cdot \frac{X_0 \Omega R^2}{X_0 \Omega R^2} \rightarrow \mu \nabla^{*2} \vec{V}^* \cdot \frac{X_0 \Omega}{R},$$

$$\rho g \cdot \frac{\rho_0}{\rho_0} \cdot \frac{g}{g} \rightarrow \rho^* g^* \rho_0 g.$$

Combining all together the previous terms one can obtain

$$\begin{aligned} \rho^* \frac{\partial \vec{V}^*}{\partial t^*} \rho_0 \frac{(X_0 \Omega)^2}{R} + \rho^* \vec{V}^* (\nabla^* \cdot \vec{V}^*) \rho_0 \frac{(X_0 \Omega)^2}{R} &= \\ &= -\nabla^* p^* \cdot \rho_0 \frac{(X_0 \Omega)^2}{R} + \mu \nabla^{*2} \vec{V}^* \cdot \frac{X_0 \Omega}{R} + \rho^* g^* \rho_0 g. \end{aligned} \quad (2.35)$$

Dividing both members for  $\rho_0 \frac{(X_0 \Omega)^2}{R}$  the equation becomes

$$\rho^* \frac{\partial \vec{V}^*}{\partial t^*} + \rho^* \vec{V}^* (\nabla^* \cdot \vec{V}^*) = -\nabla^* p^* + \frac{\mu}{\rho_0 (X_0 \Omega) R} \nabla^{*2} \vec{V}^* \cdot \frac{X_0 \Omega}{R} + \frac{g R}{(X_0 \Omega)^2} \rho^* g^*. \quad (2.36)$$

The first ratio can be indicated as  $1/\pi_1$ , the dimensionless parameter associated with it is the Reynolds number. It expresses the relationship between the inertial forces and the viscous ones. It is essential in sloshing applications because it offers an estimation of the damping that the liquid experiences during the motion inside the container

$$\pi_1 = \frac{\rho_0 (X_0 \Omega) R}{\mu}; \quad Re = \frac{\rho V L}{\mu}. \quad (2.37)$$

The second ratio can be indicated as  $1/\pi_2$ , the dimensionless parameter associated with it is the Froude number. It can be defined as the ratio of the flow inertia to the external field (for example the gravity)

$$\pi_2 = \frac{(X_0 \Omega)^2}{g R}; \quad Fr = \frac{V}{\sqrt{g L}}. \quad (2.38)$$

Finally, the dimensionless pressure boundary condition is given by

$$\Delta p \cdot \frac{\rho_0 (X_0 \Omega)^2}{\rho_0 (X_0 \Omega)^2} = \sigma \kappa \cdot \frac{R}{R} \rightarrow \Delta p^* = \frac{\sigma}{\rho_0 (X_0 \Omega)^2 R} \kappa^*.$$

The third ratio can be indicated as  $1/\pi_3$ , the dimensionless parameter associated with it is the Weber number. It is a measure of the relative importance of the

fluid's inertia compared to its surface tension. It is often useful in analysing fluid flows where there is an interface between two different fluids

$$\pi_3 = \frac{\rho_0(X_0\Omega)^2 R}{\sigma}; \quad We = \frac{\rho V^2 L}{\sigma}. \quad (2.39)$$

The scaling presented deals with the dynamics of the problem, however, also the kinematics has to be considered. In particular considering the external forcing presented in (2.1), this equation can be divided by the reference length used before, the tank radius, and a reference time  $2\pi/\omega_{11}$ . Thus the following non-dimensional expression is obtained

$$\frac{X(t)}{R} = \frac{X_0}{R} \sin\left(\frac{\Omega}{w_{11}} t^* 2\pi\right). \quad (2.40)$$

Analyzing the above expression the non-dimensional amplitude  $\frac{X_0}{R}$  and non-dimensional frequency  $\frac{\Omega}{w_{11}}$  are two non-dimensional parameters that can describe the kinematics of the problem.

In conclusion, the scaling of equations consists of adimensionalization of the equations describing the system under study. It is evident how it yields to the list of dimensionless numbers directly, the only choice consists in selecting which variable will be scaled and which will be left intact. Moreover, dimensionless equations are independent of the system units, and they apply to all physically similar systems (useful to scale up/down). However, there are also some drawbacks, such as the scaling of equation method failing to provide the relationship between dimensionless numbers, as well as the possibility of some of them being left out.

## 2.7.2 Buckingham's theorem

Buckingham's theorem allows defining the dimensionless groups of the problem through dimensional analysis. First of all, the relevant dimensional quantities for the problem have to be found

$$[R^{\alpha_1} (X_0\Omega)^{\alpha_2} \mu^{\alpha_3} \rho^{\alpha_4} g^{\alpha_5} \sigma^{\alpha_6}] = [0]. \quad (2.41)$$

In this case  $N = 6$ , that is the number of relevant dimensional quantities. In particular, they are:

- $R$  the container's radius,
- $X_0\Omega$  the velocity obtained as the, product between the external excitation's amplitude  $X_0$  and frequency  $\Omega$
- $\mu$  the fluid's dynamic viscosity in exam,

- $\rho$  the fluid's density in exam
- $g$  the gravitational acceleration, since the fluid is placed in a gravity dominated environment,
- $\sigma$  the surface tension.

The basic physical quantities in the International System are seven, however, in mechanics, they are only three: the length L, the mass M and the time T. Thus  $K = 3$  is the number of the fundamental dimensions. According to Buckingham's theorem: "if N is the number of physical dimensional quantities and K is the number of basic physical quantities, at most N-K dimensionless independent groups can be obtained". The six-dimensional quantities can be expressed as a function of the three fundamental ones in this case, yielding a maximum of three dimensionless independent groups

$$[L^{\alpha_1}(LT^{-1})^{\alpha_2}(ML^{-1}T^{-1})^{\alpha_3}(ML^{-3})^{\alpha_4}(LT^{-2})^{\alpha_5}(MT^{-2})^{\alpha_6}] = [0]. \quad (2.42)$$

Grouping together each fundamental quantity, one can obtain

$$[L^{\alpha_1+\alpha_2-\alpha_3-3\alpha_4+\alpha_5} \cdot T^{-\alpha_2-\alpha_3-2\alpha_5-2\alpha_6} \cdot M^{\alpha_3+\alpha_4+\alpha_6}] = [0]. \quad (2.43)$$

The relation (2.43) is satisfied only if each exponent expression is identically null

$$\begin{cases} \alpha_1 + \alpha_2 - \alpha_3 - 3\alpha_4 + \alpha_5 = 0 \\ -\alpha_2 - \alpha_3 - 2\alpha_5 - 2\alpha_6 = 0 \\ \alpha_3 + \alpha_4 + \alpha_6 = 0 \end{cases}$$

Since this is a linear system of three equations in six unknowns, three of them can be derived as a function of the other ones by substitution

$$\begin{cases} \alpha_1 = -\alpha_3 + \alpha_5 - \alpha_6 \\ \alpha_2 = -\alpha_3 + 2\alpha_5 - 2\alpha_6 \\ \alpha_4 = -\alpha_3 - \alpha_6 \end{cases}$$

Substituting  $\alpha_1$ ,  $\alpha_2$  and  $\alpha_4$  in (2.41) one can obtain

$$[R^{-\alpha_3+\alpha_5-\alpha_6}(A_0\Omega)^{-\alpha_3+2\alpha_5-2\alpha_6}\mu^{\alpha_3}\rho^{-\alpha_3-\alpha_6}g^{\alpha_5}\sigma^{\alpha_6}] = [0]. \quad (2.44)$$

The quantities characterized by the same exponent can be grouped together, they can be indicated as  $\pi_1$ ,  $\pi_2$  and  $\pi_3$  respectively

$$\left(\frac{\mu}{R(X_0\Omega)\rho}\right)^{\alpha_3} \left(\frac{Rg}{(X_0\Omega)^2}\right)^{\alpha_5} \left(\frac{\sigma}{R(X_0\Omega)^2\rho}\right)^{\alpha_6}. \quad (2.45)$$

Assigning the following values to the remaining unknowns, the dimensionless groups can be easily recognized: they have been already obtained in equations (2.37), (2.38) and (2.39)

$$\begin{cases} \alpha_3 = -1 \\ \alpha_5 = -\frac{1}{2} \\ \alpha_6 = -1 \end{cases}$$

It is worth noting that both methods have led to the same result. Nevertheless, the dimensional analysis doesn't follow a rigorous procedure: the choice of variables is completely subjective and needs a profound understanding of the problem. Moreover, for different choices of physical quantities, the dimensional analysis produces different dimensionless numbers. This method does not always work, and when it does, the results can be good or bad, implying that numbers may or may not have physical meaning. In conclusion, there are some problems that can't be solved by dimensional analysis, this is not a universal tool. For this reason, it is convenient to apply the scaling of equation method first, to get the proper list of dimensionless numbers, and then use dimensional analysis to find the scaling relations between them [24].

# Chapter 3

## Experimental activity

### 3.1 Experimental methodology

In this thesis the answer to the research question "how does viscosity affect damping?" is found through an experimental investigation. The effects of viscosity can be measured by computing the fluid velocity fields of the sloshing motion or detecting the level of the interface in time, with the final goal of obtaining the damping ratio. Specifically, since the studied phenomenon contemplates energy dissipation, damping is assessed by observing the decay in time of the velocity's amplitude or the interface's amplitude. The fluid velocity field and the location of the interface can be measured through two main measurement optical techniques. However, since interface visibility problems were encountered during the post-processing, the attention has been focused only on one of them: the Particle Image Velocimetry (PIV). The latter is an optical technique that records the displacement of seeding particles dispersed in the fluid under exam.

The experimental campaigns can be classified into two main categories: the cryogenic and the non-cryogenic one. Further details about the main features that distinguish one from another are provided in the following sections. The medium through which PIV technique is performed is a seeded fluid. The fluid selection is based on the calculation of the dimensionless parameters that are relevant for the sloshing problem. The most important constraint to respect is that the laboratory case should reproduce as much as possible the real one, that is a full-size tank filled with hydrogen. The reproducibility is evaluated through the kinematic and dynamic similarity between the fluids available in the laboratory and the liquid hydrogen. In the end, water, HFE7200 and liquid nitrogen were tested, however a more detailed explanation about the fluid selection is provided in section (3.1.3).

Besides the liquid, the selection of particles that act as tracers in the experiment is crucial as well. The choice is based on the tested fluid's properties in terms

of density and size of molecules. Fluorescent particles are used as tracers in the non-cryogenic experiment. Only particles that cross the laser sheet are illuminated and in turn, reflect the light. Several combinations of particles were tested in order to achieve a distribution as much as possible homogeneous. Their features are summarized in the following table (3.1).

| Particles | Portion of fluid | $\rho$     | $d$           |
|-----------|------------------|------------|---------------|
| HGMS      | Interface        | 0.83 g/cc  | 5/15 $\mu m$  |
| UVPMSBR   | Interface        | 0.995 g/cc | 45/53 $\mu m$ |
| FMR       | Bulk             | 1.3 g/cc   | 1/5 $\mu m$   |

**Table 3.1:** Particles used for the non-cryogenic experiments

The combination of Hollow Glass MicroSpheres (HGMS) for the interface and Red Fluorescent Polymer MicroSpheres (FMR) is defined as "A", while the combination of Fluorescent Red Polyethylene Microspheres (UVPMSBR) for the interface and Red Fluorescent Polymer MicroSpheres (FMR) is defined as "B". Unfortunately combination "A" turned out to be not clearly visible. For this reason, in the post-processing part, only images related to particles "B" were analysed. Figure (4.2) illustrates this situation: it compares the two combinations of particles giving the same planar signal in input. Specifically, the snapshots show the initial transient. While the FMR seeds the bulk homogeneously in both cases, the interface is differently reproduced depending on the particles' diameter. The HGMS, in particular, create a recirculation bubble during some moments of the initial transient, which causes undesired noise in the post-processing phase. The UVPMSBR, on the other hand, can accurately reproduce the interface displacement.

For the cryogenic experiment, just one combination of particles was tested, following always the criteria outlined above from a fluid dynamical point of view. The particles' main features are summarized in table (3.2).

| Particles | Portion of fluid | $\rho$    | $d$          |
|-----------|------------------|-----------|--------------|
| HGMS      | Interface        | 0.83 g/cc | 5/15 $\mu m$ |
| HGMS      | Bulk             | 0.79 g/cc | 5/20 $\mu m$ |

**Table 3.2:** Seeding particles in the cryogenic experiment

Since this work is primarily oriented toward the study of linear and non-linear sloshing, the attention is focused on the planar and swirl regimes. They are experimentally tested selecting a point for each regime in Mile's phase diagram that corresponds to a specific dimensionless external amplitude and frequency. Combining all together the experimental points, the test matrix is built. For each tested point an external sinusoidal excitation is imposed through a shaking table

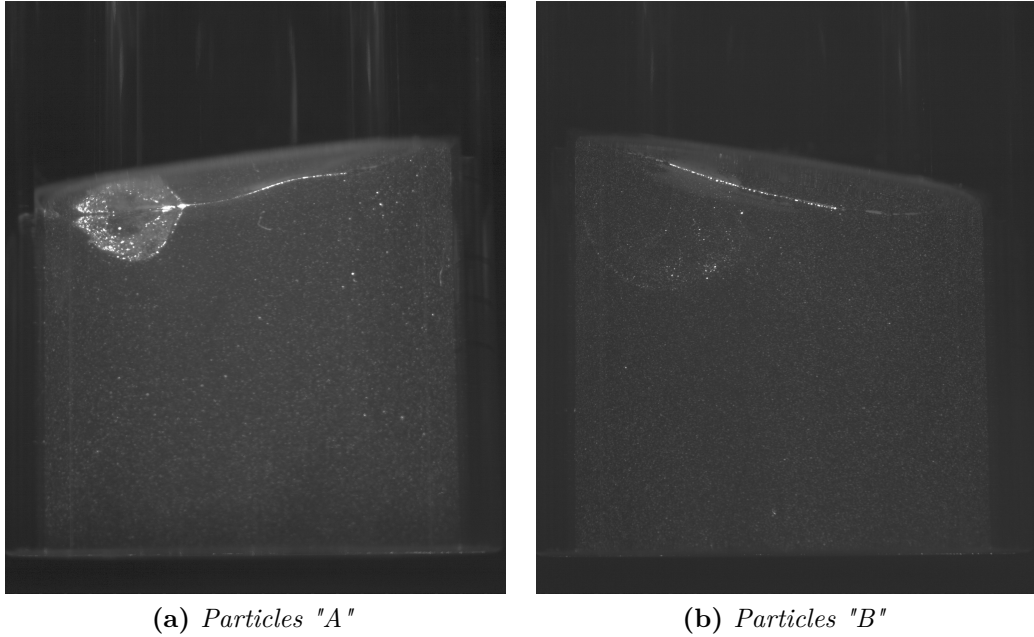


**Figure 3.1:** Snapshots of the planar mode initial transient

that allows the recreation of external sinusoidal excitation characterised by imposed amplitude and frequency, and the optical techniques illustrated in sections (3.1.1) and (3.1.2) are put into practice. The raw output of both techniques is white dotted images with a black background. The physics behind the sloshing motion can be understood by post-processing these images with appropriate tools. The fluid velocity field can be reconstructed through the PIV technique, in particular for damping estimation only the initial transient and the final damping are studied. However, due to frequencies overlapping issues in the initial transient, the attention has been focused on the final damping. The entire experimental campaign is recorded, but analysing the trigger signal from the camera it is possible to identify the specific time instants in which the initial transient and final damping occur. Once the time history of the fluid velocity field is reconstructed, damping is assessed by observing the decay in time of velocity's amplitude and finally, a damping map describing the decay rate over the fluid domain is obtained. In conclusion, these are the summarised steps describing how the experimental activity was articulated to find an answer to the initial research question. Further details about the tools used in terms of experimental techniques, the set-up, and the procedure are provided in the following sections.

### 3.1.1 PIV technique

PIV is an optical non-intrusive technique that allows the assessment of both instantaneous and mean velocity field of particles dispersed in a gaseous or liquid flow, characterized by a large amount of vectors. One or more cameras can be involved (double frame or High Speed), as well as a laser (pulsed or continuous) to take images of the particles flow at two consecutive time steps. These images are then split into a large number of Interrogation Areas (IA) and the particle displacement vector for each IA is computed by means of cross-correlation techniques. The obtained displacement vector is then divided by the time separation between two images to obtain the corresponding velocity. The PIV technique used for this experimental campaign is defined *time resolved*, meaning that images are recorded at a constant frame rate and that the  $i^{th}$  instantaneous velocity field is generated by cross-correlating the image  $i + 1$  with the image  $i$ . The laser source emits light continuously, for this reason, the experimental set-up does not need a system that synchronizes the acquisition of the camera with the laser's pulse. The choice of particles in terms of density and characteristic size is very important because it determines their ability to follow the flow field of the medium in which they are dispersed. Indeed, the relaxation time, being the lag between the particles motion and the fluid motion, is calculated including the density and the diameter of the particles. The relaxation time of the particle must be small compared to the characteristic time of the system. The ratio of these two information leads to the Stokes number, a dimensionless number characterising the behavior of particles suspended in a fluid flow. This is

$$St = \frac{t_p}{t_0} \ll 1,$$

where  $t_p$ : relaxation time, that is the reaction time of the particle moving under the action of the viscous forces

$$t_p = \frac{D_p^2 \rho_p}{\mu_f},$$

and  $t_0$ : characteristic time of the motion field, defined as the ratio between the reference length (the cylinder's radius in this case) and the characteristic velocity  $X_0 \Omega$

$$t_0 = \frac{R}{X_0 \Omega}.$$

A too high Stokes number means that particles have a lot of inertia, hence it is studied their dynamics rather than the dynamics of the flow, therefore they are not good tracers. The mean displacement of the particles is directly correlated to the

$\Delta t$  between one instant and the next one. This displacement must not be too small otherwise there is a risk of making a too large error, but the displacement must also not be too large otherwise it is not possible to carry out the correlation operation. This latter provides a measure of the most likely displacement of the particle. Another important aspect is the number of particles that have to be seeded in the liquid. A large number of particles is required to statistically describe the fluid velocity field in detail (high spatial resolution). Given that the rule of thumb for the minimum IA states that it should contain a minimum of 8-10 particles, the density of particles determines the spatial resolution of the PIV measurement.

The results are the PIV images, consisting of white dotted images with black backgrounds, and containing a certain light intensity distribution. Finally, the PIV technique set-up carried out in this case is defined as "2D2C" because the portion of field measured is a plane (two-Dimensional) and the velocity components that can be obtained are two (two-Components), in particular the ones that belong to the measurement plane. From PIV images, instantaneous planar fluid velocity fields can be extracted in terms of  $u$  and  $v$  components. These fields can be extremely useful in the determination of the damping ratio. In particular, selecting a point in the field of motion, the time evolution of both velocity components is extracted. Since the free damping oscillations are observed, the velocity signal will decay in time. The damping ratio can be calculated as the slope of linear fitting interpolating peaks, normalised with their maximum value. Depending on which sloshing regime is studied, the mutual position of the laser and the camera change with respect to the cylinder. The planar mode presents the most interesting features in the  $(x, z)$  plane, for this reason, the laser illuminates the cylinder's diametral plane and the camera is placed perpendicularly to it, as figure (3.2) shows. Conversely, the swirl mode is characterised by a rotary motion of the free surface, the most interesting features can be captured on the  $(x, y)$  plane. This time the laser illuminates the cylinder's transversal plane and the camera is above the cylinder, orthogonal to the laser sheet, as depicted in figure (3.3).

### 3.1.2 LEDAR technique

LeDaR is an acronym for Level Detection and Recording technique, it is used to characterize the liquid/gas interface, providing a high-accuracy detection of the interface in terms of location.

Particles floating at the liquid/gas interface form a visible bright line when illuminated by the laser sheet. In order to detect this bright-line an algorithm based on the Radon transform is used. This algorithm integrates the intensity values of the pixels belonging to a line positioned with an offset  $r$  with respect to a parallel line passing through the centre of the image and with a certain inclination  $\theta$ . The integration is performed for all the possible offsets  $r$  and for all the possible

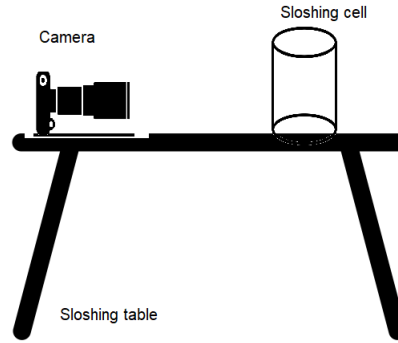


**Figure 3.2:** Mutual camera and sloshing cell position for the planar mode

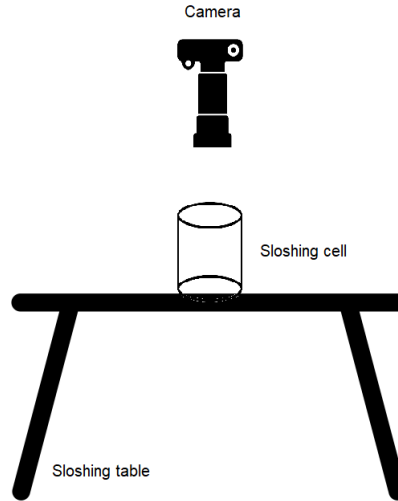


**Figure 3.3:** Mutual camera and sloshing cell position for the swirl mode

inclinations  $\theta$ . If  $f(x, y)$  is the image intensity function, then its Radon transform  $Rad(\theta, r)$  can be defined as:

$$Rad(\theta, r) = \iint f(x, y) \delta_{Dirac}(r - x \cos \theta - y \sin \theta) dx dy \quad (3.1)$$

where  $\delta_{Dirac}(r - x \cos \theta - y \sin \theta)$  is the Dirac delta function which forces the integration of  $f(x, y)$  along the direction specified by  $(r - x \cos \theta - y \sin \theta)$ . An example of how Radon transform operates is shown in figure(3.4)

The images recorded to determine the liquid/gas interface are constituted by a large number of particles, some of which belong to the bulk instead of to the interface itself or appear above the interface due to mirroring effects. A `Matlab` code has been developed based on the Radon transform:

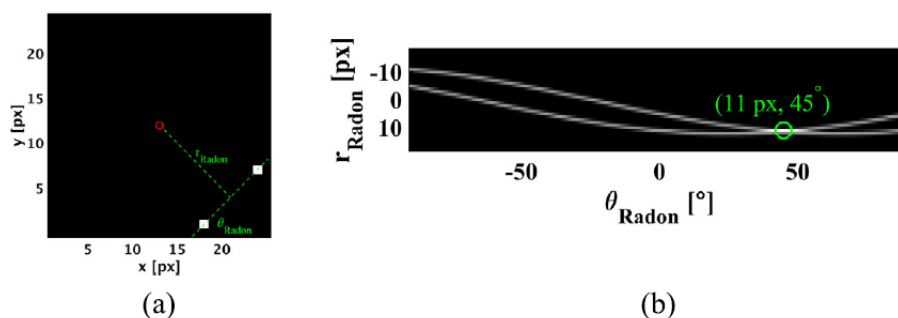


**Figure 3.4:** Example of Radon transform [22]

- first of all, the image is cropped at the interface itself, avoiding reflections in the Region Of Interest (ROI) and reducing computational time
- the image is normalized and a high pass filter is applied in order to remove background noise
- the image is split into windows with a fixed overlap
- the radon transform is performed in each window and its maximum is extracted, corresponding to the direction of the most aligned particles in the window
- the middle point of each segment obtained by means of the Radon transform is selected
- all the middle points detected are filtered in order to remove outliers, using the deviation from the median value as threshold
- finally, the remaining points are fitted by a sum of 8 sinusoids

The output of the Matlab code is shown in figure (3.5)

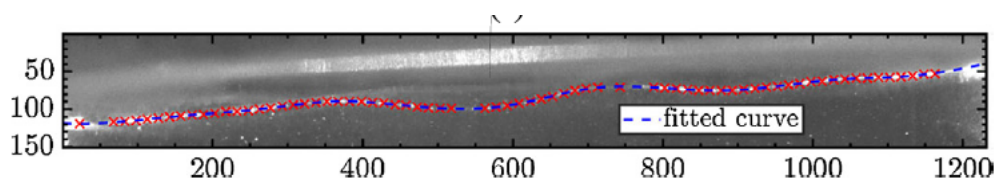


**Figure 3.5:** Final result of the LeDaR technique [22]

This detection technique is quite robust for instantaneous measurements when floating particles are in sufficient number and clearly visible. Indeed, the contrast of the images has to be enhanced in order to distinguish the particles by the

background noise. Unfortunately, the interface wasn't clearly detectable during the whole recording campaign. For this reason, LeDaR technique has been put into practice with previous experimental campaigns, as an exercise. LeDaR results could have also been useful to extract damping information studying the interface amplitude's temporal evolution.

### 3.1.3 Dimensionless parameters

In chapter 2 a scaling of the problem analysis was conducted applying two different methods. The advantages and disadvantages of both of them were explained, and in conclusion, three dimensionless parameters were found fundamental to describe the sloshing problem under exam: the Reynolds number, the Froude number and the Weber number. In order to investigate if the sloshing cell filled with replacement fluids (laboratory case) can reproduce a full-size cryogenic tank (real case), these numbers were calculated for:

- four points selected in Miles' phase diagram
- different kinds of fluids, specifically liquid nitrogen, water, HFE and ethanol for the laboratory case and liquid hydrogen for the real one.

In reference to expressions (2.37, 2.38, 2.39) it can be noticed that the three numbers essentially depend on:

1. fluid's properties under exam ( $\rho, \mu, \sigma$ )
2. tank's geometry (R)
3. external excitation parameters ( $X_0, \Omega$ )

In table (3.3) the fluid properties used to calculate the dimensionless number of table (3.4) are reported.

| Fluid property  | $T_{ref}$ | $\rho$               | $\nu$               | $\sigma$ | $C_p$   | $k$    | $\alpha$            | $\beta$  |
|-----------------|-----------|----------------------|---------------------|----------|---------|--------|---------------------|----------|
| Unit of measure | [K]       | [kg/m <sup>3</sup> ] | [m <sup>2</sup> /s] | [N/m]    | [J/kgK] | [W/mK] | [m <sup>2</sup> /s] | [1/K]    |
| $LH_2$          | 20.6      | 70.58                | 1.85E-07            | 1.91E-03 | 9904.7  | 0.104  | 1.49E-07            | 0.016    |
| $LN_2$          | 77        | 807.69               | 2.02E-07            | 8.96E-03 | 2039.8  | 0.147  | 8.90E-08            | 0.006    |
| HFE7200         | 293.15    | 1433.9               | 4.83E-07            | 0.014    | 1213.4  | 0.067  | 3.85E-08            | 1.58E-03 |
| $H_2O$          | 293.15    | 997.78               | 9.79E-07            | 0.073    | 4076.4  | 0.598  | 1.49E-07            | 3.41E-03 |
| Ethanol         | 293.15    | 789.4                | 1.50E-06            | 0.022    | 2510    | 0.171  | 21933               | 0.040    |

**Table 3.3:** Fluid's properties

Analysing table (3.4) the kinematic similarity is imposed by selecting the excitation parameters ( $X_0$  and  $\Omega$ ) such that the sloshing regime is the same in the

| Dimensionless parameter | Case | $H_2O$   | Ethanol  | HFE7200  | $LN_2$   | $LH_2$   |
|-------------------------|------|----------|----------|----------|----------|----------|
| Re                      | A    | 1.32E+02 | 8.62E+01 | 2.68E+02 | 6.41E+02 | 2.47E+05 |
|                         | B    | 1.52E+02 | 9.92E+01 | 3.08E+02 | 7.37E+02 | 2.84E+05 |
|                         | C    | 1.67E+02 | 1.09E+02 | 3.38E+02 | 8.09E+02 | 3.12E+05 |
|                         | D    | 1.82E+02 | 1.19E+02 | 3.68E+02 | 8.82E+02 | 3.40E+05 |
| Fr                      | A    | 5.16E-03 | 5.16E-03 | 5.16E-03 | 5.16E-03 | 5.16E-03 |
|                         | B    | 5.94E-03 | 5.94E-03 | 5.94E-03 | 5.94E-03 | 5.94E-03 |
|                         | C    | 6.52E-03 | 6.52E-03 | 6.52E-03 | 6.52E-03 | 6.52E-03 |
|                         | D    | 7.10E-03 | 7.10E-03 | 7.10E-03 | 7.10E-03 | 7.10E-03 |
| We                      | A    | 5.73E-03 | 1.47E-02 | 4.28E-02 | 3.77E-02 | 3.86E+01 |
|                         | B    | 7.57E-03 | 1.95E-02 | 5.67E-02 | 4.99E-02 | 5.11E+01 |
|                         | C    | 9.13E-03 | 2.35E-02 | 6.83E-02 | 6.01E-02 | 6.16E+01 |
|                         | D    | 1.08E-02 | 2.79E-02 | 8.10E-02 | 7.13E-02 | 7.31E+01 |

**Table 3.4:** Dimensionless parameters

experimental case and in the real one. This is achieved by guaranteeing that the frequency offset parameter is the same in both facilities. This concept is evident reworking expression (2.30)

$$\beta = \frac{\left(\frac{\Omega}{\omega_{11}}\right)^2 - 1}{\left(1.684\frac{X_0}{R}\right)^{2/3}} \quad (3.2)$$

Meaning that the dimensionless excitation amplitude and frequency, have to be imposed and fixed between the real and the experimental case. The corresponding dimensional quantities can be determined as a consequence

$$X_0 = \underbrace{\left(\frac{X_0}{R}\right)}_{\text{const.}} R \quad \text{and} \quad \Omega = \underbrace{\left(\frac{\Omega}{\omega_{11}}\right)}_{\text{const.}} \omega_{11} \quad (3.3)$$

Moreover, considering expression (2.10) of the natural frequency calculated for the cylindrical sloshing problem, in normal gravity condition and for deeply filled tanks  $h/R \gg 1$ , the first natural frequency can be approximated as  $\omega_{11} \simeq \sqrt{\frac{g}{R}}$ . Thus the excitation velocity can be calculated as

$$X_0 \Omega \sim \underbrace{\left(\frac{X_0}{R}\right) \left(\frac{\Omega}{\omega_{11}}\right)}_{\text{const.}} \cdot \sqrt{gR} \quad (3.4)$$

Thus dimensionally  $[X_0\Omega] \sim \sqrt{gR}$ . In conclusion, for gravity dominated sloshing, the velocity is independent of the external excitation. Considering the expression of the Froude number for the cylindrical sloshing problem (2.38), it is evident that the Froude number is always preserved between the real and laboratory sloshing facility, as long as the dimensionless excitation parameters are kept constant, this guarantees that the relative importance of inertia and volume forces in the fluid is the same. The dynamic similarity is guaranteed only if all dimensionless numbers are the same for both facilities. Analysing the Reynolds and the Weber number, it is evident that they depend on the tank's geometry and on the fluid's properties. Since the container dimensions are fixed, the similarity between the experimental and the real case can be guaranteed only by selecting the experimental fluids adequately. Considering the Reynolds number in the dimensionless parameters table (3.4) as well as in figure (3.6), it can be noticed that it differs by three orders of magnitude considering the real case and the selected replacement fluids. This difference suggests that damping is stronger in the experimental sloshing cell because the Reynolds number is three orders of magnitude lower than the real case, hence the viscous forces are prevalent in the experimental case. Comparing Weber numbers' orders of magnitude in table (3.4) and in figure (3.7), it is evident that in the experimental case it is three orders of magnitudes inferior to the real case: this means that surface tension effects are prevalent in the experimental sloshing cell. However, since the tank's diameter is much bigger than the capillary length of the problem, surface tension should play a negligible role. In conclusion, most of the time perfect similarity cannot be guaranteed; so even if numbers have very different order of magnitudes, what matters is that they belong to the same regime. Keeping in mind all these considerations about the potential replacement fluids, in the end, water, HFE7200 and liquid nitrogen were selected, because the related dimensionless parameters guaranteed a reliable reproduction of the regime under exam.

### 3.1.4 Experimental matrix

The tested sloshing excitations are summarized in Table (3.5) and Figure (3.8). It is desirable to test excitations in the three main sloshing regimes according to Mile's weakly non-linear theory: planar, chaotic and swirl waves. As a result, one point is chosen to test each regime. The definition of these points is based on the non-dimensional excitation amplitude  $X_0/R$  and frequency  $\Omega/\omega_{11}$ . However, the chaotic mode can be difficult to study by means of a 2D PIV technique, the analysis mainly focuses on the planar and swirl mode.

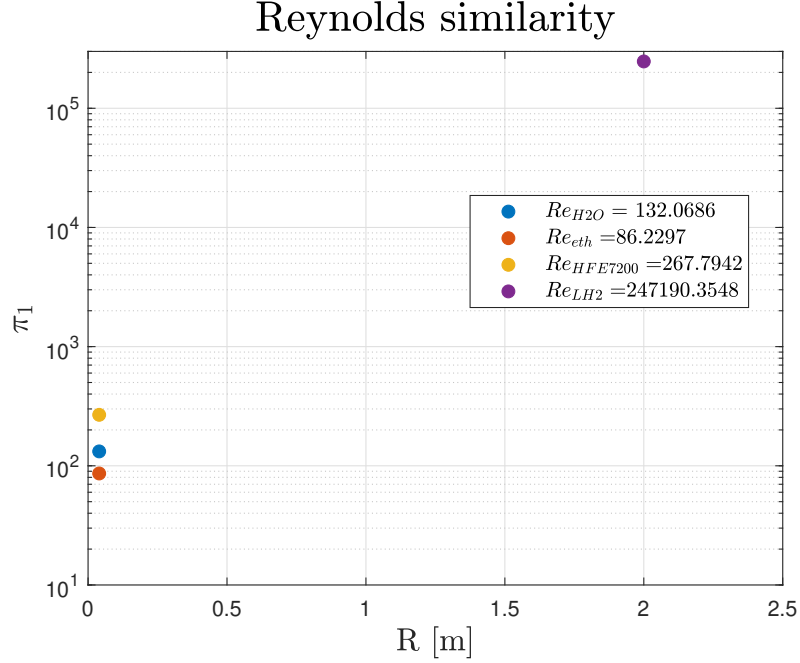


**Figure 3.6:** Comparison between the laboratory case and the real one in terms of Reynolds number

| Fluids  | Regime | $X_0/R$ | $\Omega/\omega$ | $X_0$ [mm] | $f_{ext}$ [Hz] |
|---------|--------|---------|-----------------|------------|----------------|
| HFE7200 | Planar | 0.03    | 0.8             | 1.2        | 2.7            |
|         | Swirl  | 0.03    | 1.01            | 1.2        | 3.4            |
| Water   | Planar | 0.025   | 0.89            | 1          | 3              |
| $LN_2$  | Planar | 0.03    | 0.8             | 1.2        | 2.7            |
|         | Swirl  | 0.03    | 1.01            | 1.2        | 3.4            |

**Table 3.5:** Tested fluids

## 3.2 Experimental facility

In this section, the experimental facility including all the instrumentation used is described. The same kind of experiment is performed with both non-cryogenic and cryogenics fluids. Given the particular thermal requirements needed for cryogenic liquids, the two kinds of fluids are tested in two different facilities. The two experiments have in common most of the instrumentation, such as the sloshing table (3.2.1) to provide external excitations with imposed frequencies, the optical displacement sensor (3.2.2) to detect the imposed displacements, the accelerometer (3.2.3) to measure the related accelerations, the laser (3.2.4) to illuminate the field

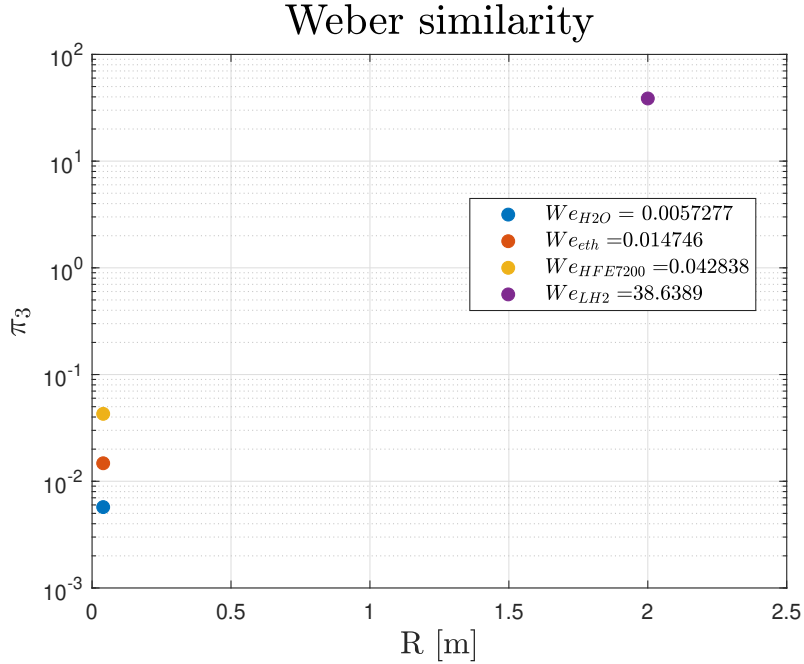


**Figure 3.7:** Comparison between the laboratory case and the real one in terms of Weber number

of motion to study, the optics (3.2.5) to obtain a laser sheet and the camera (3.2.6) to record the experimental campaign. The two experiments differ for the kind of the tested fluid, cryogenic or non-cryogenic (3.2.8), the seeded particles (3.2.7) which are chosen to be good tracers based on the properties of the tested fluid, and the container. In the non-cryogenic experiment, it is used a simple quartz cell (3.2.9), while in the cryogenic one it is used a cryostat, whose details are illustrated in section (3.2.10).

### 3.2.1 SHAKESPEARE sloshing table

The experimental isothermal sloshing measurements are performed in the SHAKESPEARE sloshing table, shown in Figure (3.9). The facility has been named SHAKESPEARE from the acronym: SHaking Apparatus for Kinetic Experiments of Sloshing Projects with EArthquake REproduction. The tabletop has dimensions of 1.5 m  $\times$  1.5 m. This facility contains three sliding modules, one for each axis, which allow for the recreation of sloshing excitations in all three directions with controlled amplitudes and frequencies.

Since this work focuses on lateral sloshing excitations, displacements are only imposed along the shaking table's x-axis. The displacements are imposed according

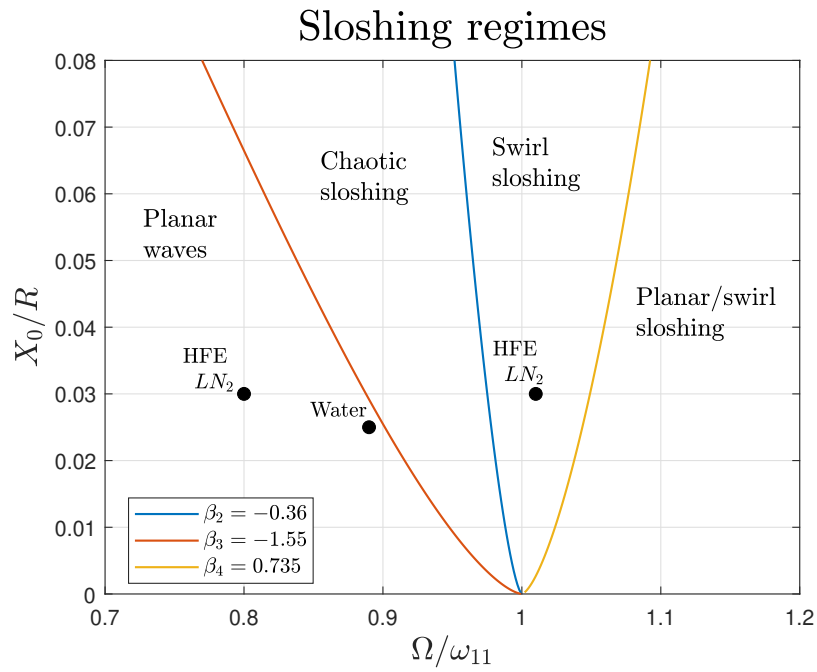


**Figure 3.8:** Tested points in Miles' phase diagram



**Figure 3.9:** SHAKESPEARE sloshing table used at the Von Karman Institute

to equation (3.5).

$$X(t) = X_0 \sin(\Omega t) \tag{3.5}$$

The imposed external excitation is sinusoidal because this kind of signal allows the selection of well-defined frequencies. Moreover, it is lateral because in this way the fluid mass centre of gravity can be moved from its equilibrium position. The effects of this shift are studied in particular for the most likely excited mode, that is the first asymmetric one.

### 3.2.2 Displacement sensor

The sloshing table's displacements are detected by the ODS, Optical Displacement Sensor. The measuring range of this sensor is  $28 - 32 \text{ mm}$  and the corresponding output is  $1 - 9 \text{ V}$ , which refers to the minimum and maximum measurable displacement. Moreover, this sensor allows verifying that the displacement input inserted in the sloshing table's control system is correct. In figure (3.10) is shown its location: along the x-axis of the sloshing table, fixed through a BOSCH profiles structure.



**Figure 3.10:** ODS measuring the sloshing table's motion along the x-axis

### 3.2.3 Accelerometer

A triaxial variable capacitance accelerometer is used, in particular it is placed such that it is solidal to the reservoir. It can measure the accelerations arising from the imposed external excitations at the same time along the three Cartesian directions. Computing the Fast Fourier Transform of the signal detected by the accelerometer the user can verify if the peak in the FFT corresponds to the imposed frequency in the external signal.

### 3.2.4 Laser

A CW laser is used to light up the seeding particles contained in a portion of the field of motion. The laser source emits a green monochromatic and coherent light beam, meaning that it has only one wavelength  $\lambda = 532 \text{ nm}$  and it is concentrated in a small spatial region. The beam power is  $P = 0.8 \text{ W}$

### 3.2.5 Optics

The optical set-up has the function to transform the laser beam into a very thin sheet, in this way the beam becomes coherent and planar. In particular, two different kinds of lenses are used:

- the spherical one focuses the beam at his focal distance
- the cylindrical one diverge the beam into a sheet

The combination of the spherical lens and the cylindrical one realises a laser sheet of a thickness below  $1 \text{ mm}$ . The laser sheet must be centred as much as possible with respect to the sloshing cell. Moreover, the optical set-up includes also a prism that deflects the beam from the x-direction to the z-direction.

### 3.2.6 Camera

The camera is the component responsible for capturing the particles' position in the motion field and in time. A CCD camera is placed perpendicularly to the plane of illumination. The main features of the camera are:

- the number of bits, it gives an idea of how many different gray levels the camera is able to discern  $2^N = \# \text{ gray levels}$ . In this case  $N = 8 \text{ bits}$
- the pixel size  $5.5 \mu\text{m}$ . The camera sensor consists of a matrix divided into rows and columns, usually, the single pixels are square and the single-pixel size is  $5.5 \mu\text{m}$ . Multiplying the pixel size by the number of rows and columns of the matrix (camera resolution) the physical dimensions of the sensor is obtained. The pixel size is important for achieving high spatial resolution.

The camera settings used to record images for each experiment are summarized in table (3.6).

A 60 mm Macro Nikkor objective was mounted on the camera, and the maximum aperture was settled ( $f/2$ ). In order to measure efficiently, further light sources have to be shielded, otherwise, they would pollute the images. Therefore the experiment region is covered with a black sheet.

| Experiment         | Cryogenic   | Non-cryogenic |             |             |
|--------------------|-------------|---------------|-------------|-------------|
| Fluid              | LN2         | H2O           | HFE7200     |             |
| Regime             | Planar      | Planar        | Planar      | Swirl       |
| Frame rate [Hz]    | 100         | 75            | 100         | 75          |
| Exposure time [ms] | 1000        | 2000          | 1000        | 2000        |
| FOV [px × px]      | 3072 × 2592 | 3072 × 2592   | 3072 × 2592 | 2800 × 2800 |
| Lens aperture      | f/2         | f/2           | f/2         | f/2         |
| Camera lens [mm]   | 60          | 60            | 60          | 60          |

**Table 3.6:** Camera settings for the different experiments

### 3.2.7 Acquisition system

The ODS, the accelerometer and the camera are all connected to an acquisition system called DAQ (Data Acquisition) with acquisition cards from National Instruments. Instead, LabVIEW is the system design software designed specifically for developing test, measurement, and control applications with quick access to hardware and results. It provides in output a `.lvm` file in which each column reports the signal coming from a different instrument. Specifically the following quantities are reported: the time acquired according to the user-defined sampling frequency, the trigger signal from the camera, the displacement detected by the ODS and the acceleration measured along the three axes. In addition, another software called Streampix is used to record images. Here the user can decide the camera settings previously illustrated in table (3.6).

| t [s]    | Camera [V] | ODS [V]  | $a_x$ [V] | $a_y$ [V] | $a_z$ [V] |
|----------|------------|----------|-----------|-----------|-----------|
| 0.000000 | 5.370629   | 5.241275 | -0.230277 | 1.953418  | -0.001654 |
| 0.001000 | 5.370629   | 5.240959 | -0.235377 | 1.953101  | -0.002292 |
| 0.002000 | 5.370629   | 5.240011 | -0.232189 | 1.955947  | -0.001654 |
| 0.003000 | 5.370629   | 5.241907 | -0.231552 | 1.954998  | -0.001017 |
| 0.004000 | 5.370629   | 5.245701 | -0.233783 | 1.952785  | -0.002929 |
| 0.005000 | 5.370629   | 5.244752 | -0.231552 | 1.953734  | -0.003248 |

**Table 3.7:** Example of the first rows of a `.lvm` file in output from a Labview acquisition

### 3.2.8 Particles

The criteria followed in the selection of the particles has been already explained in the experimental methodology. The kind of tracers changes according to the tested

fluid's properties in terms of density and size of molecules, in this way it is studied the dynamic of the flow rather than the dynamic of the particles.

### 3.2.9 Liquid

Three kinds of liquids are employed and compared in this experiment:

- water
- HFE7200, an engineering fluid
- liquid nitrogen

### 3.2.10 Sloshing cell

The sloshing cell used in this project is a quartz rectangular cuboid with dimensions  $100\text{ mm} \times 100\text{ mm} \times 134\text{ mm}$  in which a cylindrical hole with diameter  $D = 80\text{ mm}$  is drilled down to a depth of  $124\text{ mm}$  (Figure 3.11). This design is optimized to reduce as much as possible the image deformation. In particular, this issue is not caused by the flat external surfaces, but by the inner cylindrical walls. Refractive index matching is the design technique that allows for this minimization.

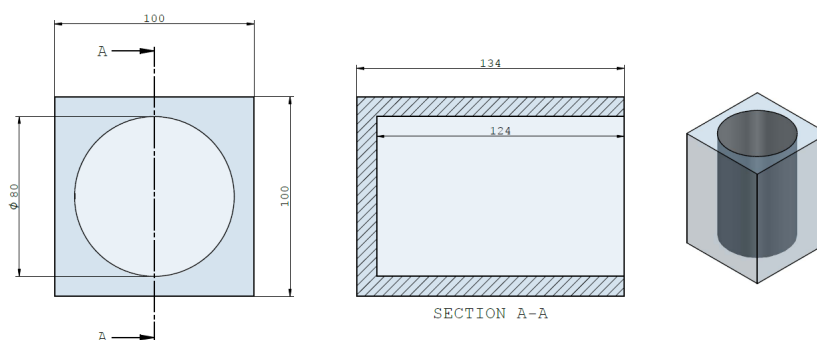


**Figure 3.11:** Technical drawing of the quartz sloshing cells.

### 3.2.11 Cryostat

The cryogenic experiment uses liquid nitrogen with a temperature of 77K at 1 bar of pressure in the sloshing cell. The cryostat is composed by a reservoir filled with LN2 and a sample space, both placed in a vacuum chamber. The reservoir is used to cool down the sample space by means of a heat exchanger in which LN2 flows. The remaining volume of the sample space is filled with gaseous helium to enhance the heat exchange and the temperature uniformity. The cryostat is provided with

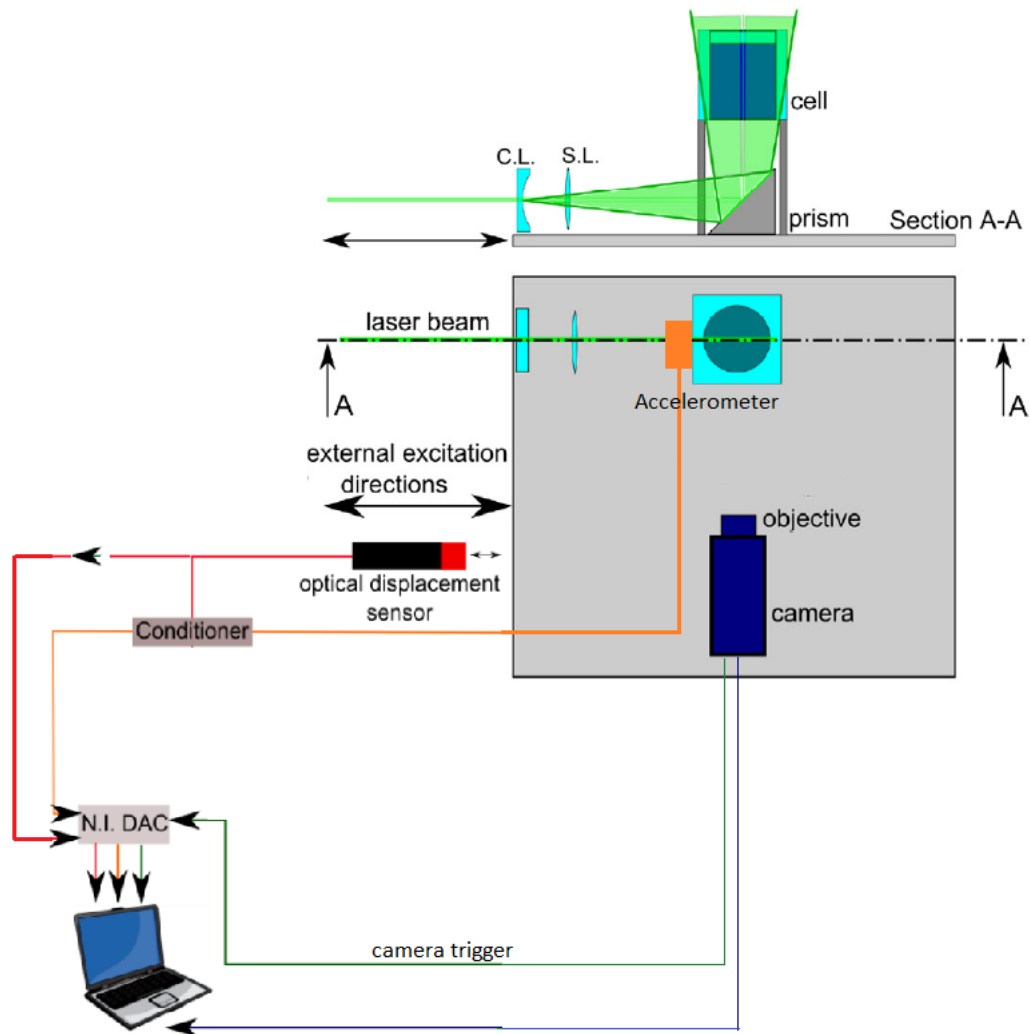


**Figure 3.12:** Scheme of the sloshing isothermal experiment with optical equipment. Modified sketch from ref. [25]

five optical accesses that allow the usage of optical techniques. The cooling of the cryostat and the attainment of a stable temperature in the sample area may require several hours: the system is considered in thermal equilibrium when its temperature variations are below 1K per hour. A sketch of the cryostat as well as a photo representing it mounted on the sloshing table is provided in figures (3.13) and (3.14)

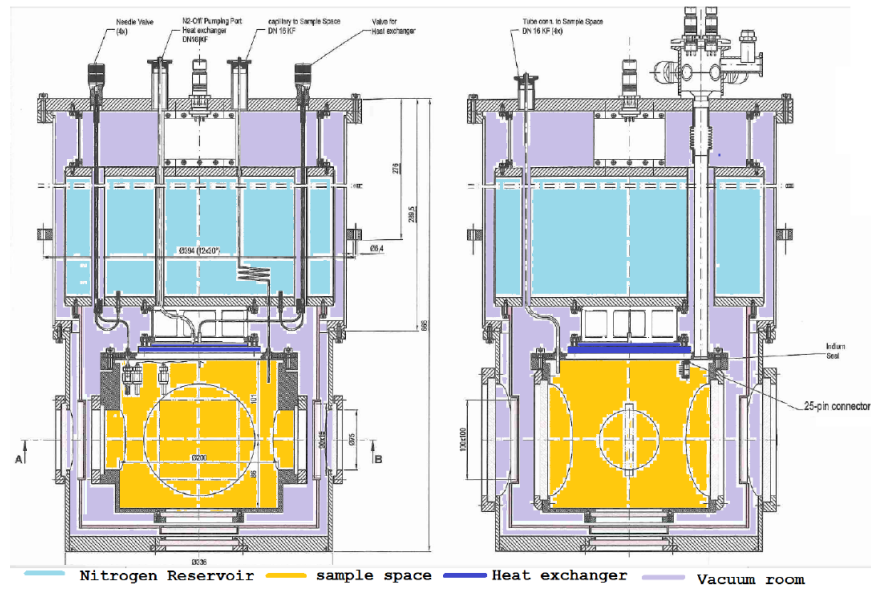


Figure 3.13: Sketch of the cryostat with the main components highlighted

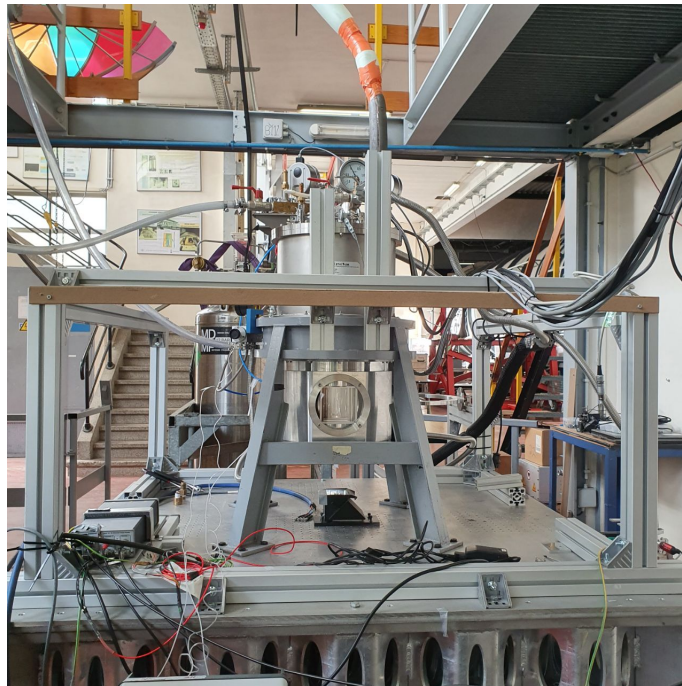


Figure 3.14: Cryostat mounted on the top of the slotted table during the experimental cryogenic campaign

### 3.3 Experimental procedure

Given that with the initial transient recording, several frequencies might be excited at the same time and overlapped to the external excitation frequency; it was decided that the recording of the final damping is more straightforward to be analysed. The steps executed for each measurement are described in the following:

1. the sloshing cell is filled with the liquid up to a height of 60 *mm*. This is accomplished by measuring and marking the desired level and then filling the cell with a syringe. The liquid is seeded with one of the combinations of particles previously illustrated
2. the signal C corresponding to the swirl regime is given as an input from the sloshing table's control system, in order to mix the particles and ensure a homogeneous distribution.
3. start the LabVIEW acquisition, start the Streampix acquisition, start the input signal from the sloshing table's control system and wait long enough to get a recording of the initial transient, then stop the LabVIEW acquisition as well as the Streampix one. The LabVIEW script receives inputs from the accelerometer, the optical displacement sensor and the trigger signal from the camera.
4. once again it is given in input the signal C for mixing reasons
5. in order to record the damping this time, the input signal is triggered, then the LabVIEW acquisition is started (and the Streampix acquisition as well) when the input signal is going to end. The acquisition is stopped when the liquid comes back at rest

These steps were repeated to test each signal (planar and swirl) and two different combinations of particles concerning the non-cryogenic experiment. While, concerning the cryogenic campaign just one combination has been tested. To make sure that it was recorded a fully established damping, it was chosen that starting from a certain number of lines from the *.csv* file as an input of the sloshing table, the recording would start. A similar criteria was followed to record the initial transient.

# Chapter 4

## Data treatment

### 4.1 Image processing

In the planar mode, the acquired images representing HFE7200 and water have a drawback regarding the interface: it is not always clearly visible. For this reason they have been cropped at the tank's edges and below the interface, in order to study the bulk's fluid velocity, as figure (4.1) shows. Then the images have been analyzed through a `Matlab`'s toolbox: PIVlab, a software dedicated to PIV data analysis. Data processing is subdivided in the following steps:

- images import,
- data pre-processing,
- calibration,
- cross-correlation,
- export of speed vectors.

Post-processing involves the drafting of a `Matlab` code that allows to:

- read the speed vectors
- post-process the data (for example obtaining the time course of the velocity fields)

#### **IMAGES IMPORT**

Since the actual damping takes place only when the sloshing table is completely stopped, not all the images were imported in PIVlab. Analysing the LABVIEW's `.lvn` acquisition file it is possible to trace from which image the actual free damping

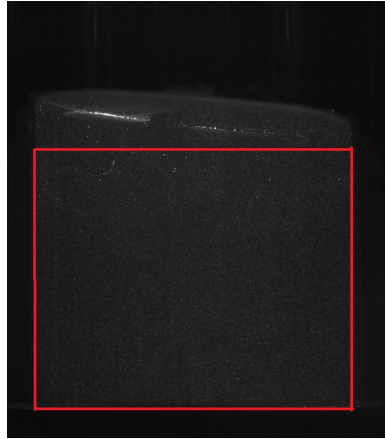


**Figure 4.1:** Cropped image to analyse the planar mode

starts: it is sufficient to find the time instant in which the ODS measures an almost negligible displacement. That time instant multiplied for the camera frame rate gives the number of images that don't have to be imported.

## IMAGES PRE-PROCESSING

A filter that locally enhances images contrast is enabled, it is called CLAHE, that stands for Contrast-Limited Adaptive Histogram Equalization. In this way they are easier to process.

## CALIBRATION

The real dimensions of the cylindrical sloshing cell are the input for calibration. In particular, in both planar and swirl mode images, the only known size is the cylinder diameter  $D = 80 \text{ mm}$ . Moreover  $\Delta t = \frac{1}{f}$  is the time step between images acquired, where  $f$  is the camera frame rate. This allows to obtain the scaling factor

$$Sc = \frac{D}{\#pixel}$$

It is a conversion factor from real dimensions to pixels and vice versa. In the following table are summarized the different calibrations used in the experiments, which vary depending on the frame rate and the number of pixels in the horizontal direction.

| Fluids  | Regime | $f$ [Hz] | $Sc$ [mm/px] |
|---------|--------|----------|--------------|
| HFE7200 | Planar | 100      | 0.0381       |
| Water   | Planar | 75       | 0.0539       |
| HFE7200 | Swirl  | 75       | 0.0268       |

Table 4.1: Calibrations

## CROSS-CORRELATION SETTINGS

The Fast Fourier transform is a practical way to perform the cross-correlation. The latter consists in dividing the image in different areas and to correlate them to the next ones in time. This operation can be of two kinds:

1. *single pass*, there is a unique size of the areas,
2. *multi pass*, areas' size is progressively reduced.

A rule of thumb to choose the areas' optimal size is that inside each area a sufficient number of particles have to be present (at least 8-10 for planar PIV)

## 4.2 Post-processing

Once PIVlab has analyzed all the frames, they can be exported in a `.mat` file and manipulated through a `Matlab` script. In the workspace several variables are loaded, however four of them are interesting for the damping analysis:

1.  $u_{original}$  it is a cell that contains the temporal evolution of the  $u$  component in the entire field of motion,
2.  $v_{original}$  it is a cell that contains the temporal evolution of the  $v$  component in the entire field of motion,
3.  $x$ ,
4.  $y$ .

PIVlab exports variables as cells, but working with double type data is more convenient. The physical dimensions of the domain are obtained by exporting  $x$  and  $y$ .

## 4.3 Logarithmic decrement method

Manipulating the variables from the `.mat` file obtained by means of PIV it is possible to extract some useful information regarding the fluid velocity field. First

of all, it is possible to reconstruct the time history of each velocity component. The two following snapshots are presented as an example: Since the final goal is to

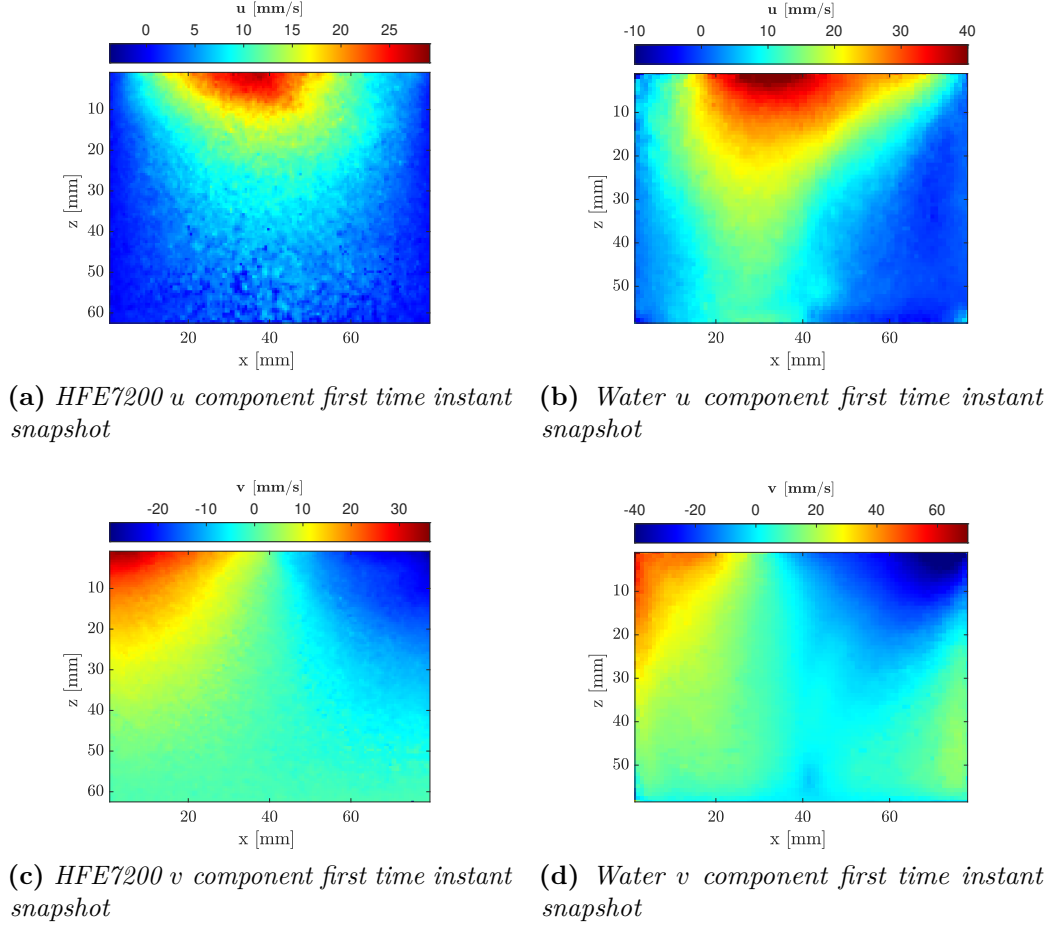


**Figure 4.2:** Snapshots of the first time instants of  $u$  and  $v$  component in the planar mode

obtain the first damping ratio, in the following is presented one possible procedure, called logarithmic decrement method:

1. first, a point of the fluid domain has to be selected, located at particular coordinates in terms of  $(x, z)$ . The selection of the point follows some criteria. Concerning the  $z$  component the point must be as much as possible near the interface to catch the strongest value of damping. Concerning the  $x$  coordinate, it is a compromise among the following considerations:

- the  $u$  component reaches its maximum value towards the tank's centre

- the  $v$  component reaches its maximum value towards the tank's edges
- the maximum value of the damping should be captured towards the tank's edges, however viscosity effects could affect its estimation
- in the planar mode there is a node at the tank's centre (zero-velocity point)

For instance, in figure (4.3) is showed a point located at  $x = R/4$  from the left edge.

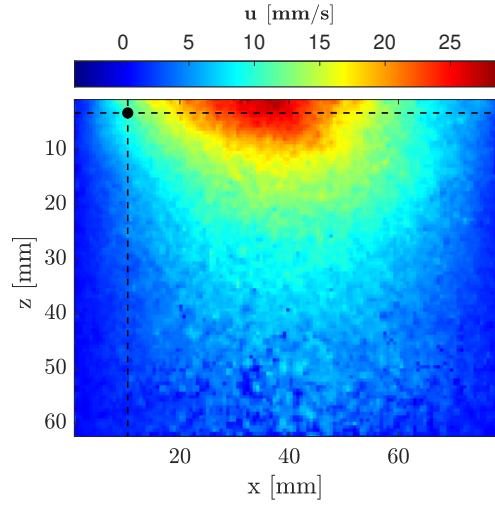


**Figure 4.3:** Selection of the point located at  $x = R/4$

2. it is extracted the temporal evolution of the selected point in terms of  $u$  and  $v$  component. A more precise estimation of the damping ratio can be obtained extracting the peaks from the velocity magnitude rather than from the singular components  $|\vec{V}| = \sqrt{u^2 + v^2}$ . Even though the signal has an oscillatory behavior, the amplitude's peaks decay in time, indicating the presence of damping (4.4)
3. selecting the positive peaks of the signal, they form a straight line when it is calculated the logarithm of the ratio  $|\vec{V}_{peak}|/|\vec{V}_{max,peak}|$  and when they are plotted as a function of time divided by the period of the external excitation ( $T = 1/f_{ext}$ ) as figure (4.5) shows. At this point, the damping ratio is the slope of the linear fitting interpolating the experimental points. In particular:
  - $|\vec{V}_{peak}|$  is the positive peak of the velocity magnitude signal for each time instant
  - $|\vec{V}_{max,peak}|$  is the maximum value among all the positive peaks

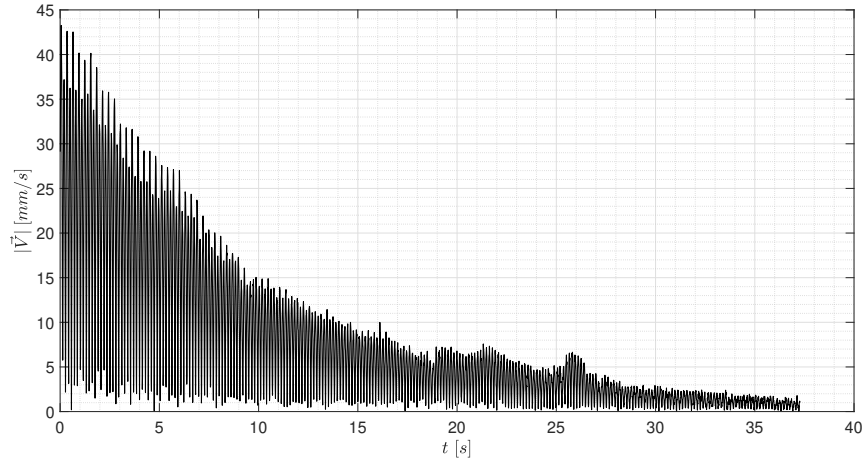


**Figure 4.4:** Temporal evolution of the velocity magnitude at the point located at  $x = R/4$ . HFE7200 planar mode test 1

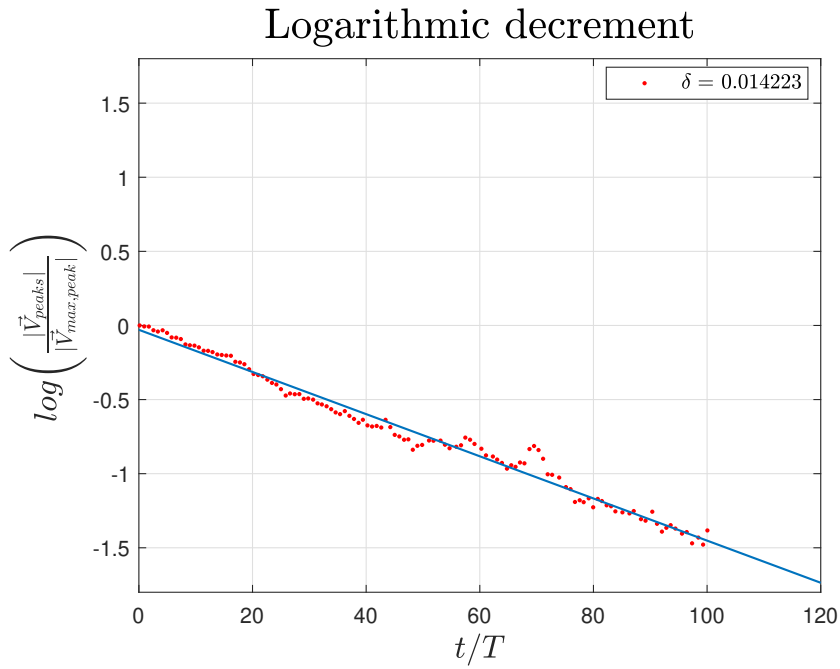


**Figure 4.5:** Damping ratio calculated at point located at  $x = R/4$ . HFE7200 planar mode test 1

4. finally, to get a more complete view, the calculation made for the single point can be extended to the entire bulk. This leads to the determination of the

three different damping maps, depending on which velocity component is selected ( $u, v, |\vec{V}|$ ).

## 4.4 Data driven decomposition methods

In fluid dynamics context is essential the detection of coherent structures, particularly when the study of a complex flow is approached. There are some coherent features called modes, they can be detected according to their energy contribution. In the overall view, a data-driven decomposition method collects data from important flow configurations and classifies them into representative structures, rather than considering every single detail in a flow and analyzing equations of motion in isolation. Two main data-driven decomposition methods can be identified:

- POD, that stands for Proper Orthogonal Decomposition, it is an energy-based decomposition, that can be defined as a matrix factorization. POD is one of the first data-driven modal decompositions in fluids. It can reduce matrices' rank using a SVD (Singular Value Decomposition). POD provides the modes with the highest amplitude (in this sense it is aimed at energy maximization), the convergence of the approximation is assured increasing the number of modes. POD's main advantage is its huge applicability to data coming from both simulations and experiments. It guarantees the identification of the most energetic modes, although their individual interpretation might be challenging. It might occur that different phenomena characterized by widely spaced frequencies, have very similar energy content. In such cases, an energy-based formulation cannot distinguish the various contributions, which according to POD share the same structures [26]. The POD's temporal structures  $\psi_{\mathcal{P}_r}$  must be eigenvectors of the temporal correlation matrix  $\mathbf{K}[k, n] = \langle \vec{\mathbf{u}}(\mathbf{x}_i, t_k), \vec{\mathbf{u}}(\mathbf{x}_i, t_n) \rangle_S$ , with  $\langle \bullet \rangle_S$  the expectation operator in the space domain. Hence:

$$\mathbf{K}\psi_{\mathcal{P}_r}(t_k) = \lambda_r\psi_{\mathcal{P}_r}(t_k) \quad \forall r \in [1, R] \rightarrow \mathbf{K} = \sum_{r=1}^R \lambda_r\psi_{\mathcal{P}_r}(t_k)\psi_{\mathcal{P}_r}^T(t_k) \quad (4.1)$$

The correlation matrix is symmetric and positive definite. The specific choice of the temporal structures makes the associated spatial structures orthonormal, that is why POD is defined as 'proper orthogonal'

If  $n_t$  is the number of time instants and  $n_s$  is the number of spatial points, one might decide whether to work with the diagonalization of  $\mathbf{K}$  or  $\mathbf{C}$  (the spatial correlation matrix) depending on whether  $n_t \ll n_s$  or  $n_s \ll n_t$ , and

compute by correlation the other structures ( $\phi_k$  through equation (??) or  $\psi_{\mathcal{P}_r}$  through equation (??))

$$\mathbf{D} = \mathbf{\Phi}_{\mathcal{P}} \mathbf{\Sigma}_{\mathcal{P}} \mathbf{\Psi}_{\mathcal{P}} \quad (4.2)$$

for datasets equally spaced in time and space, equation (4.2) represents a singular value decomposition of  $\mathbf{D}$

- DMD, that stands for Dynamic Mode Decomposition, it is a frequency-based decomposition. Frequency based methods, unlike energy-based ones, assign to each mode a single frequency deduced by data. Since each frequency is considered complex, this method implies an exponential decay or growth in time. DMD can be thought as a combination of POD with Fast Fourier transforms in time in order to minimize potential windowing effects (consisting in the presence of the spectral noise at the boundaries of the spectrum plot). If  $\mathbf{D}_1 \in \mathbb{R}^{2n_x n_y \times n_t - 1}$  and  $\mathbf{D}_2 \in \mathbb{R}^{2n_x n_y \times n_t - 1}$  are two portions of the snapshot matrix  $\mathbf{D} \in \mathbb{R}^{2n_x n_y \times n_t}$  shifted in time, and if the dynamic system under exam is linear, then they are related through a propagator matrix  $\mathbf{P}$  according to the following relation  $\mathbf{D}_2 = \mathbf{P} \mathbf{D}_1$ . The eigenvalues of the propagator matrix influence the evolution of the system and its eigenvectors are the DMD modes. The previous equation can be solved in a "old-fashioned" way, meaning that computing  $\mathbf{P}$  leads to a classical least square problem and implies the use of the pseudo-inverse of  $\mathbf{D}_1$ . However, the eigendecomposition of  $\mathbf{P}$  can be computationally demanding for most of the real fluid dynamical applications. Thus, the solution is to apply the eigendecomposition on a reduced POD system that relies on a reduced POD basis ( $\tilde{\mathbf{\Phi}}_{\mathcal{P}} \in \mathbb{R}^{n_r \times n_r}$  where  $n_r$  is the number of selected modes). The reduced system becomes:

$$\mathbf{D}_2 \approx \mathbf{P} \mathbf{D}_1 \longrightarrow \underbrace{\tilde{\mathbf{\Phi}}_{\mathcal{P}}^T \mathbf{D}_2}_{\mathbf{V}_2} \approx \underbrace{\tilde{\mathbf{\Phi}}_{\mathcal{P}}^T \mathbf{P} \tilde{\mathbf{\Phi}}_{\mathcal{P}}}_{\mathbf{S}} \underbrace{\tilde{\mathbf{\Phi}}_{\mathcal{P}}^T \mathbf{D}_1}_{\mathbf{V}_1} \longrightarrow \tilde{\mathbf{V}}_2 \approx \tilde{\mathbf{S}} \tilde{\mathbf{V}}_1 \quad (4.3)$$

Here the reduced propagator is thus  $\tilde{\mathbf{S}}$

$$\tilde{\mathbf{S}} = \tilde{\mathbf{\Phi}}_{\mathcal{P}}^T \mathbf{P} \tilde{\mathbf{\Phi}}_{\mathcal{P}} = \tilde{\mathbf{\Phi}}_{\mathcal{P}}^T \mathbf{D}_2 \tilde{\mathbf{\Psi}}_{\mathcal{P}} \tilde{\mathbf{\Sigma}}_{\mathcal{P}}^{-1} \quad (4.4)$$

The eigenvalue decomposition of this propagator  $\tilde{\mathbf{S}} = \mathbf{Q} \mathbf{\Lambda} \mathbf{Q}^{-1}$  controls the evolution of the reduced system. The advantages of this method are its simplicity in the execution and the small number of hypothesis adopted on the system under exam. The computational cost of the algorithm is a singular value decomposition (SVD) of the snapshot matrix constructed from the data.

There is another decomposition method called Discrete Fourier Transform (DFT) which was not used to the post-processed data set. The main difference with

the previous techniques is that each mode is associated to a frequency that is forced to be a multiple of the fundamental tone  $f_0 = 1/T$  where  $T = n_t \Delta t$  is the observation time. Both decomposition methods were applied to the captured snapshots, however, the DMD results showed a poor ability to reconstruct the fluid velocity field even with a fairly large number of modes (about 500). DMD failure could be in the approximation that the system to solve is considered linear, probably in damping application, this is a too strong hypothesis. Instead, as mentioned before, the advantage of POD is that it always converges; as a result, modal analysis was performed using the POD approach.

POD has been applied to the full dataset of the fluid velocity field of both HFE and water. If  $\mathbf{D}_u \in \mathbb{R}^{n_x n_y \times n_t}$  is the matrix reshaped such that each column contains the  $u$  component velocity field at a specific time instant, and  $\mathbf{D}_v \in \mathbb{R}^{n_x n_y \times n_t}$  is the same concerning the  $v$  component. Then the matrix  $\mathbf{D} \in \mathbb{R}^{2n_x n_y \times n_t}$  is built such that it assembles  $\mathbf{D}_u$  and  $\mathbf{D}_v$ . Where the subscripts refer to :

- $n_x$  number of pixels along the x-direction,
- $n_y$  number of pixels along the y-direction,
- $n_t$  number of time instants that corresponds to the number of snapshots acquired.

POD has been applied using the `MODULO` package implemented in `Python` [27]. In input matrix  $\mathbf{D}$  is required as well as  $n_r$ , that is the number of modes selected for the POD analysis. In this case the first 500 modes were selected. The outputs are:

- $\Phi_{\mathcal{P}} \in \mathbb{R}^{2n_x n_y \times n_r}$  the spatial structures,
- $\Psi_{\mathcal{P}} \in \mathbb{R}^{n_t \times n_r}$  the temporal structures,
- $\Sigma_{\mathcal{P}} \in \mathbb{R}^{n_r \times n_r}$  a diagonal matrix containing the amplitude of the modes.

Once the results are obtained, a lot of interesting information can be collected regarding modes' features and their influence on damping. The results discussion is developed in chapter 5.

# Chapter 5

## Results

### 5.1 Test matrix

As mentioned before, some points in Miles' phase diagram pertaining to different sloshing regimes were selected. Of particular interest are the planar and the swirling mode because this project focuses on linear and non-linear sloshing. The non-cryogenic tests were conducted using two liquids: water and HFE7200, whereas the cryogenic tests were carried out only with liquid nitrogen. The tested points are displayed in figure (5.1) and they are specified in table (5.1) in terms of dimensionless external amplitude and frequency.

| Fluids  | Regime | $X_0/R$ | $\Omega/\omega$ | $X_0$ [mm] | $f_{ext}$ [Hz] |
|---------|--------|---------|-----------------|------------|----------------|
| HFE7200 | Planar | 0.03    | 0.8             | 1.2        | 2.7            |
|         | Swirl  | 0.03    | 1.01            | 1.2        | 3.4            |
| Water   | Planar | 0.025   | 0.89            | 1          | 3              |
| $LN_2$  | Planar | 0.03    | 0.8             | 1.2        | 2.7            |
|         | Swirl  | 0.03    | 1.01            | 1.2        | 3.4            |

**Table 5.1:** Tested fluids

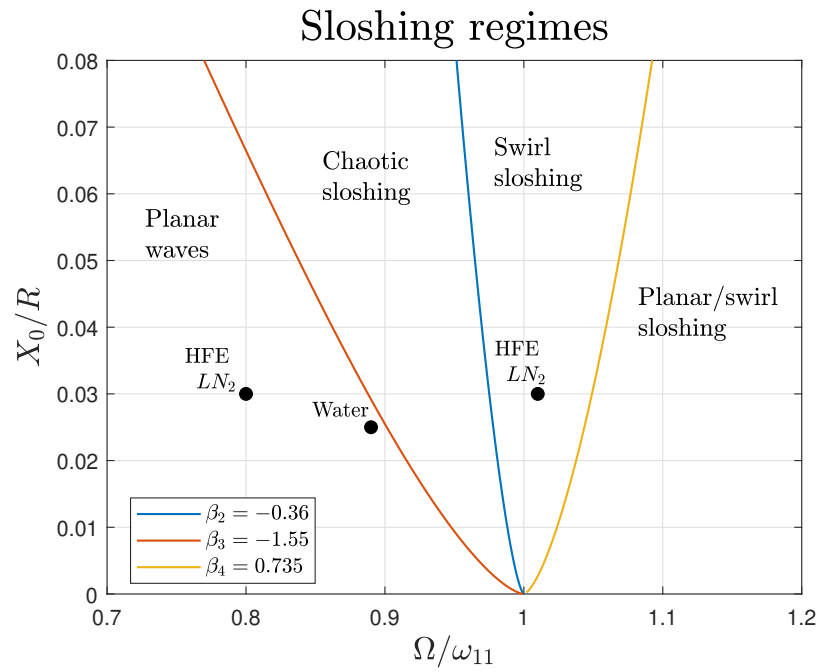


**Figure 5.1:** Tested points. The HFE points implicitly indicate the tests performed with LN2

## 5.2 Planar mode

### 5.2.1 Damping maps

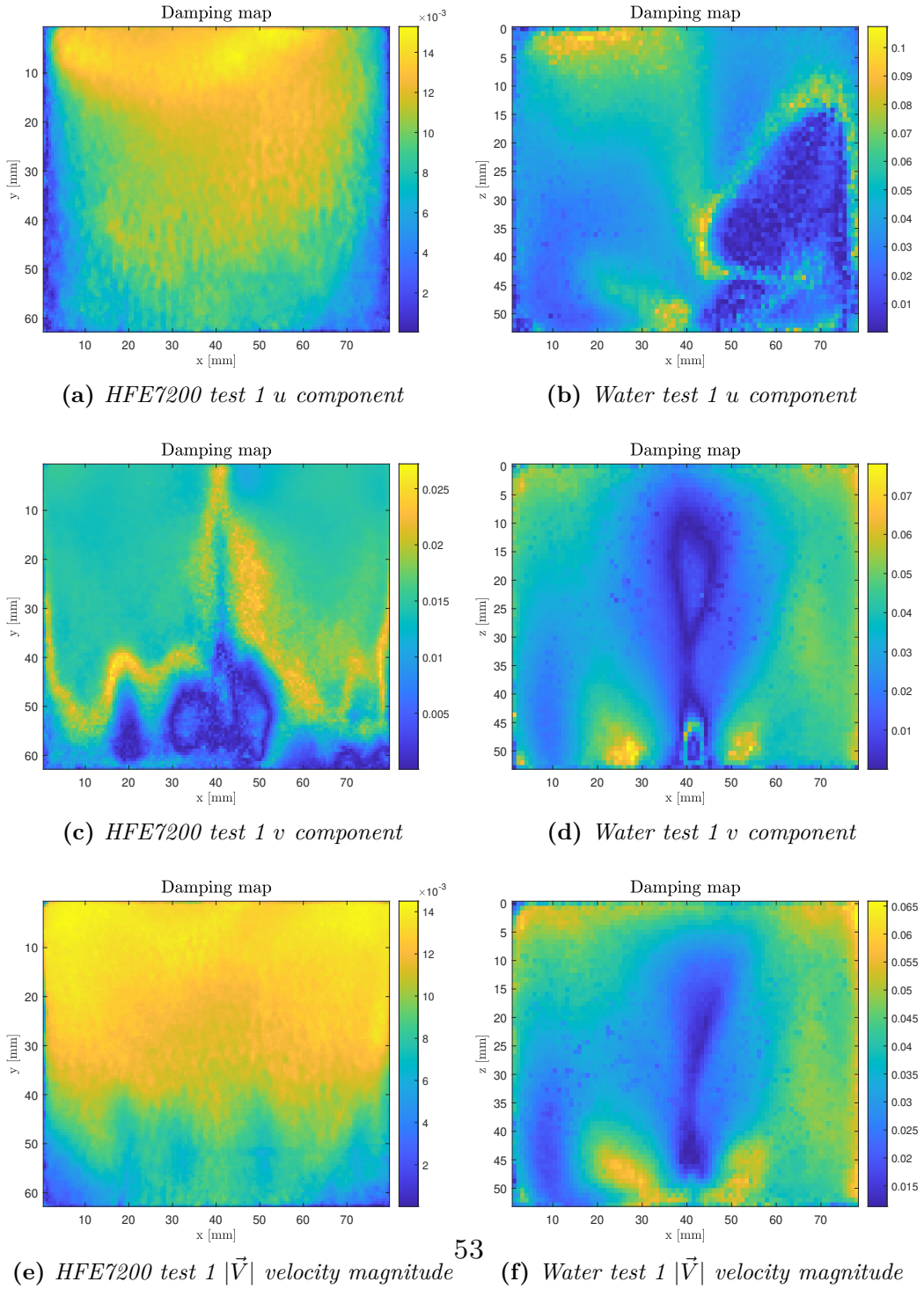
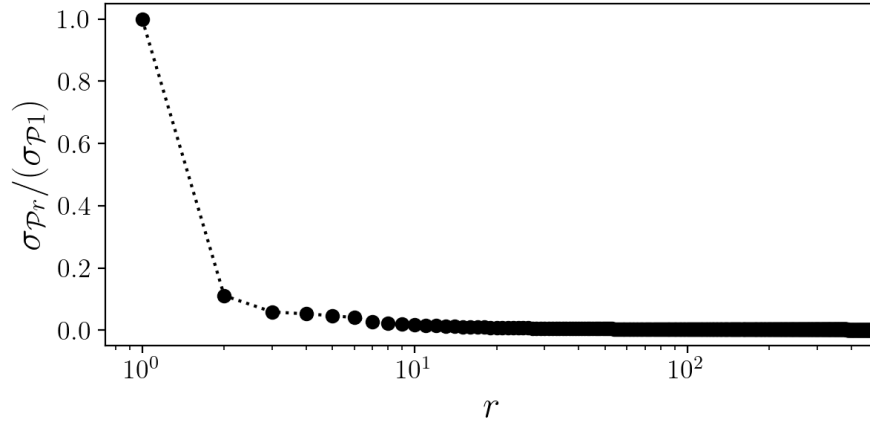


**Figure 5.2:** Damping maps. On the left, HFE7200 test 1. On the right, water test 1

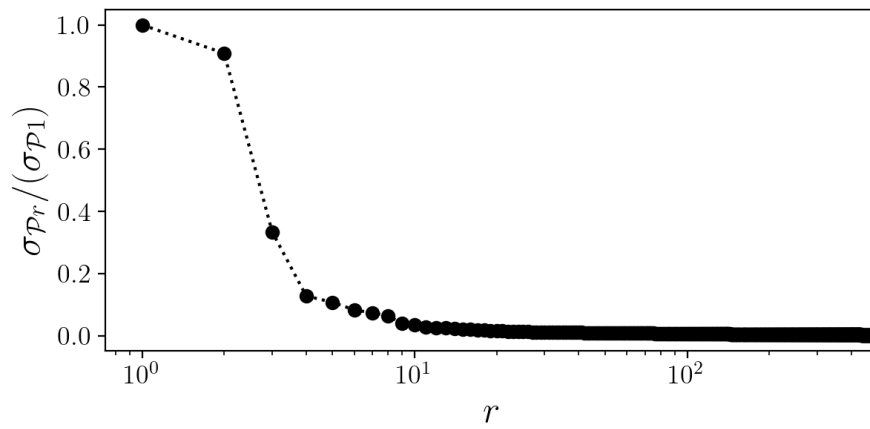
Figure (5.2) shows the damping maps obtained applying the logarithmic decrement method illustrated in chapter 4. First of all, while looking at the damping map for the  $u$  component of the HFE7200, it is clear that damping is stronger in the upper part of the container, which is the closest to the interface. While, proceeding towards the bulk, the fluid is almost at rest, consequently the damping ratio is very close to zero. The presence of a nodal diameter perpendicular to the plane of oscillation is a key property of the planar mode, as evidenced by the damping map for the  $v$  component, which shows "a line" along which the damping ratio approaches zero. Finally, considering the velocity magnitude ( $|\vec{V}| = \sqrt{u^2 + v^2}$ ), the damping map becomes almost homogeneous, with the highest damping occurring near the interface, since the latter is the portion of fluid that experiences a wider motion (except for the interface). Proceeding towards the bottom the trend is quite similar to the damping map related to the  $u$  component, where the damping ratio is extremely close to zero since the bulk can be considered almost at rest. Analogous remarks can be provided regarding the water damping maps while looking at figure (5.2). One slightly difference can be pointed out: the colorbar displays a much more variable damping ratio (it changes of one order of magnitude along the  $z$ -direction, whereas for HFE7200 the order of magnitude is constant, around  $10^{-3}$ ). The damping ratio can be considered as a measure of the fluid capability to counteract the motion externally imposed. Since water's damping ratio is greater than HFE7200's one, this means that water can damp the imposed motion in less time, compared to HFE7200. The damping ratio value is strongly related to the fluid's viscosity: the higher is the viscosity, the higher damping ratio will be measured. In reference to table (3.3) water has a higher viscosity than HFE7200, which validates the obtained damping ratio values and physically implies that water has a stronger resistance to external excitations.

### 5.2.2 POD

In this section the results obtained applying the Proper Orthogonal Decomposition (POD), explained in section 4, are shown. First of all, the POD analysis has been restricted to the first  $r = 500$  modes for both liquids. The plots showing their normalized amplitudes  $\sigma_{P_r}/\sigma_{P_1}$  point out which are the prevalent modes in the sloshing motion. Figure (5.3) shows a comparison between the modes of HFE7200 and water related to the planar mode.



(a) HFE7200 test 1

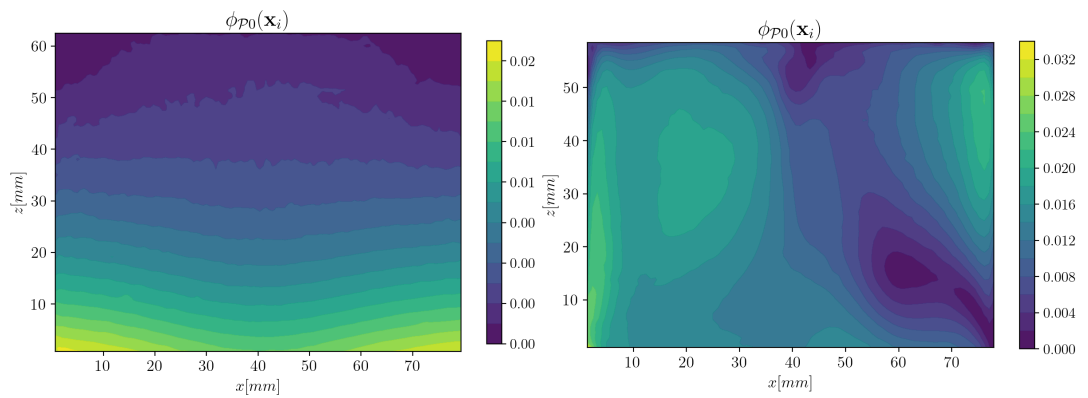


(b) Water test 1

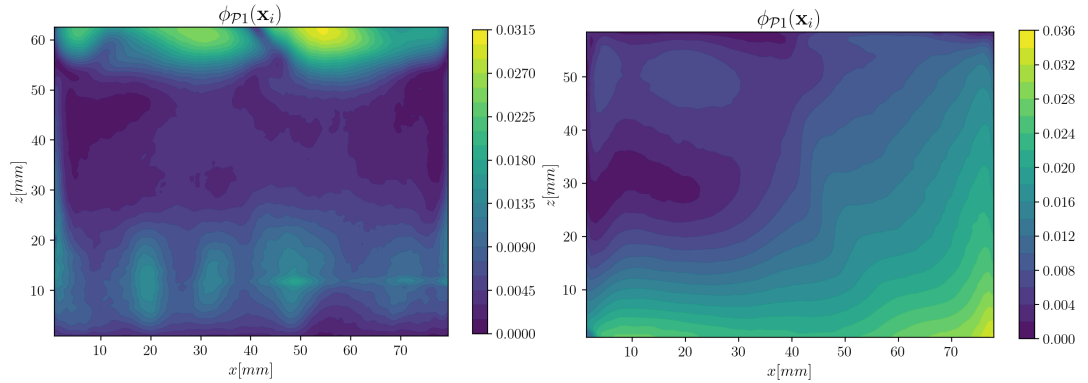
**Figure 5.3:** Modes' amplitude

Comparing the modes energy, in both cases the majority of the normalized modes' amplitudes decays to zero. For this reason only the first four modes are considered relevant in the following analysis. The main difference between the two liquids is that for HFE7200 the first mode is the most energetic one (it contains almost the 90% of the total energy), while the others are comparable. Concerning water, most of the energy is contained in the first two modes. From the selected modes some important information can be retrieved:

1. each spatial structure gives an idea on the spatial distribution of the mode's vibrations



(a) HFE7200 test 1 spatial structure mode 0 (b) Water test 1 spatial structure mode 0



(c) HFE7200 test 1 spatial structure mode 1 (d) Water test 1 spatial structure mode 1

**Figure 5.4:** Spatial structures planar mode. On the left HFE7200 test 1, on the right water test 1

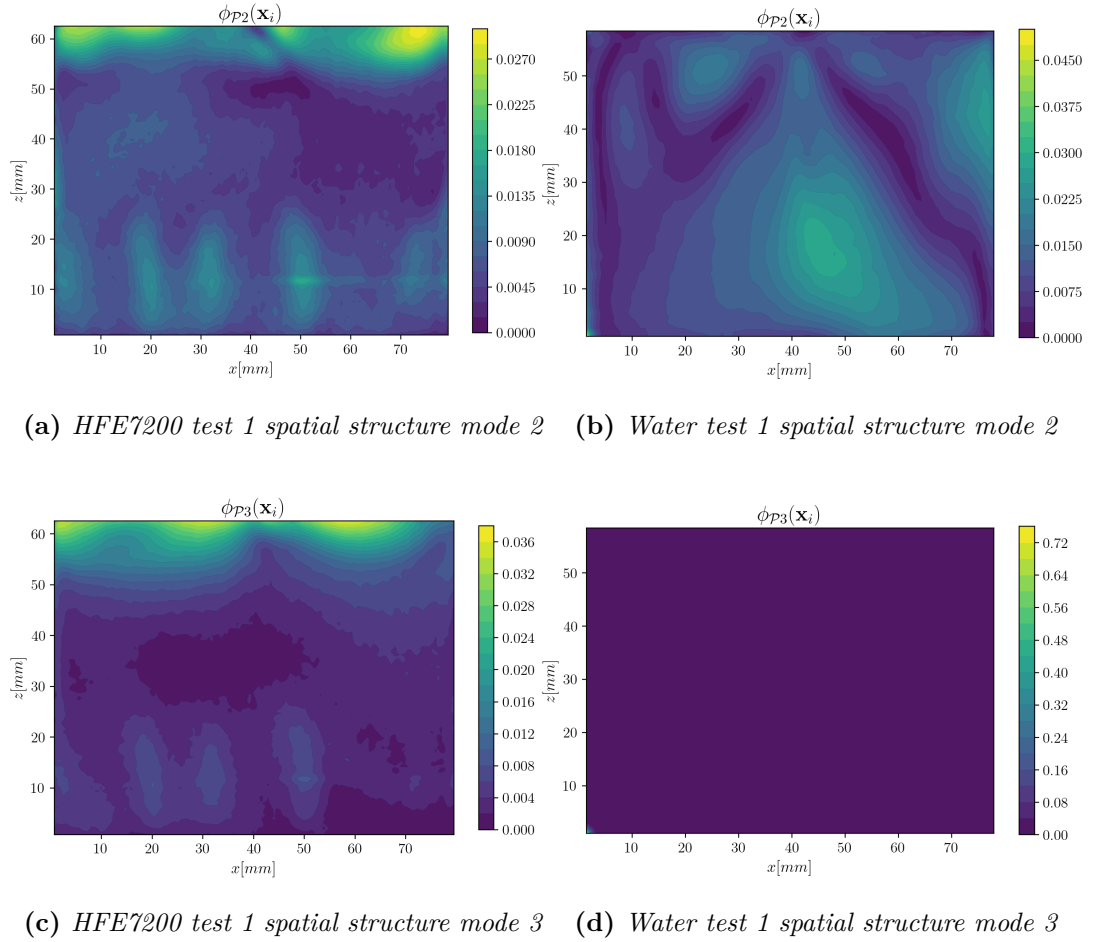
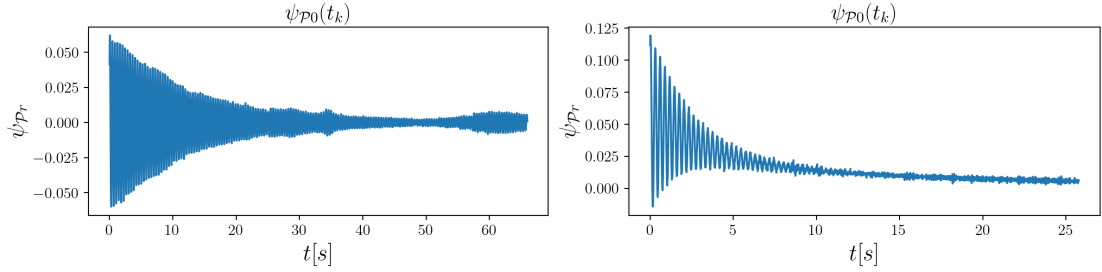


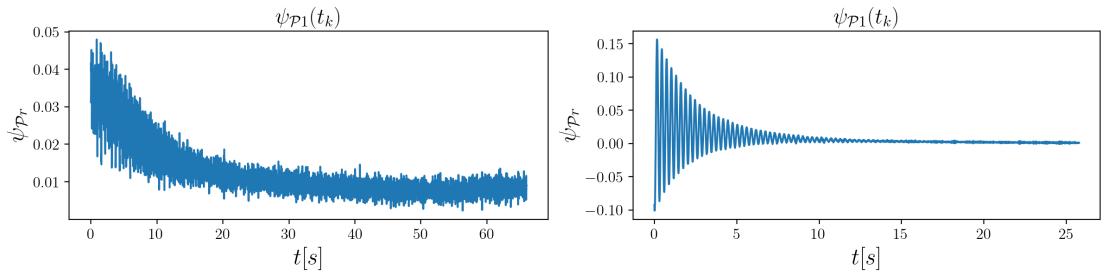
**Figure 5.5:** Spatial structures planar mode. On the left HFE7200 test 1, on the right water test 1

Looking at the modes, and looking at the repeatability tests it is evident that the experiments in water are less repeatable. It appears that the velocity fields with the water test cases are ‘more complex’ than the ones in HFE. The planar mode is supposed to have a structure whose isolines are almost horizontal. This is seen in mode 0 for HFE7200 and in mode 1 for water. Mode 3 in the water case is the less relevant concerning the energy content.

2. temporal structures indicate how much energy is dissipated in time for each spatial structure, meaning for each mode identified by the POD



(a) *HFE7200 test 1 temporal structure mode 0* (b) *Water test 1 temporal structure mode 0*



(c) *HFE7200 test 1 temporal structure mode 1* (d) *Water test 1 temporal structure mode 1*

**Figure 5.6:** Temporal structures planar mode. On the left HFE7200 test 1, on the right water test 1

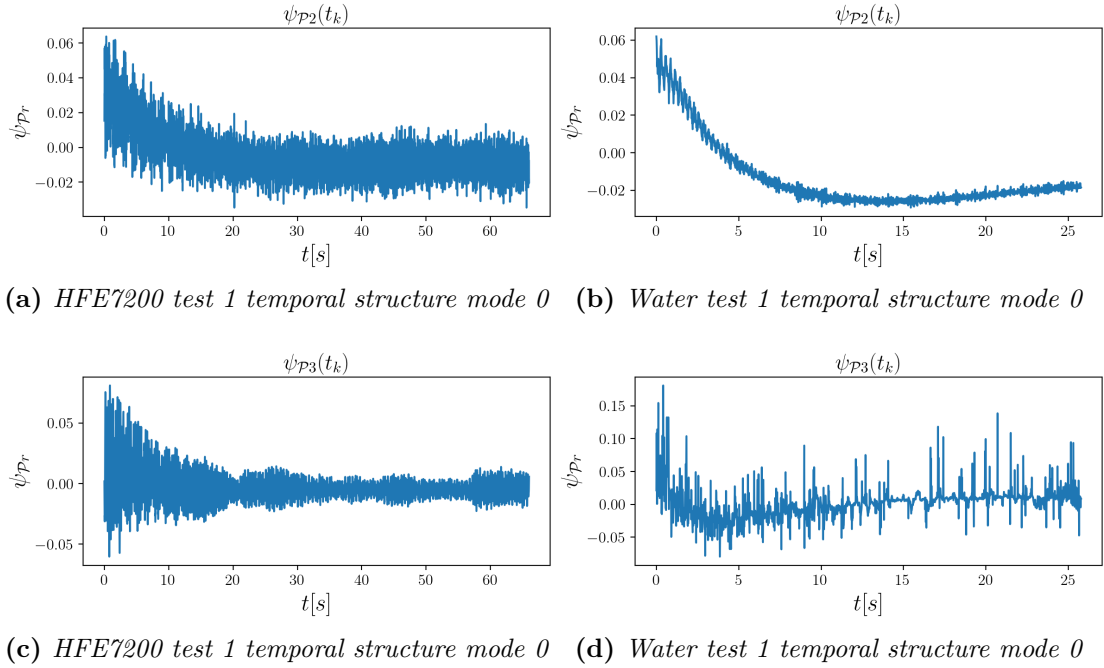


**Figure 5.7:** Temporal structures planar mode. On the left HFE7200 test 1, on the right water test 1

Analysing the temporal structures, it can be noticed that mode 0 for HFE7200 and mode 1 for water follow an exponential trend which is typical of the linear decay behavior of the planar sloshing mode. The leading spatial structures of the modes are not symmetric and that their temporal evolution (see Fig 5.6 (b)) has an extra transient in the first 4-5 seconds. It is as if the flow takes much more time to ‘forget’ about the previous sloshing phase and start the damping phase. This is also evident in the spectra, as you see a leading frequency at about 0 Hz. That’s the transient talking to you!

- the frequency spectrum, obtained applying the Fast Fourier Transform to the temporal structures. By evaluating the peaks of the FFT, the frequency domain may be used to immediately determine which frequencies are the most relevant for the mode under consideration

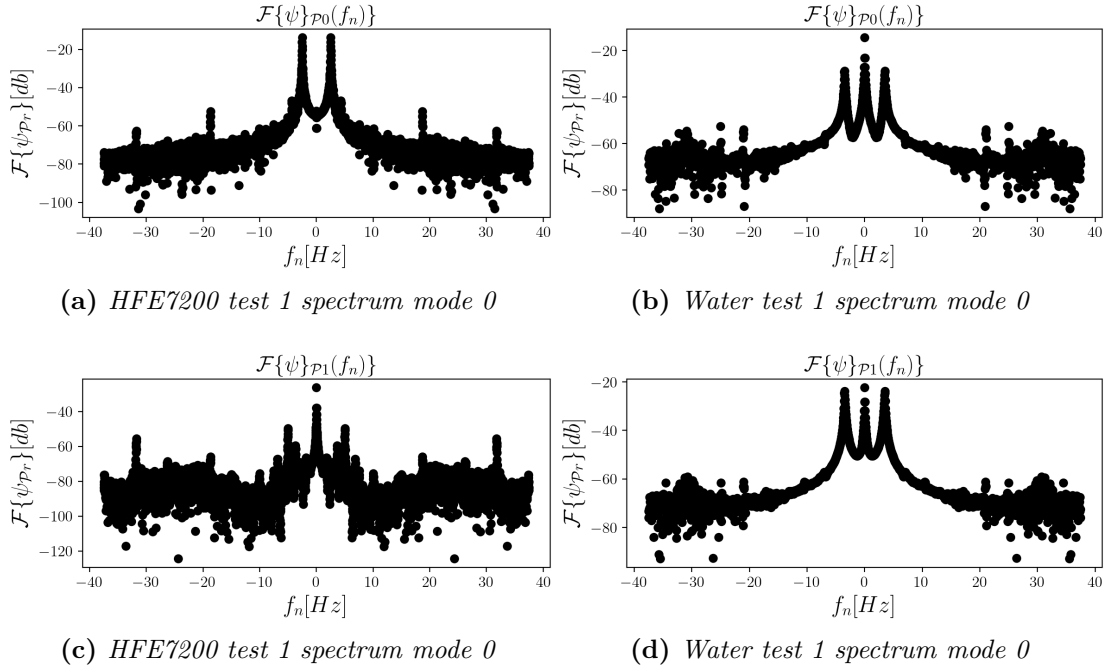


**Figure 5.8:** Temporal structures' Fast Fourier Transform planar mode. On the left HFE7200 test 1, on the right water test 1

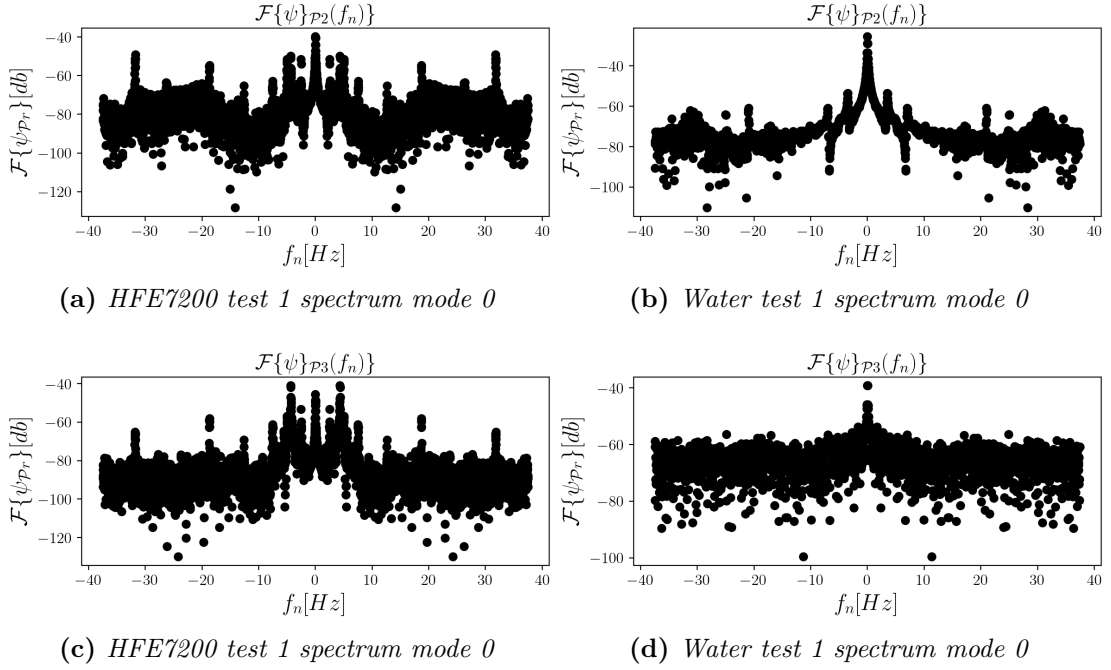


**Figure 5.9:** Temporal structures' Fast Fourier Transform planar mode. On the left HFE7200 test 1, on the right water test 1

In the frequencies analysis, two frequencies have to be kept in mind: the frequency of the external excitation and the first natural frequency pertaining to the cylindrical reservoir. The latter can be calculated through equation (2.10). Table (5.2) specifies the peaks observed in the planar mode spectra for both liquids, represented in figures (5.8) and (5.9).

| HFE7200 |                        |                       |                       | Water |                        |                       |                       |
|---------|------------------------|-----------------------|-----------------------|-------|------------------------|-----------------------|-----------------------|
| Mode    | $f_{\text{peak}}$ [Hz] | $f_{\text{ext}}$ [Hz] | $f_{\text{nat}}$ [Hz] | Mode  | $f_{\text{peak}}$ [Hz] | $f_{\text{ext}}$ [Hz] | $f_{\text{nat}}$ [Hz] |
| 0       | 2.51                   | 2.7                   | 3.37                  | 0     | 3.49                   | 3                     | 3.37                  |
| 1       | 3.49                   |                       |                       | 1     | 3.49                   |                       |                       |
| 2       | 3.49                   |                       |                       | 2     | 3.49                   |                       |                       |
| 3       | 3.49                   |                       |                       | 3     | 0                      |                       |                       |

**Table 5.2:** Peaks in the frequency spectrum for both liquids

Concerning HFE7200 the excitation frequency is lower than the first natural one; each mode has a peak at a frequency greater than  $f_{\text{nat}}$ , except for mode 0. While considering water each peak is very close to the first natural frequency; also in this case the excitation frequency is lower than the first natural one. This means

that once the external excitation is stopped, the system tends to vibrate around the first natural frequency. This is true for every mode, except for mode 3, which is the less energetic one, as previously highlighted.

The logarithmic decrement method has been applied to the temporal structures presented in figures (5.6)a and (5.6)d because they are the only structures that have a linear oscillatory behaviour around zero. The results are documented in table (5.3) and figure (5.10). The  $\delta$  values reported in table (5.3) are the slopes of the linear fittings (5.10)c and (5.10)d. In particular, figure (5.10) shows only the first test executed on both liquids. While table (5.3) compares the damping ratios arising from several tests.

| Test | HFE7200    | Water      | Method |
|------|------------|------------|--------|
|      | $\delta_0$ | $\delta_1$ |        |
| 1st  | 0.010      | 0.043      | POD    |
| 2nd  | 0.011      | 0.064      |        |
| 3rd  | -          | 0.070      |        |

**Table 5.3:** Damping ratios obtained applying POD to a single mode

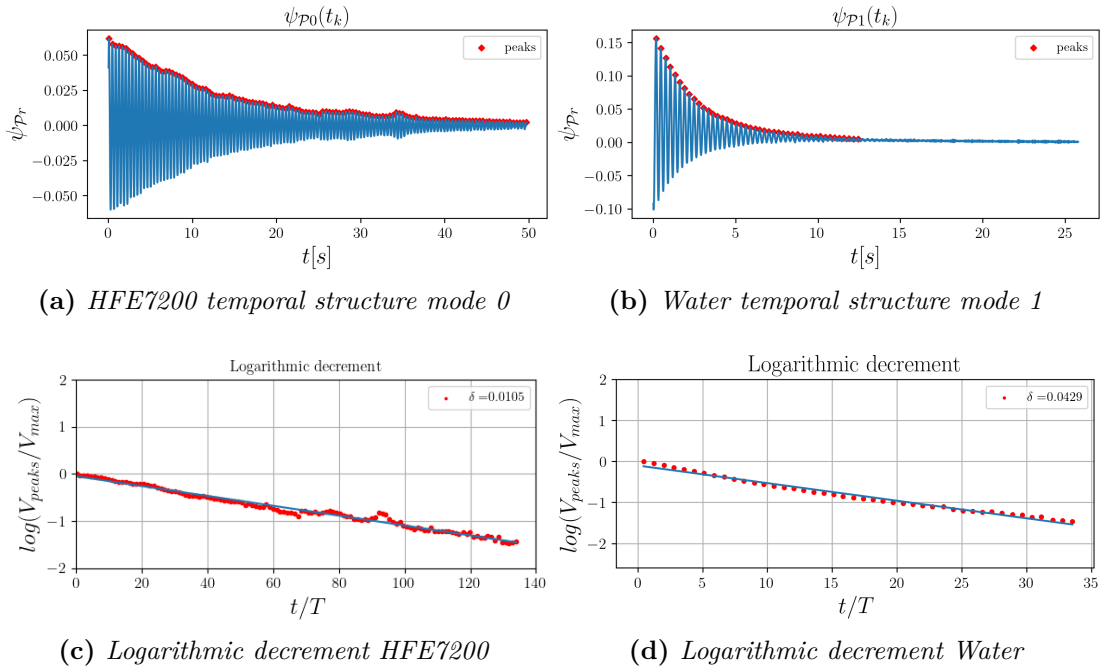


**Figure 5.10:** Logarithmic decrement method. On the left HFE7200 test 1, on the right water test 1

From the POD analysis matrix  $D$  has been reconstructed starting from only the modes that are considered relevant (the first four in both cases). In particular, the reconstruction is obtained through the matrix product among the spatial structures, the modes amplitudes and the temporal structures but only related to the first four modes.

$$D = \Phi_{\mathcal{P}} \Sigma_{\mathcal{P}} \Psi_{\mathcal{P}} \quad (5.1)$$

Since matrix  $D$  contains the reconstructed fluid velocity field, a mean value of the damping ratio can be computed in the first 30 *mm* of the reservoir below the interface, applying the logarithmic decrement method. The same mean value can be extracted from the damping maps previously computed. The results have been compared with the theoretical model presented in chapter 2 as well as the other tests to ensure that the signal was repeatable. Table (5.4) summarizes all of them. The theoretical model and the empirical formula are able to make pretty accurate predictions about the HFE7200's damping ratio, instead, the POD reconstruction tends to underestimate it. Overall it can be concluded that there is good agreement among the different estimates. Concerning water, the predictions are not so accurate both from the theoretical model and the empirical formula, the reason could be that water has a higher viscosity compared to HFE7200, this implies that it takes less time to damp (10s for water and 50s for HFE7200). Probably a shorter damping time affects the results badly. In addition, POD reconstruction provides results in good agreement with the theoretical and the empirical formula. It is not surprising that the results related to POD applied to a single mode and the POD reconstruction of HFE7200 are similar because most of the energy is contained in the first mode. Conversely, in the water case, the inclusion of the other modes besides the first, leads to different results. A probable explanation is that, in reference to figure (5.3), also the second mode contains an energetic contribution not negligible.

Another possible reason why there is lack of consistency among the results predicted by the theoretical model, POD and the experimental ones is that the damping ratio has three different definitions according to which point of view is adopted. From the theoretical/empirical point of view the eigenfrequencies and eigenmodes can be computed only in a linear case, meaning that the theoretical formula is valid only for small amplitudes and when the motion is planar. However, experimentally, depending on the regime tested, both the linear and non-linear conditions can be encountered. Finally, the data-driven decompositions define the decaying differently: concerning the POD, the most energetic modes are found, within them, some modes decay linearly while others have proper non-linear behaviour. Instead, according to DMD, each mode decays/grows exponentially depending if the related frequency is higher/lower than the unit.

| Test            | HFE7200  |          | Water    |          | Method                |
|-----------------|----------|----------|----------|----------|-----------------------|
|                 | $\delta$ | $\sigma$ | $\delta$ | $\sigma$ |                       |
| 1 <sup>st</sup> | 0.013    | 8.11E-04 | 0.038    | 9.45E-03 | Logarithmic decrement |
| 2 <sup>nd</sup> | 0.014    | 7.22E-04 | 0.043    | 8.70E-03 |                       |
| 3 <sup>rd</sup> | -        | -        | 0.040    | 9.99E-03 |                       |
| 1 <sup>st</sup> | 0.009    | -        | 0.023    | -        | POD reconstruction    |
| 2 <sup>nd</sup> | 0.010    | -        | 0.023    | -        |                       |
| 3 <sup>rd</sup> | -        | -        | 0.022    | -        |                       |
|                 | 0.017    | -        | 0.025    | -        | Utsumi                |
|                 | 0.015    | -        | 0.022    | -        | Abramson              |

Table 5.4: Damping ratios

### 5.2.3 DMD

Despite the DMD results being unsatisfactory, it is worth mentioning the results obtained in terms of eigenvalues. Figure (5.11) shows the unit circle in the complex plane, black dots represent the eigenvalues derived from the DMD analysis. DMD modes time dynamics can be predicted according to the absolute value of the eigenvalues:

- if  $|\lambda_r| = 1$  the modes are purely harmonic, unlike DFT the frequency associated to each mode is not forced to be a multiple of the fundamental one  $f_0 = 1/T$  where  $T = n_t \Delta t$  is the observation time
- if  $|\lambda_r| < 1$  the modes decay in time
- if  $|\lambda_r| > 1$  the modes grow in time

Considering the unit complex circle, the most relevant modes are those close to the circle's edge because the magnitude of  $\lambda_r$  is very close to the unit, and therefore they are nearly harmonic. The modes whose eigenvalues are very close to the unit, take more time to vanish. Since the test case under exam is damping, for sure there will be a mode with zero imaginary part, that will decay without oscillation. The other relevant ones are all complex, characterised by a real and an imaginary part that corresponds to the mode's decaying and oscillatory behaviour, respectively.

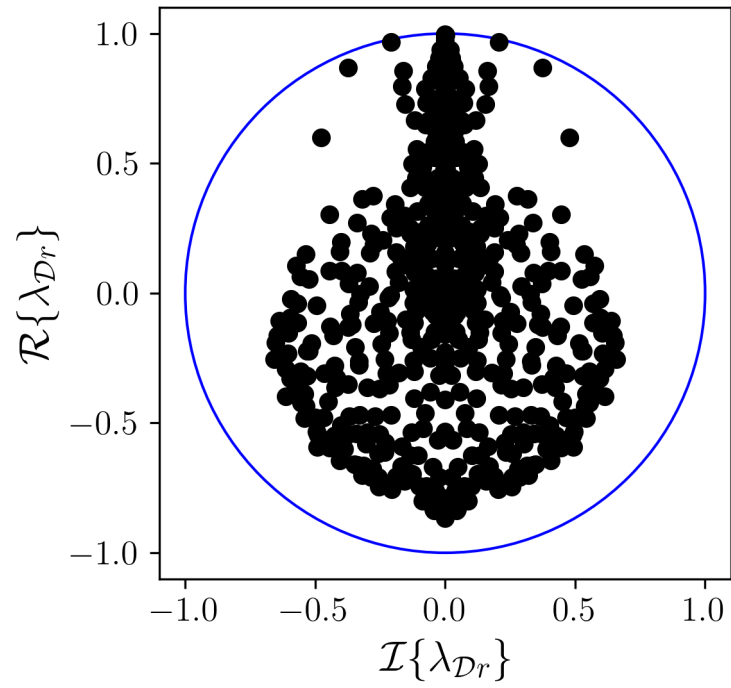
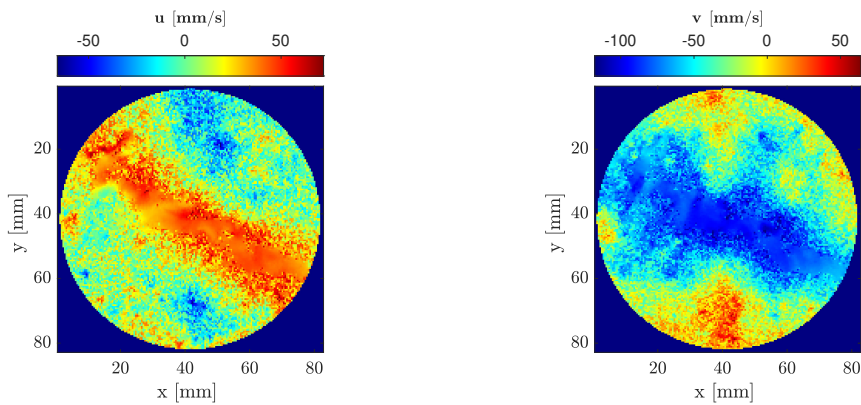


**Figure 5.11:** Eigenvalues in the unit complex circle

## 5.3 Swirl mode

### 5.3.1 Damping maps

Only the HFE7200 was tested in the swirl mode. The analysis conducted for this mode is similar to the previous one. It is worth remark that for the swirl mode campaign the camera was placed above the cylinder, to record the transversal plane. First, the fluid velocity field in terms of  $u$  and  $v$  component has been reconstructed. Figure (5.12) illustrates the first time instants as an examples.



(a) *HFE7200 u component first time instant snapshot* (b) *HFE7200 v component first time instant snapshot*

**Figure 5.12:** Snapshots of the first time instants of  $u$  and  $v$  component in the swirl mode

The logarithmic decrement method is once again applied in order to obtain the damping maps

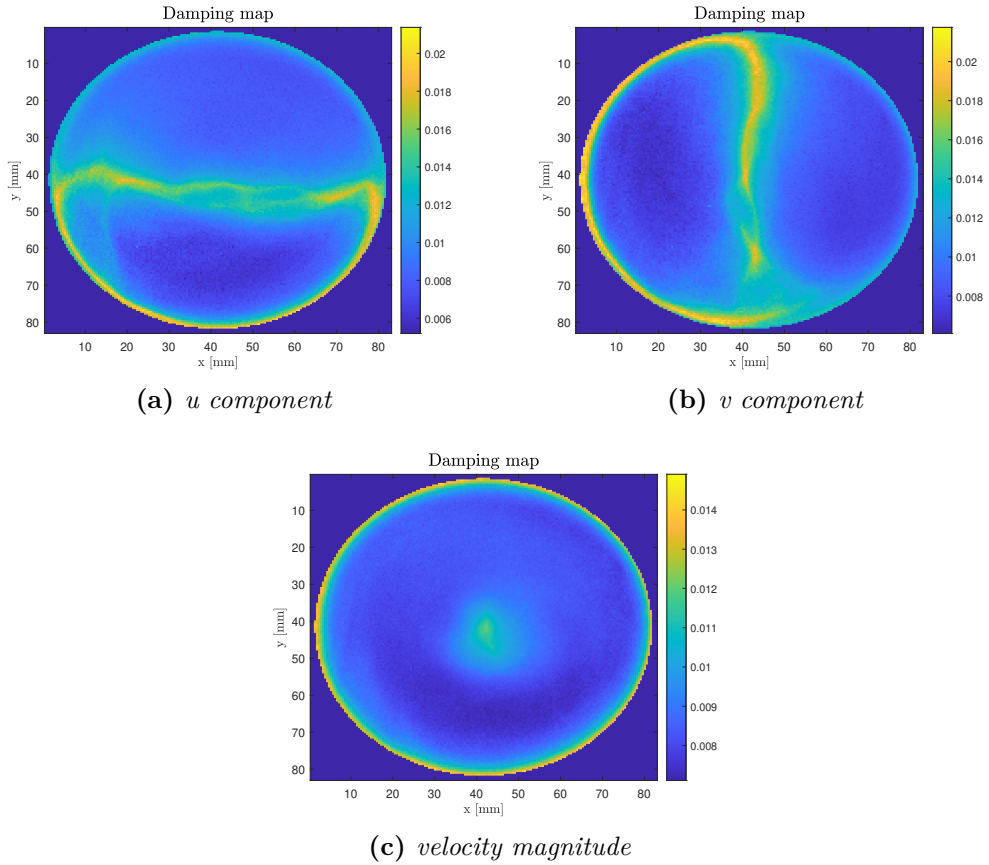
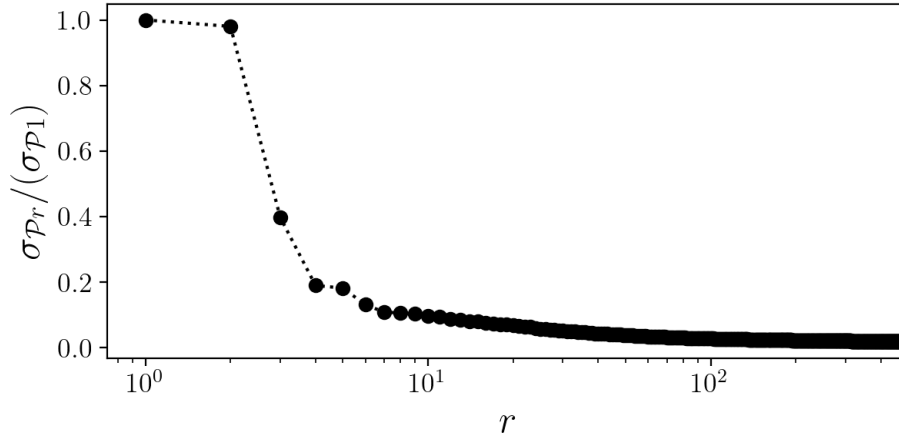


**Figure 5.13:** Damping maps HFE7200 swirl mode

The swirl mode produces higher damping ratios if compared to the ones of HFE7200 in the planar mode.

### 5.3.2 POD

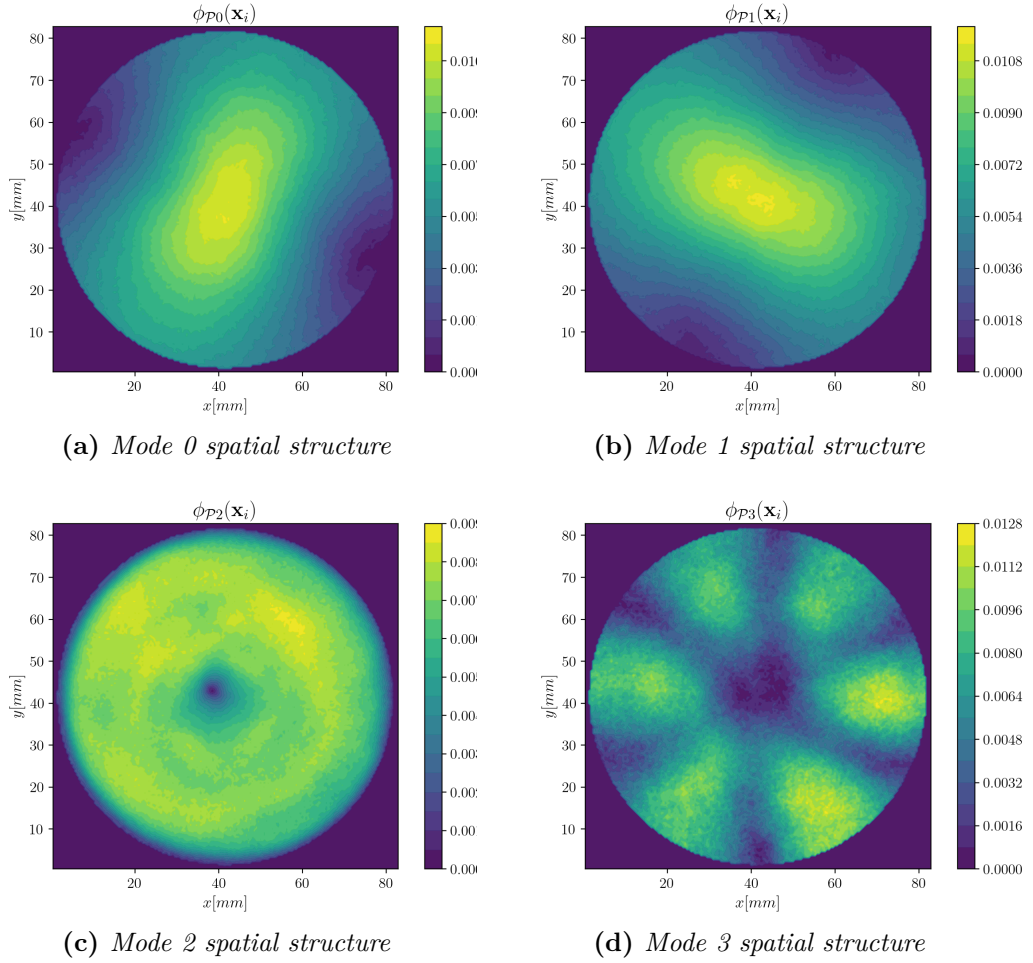
The same POD technique has been to the swirl mode, restricted to the first  $r = 500$  modes. The plot showing their normalized amplitudes  $\sigma_{\mathcal{P}_r}/\sigma_{\mathcal{P}_1}$  points out which are the prevalent modes in the sloshing motion.



**Figure 5.14:** Modes amplitude swirl mode HFE7200

Also in this case the majority of the normalized amplitudes' modes decays to zero, for this reason only the first four modes are considered relevant. From the selected modes, as previously, the following features are extracted:

## 1. the spatial structures

**Figure 5.15:** Spatial structures HFE7200 swirl mode

In reference to figure (5.15) modes 0 and 1 have very similar spatial structures; the only difference is that they are rotated at  $90^\circ$  one respect each other. Instead, the spatial structure related to mode 2 seems to be the proper swirling one. Finally, the last one may be interpreted as the composition of the fundamental harmonic, as evidenced by the peak in the Fast Fourier Transform of the temporal structures.

## 2. the temporal structures

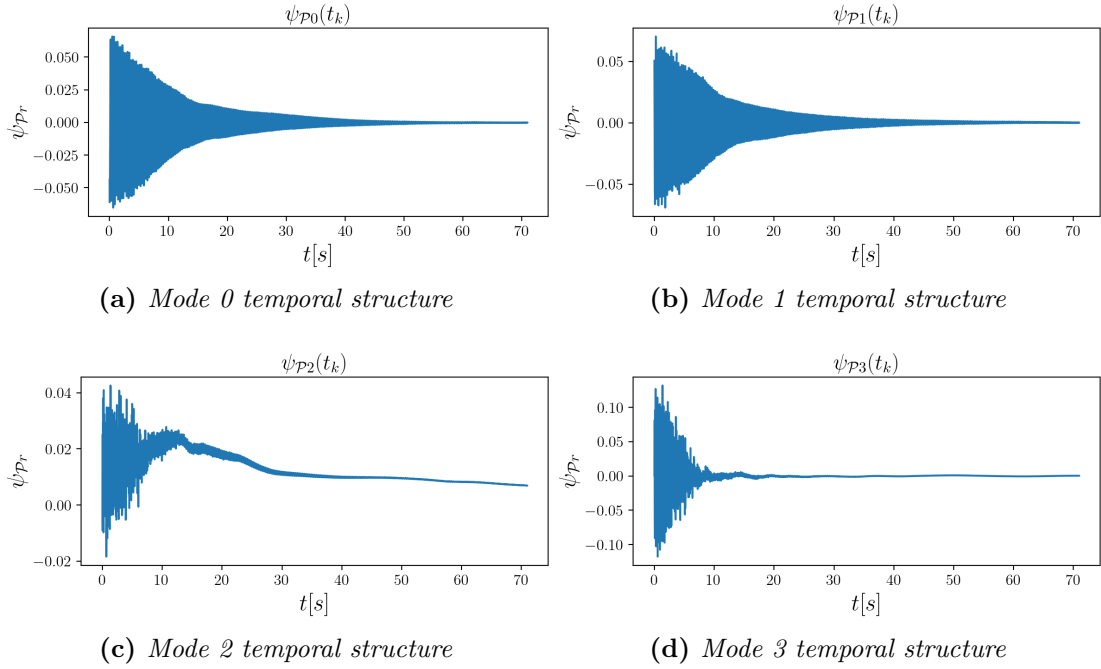


**Figure 5.16:** Temporal structures HFE7200 swirl mode

Looking at figure (5.16) it is evident that the temporal structure related to modes 0 and 1 are very similar, they oscillate around zero and decay in time since the first time instant. Instead, the temporal structure related to mode 2 starts to decay 10 s later the previous ones. Finally, the last one decays in few seconds (the first 10 s) this means that this mode is the less relevant among the selected ones.

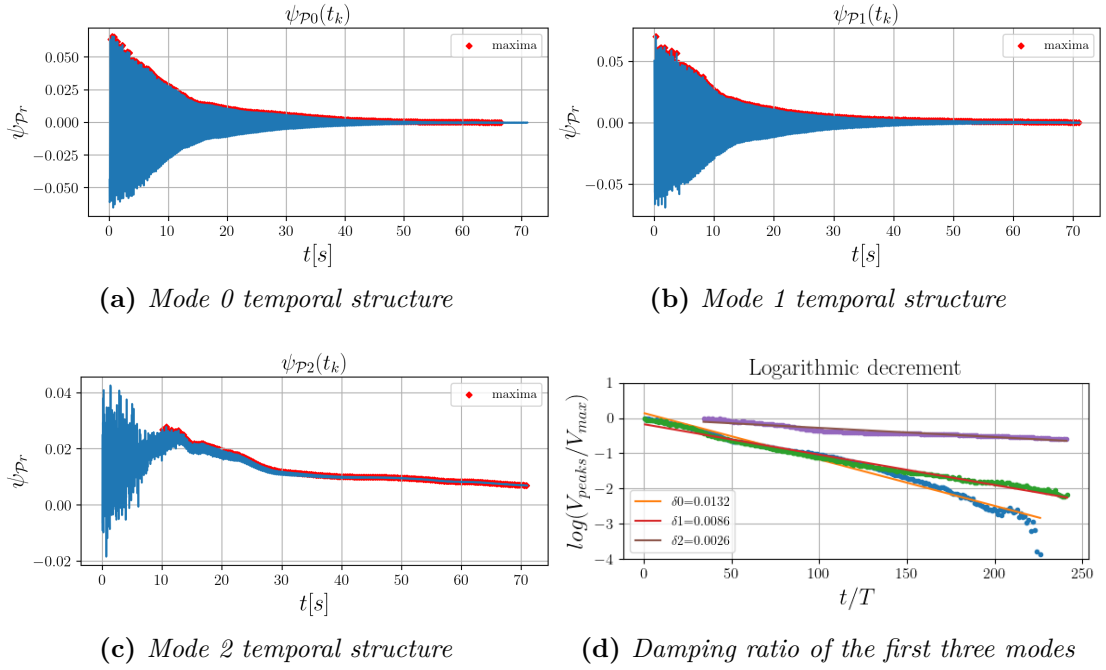


**Figure 5.17:** Logarithmic decrement method applied to the temporal structures of HFE7200 swirl mode

Selecting the positive peaks of the modes' temporal structures, it can be applied the logarithmic decrement method. In particular, it is applied on modes 0,1 and 2 because they show an exponential decay in time. As previously stated, mode 2 starts damping after the first 10s, for this reason peaks were selected starting from  $t = 10s$ . It is worth noting that damping ratios related to mode 0 and 1 are remarkably comparable in figure (5.17), as well as the corresponding temporal structures. Instead, the estimation arising from mode 2 is quite different. Finally, comparing the results with the ones predicted by the theoretical model, the limits of the model are highlighted because for the swirling mode it commits a wider error. Considering the assumptions on which the theoretical model is based, it is not suitable for non-linear motions. This is the explanation for the discrepancy between the theoretical value and the experimental one found in the swirl regime.

3. the spectrum related to the temporal structures

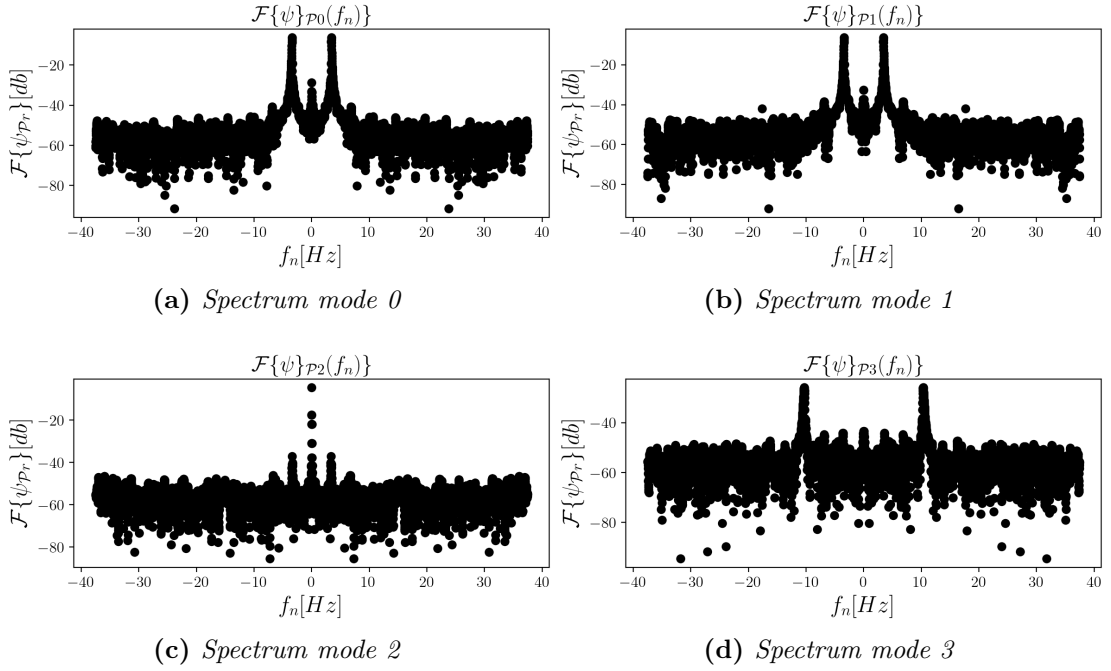


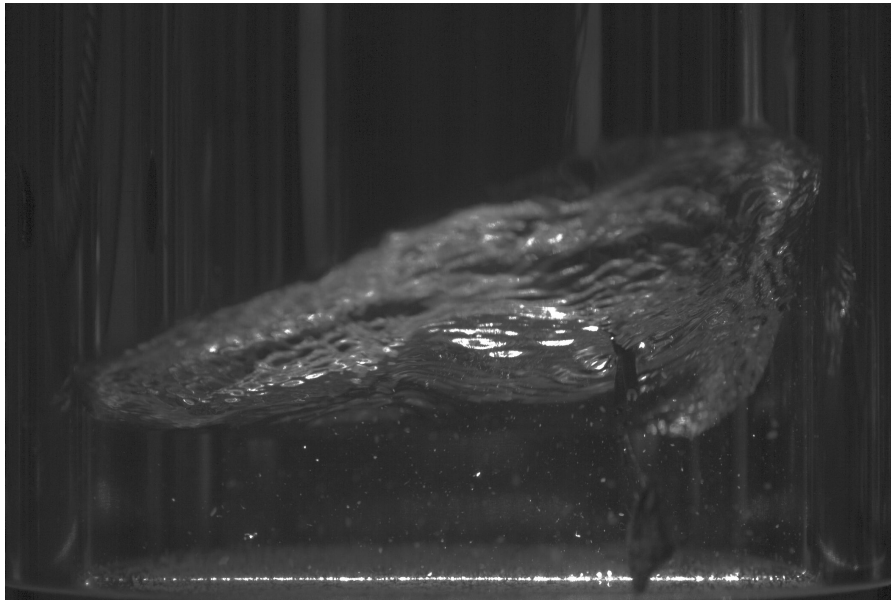
**Figure 5.18:** Spectra related to the temporal structures HFE7200 swirl mode

The peaks in the temporal structures' spectra indicate the most relevant frequencies of the analysed mode. The spectra related to mode 0 and 1 present a peak at  $f = 0 \text{ Hz}$  and  $f = 3.5 \text{ Hz}$  that is the external excitation frequency. Concerning mode 2, the peaks is at  $f = 3.4 \text{ Hz}$  that is the first natural frequency of the cylindrical container. This means that once the eternal excitation is stopped, according to mode 2 the system tends to the first natural frequency. Finally, the last spectrum shows the peaks at  $f = 10 \text{ Hz}$ , that is almost  $3 \times f_{nat}$  this aspect confirms that mode 3 can be interpreted as the third harmonic of the fundamental one.

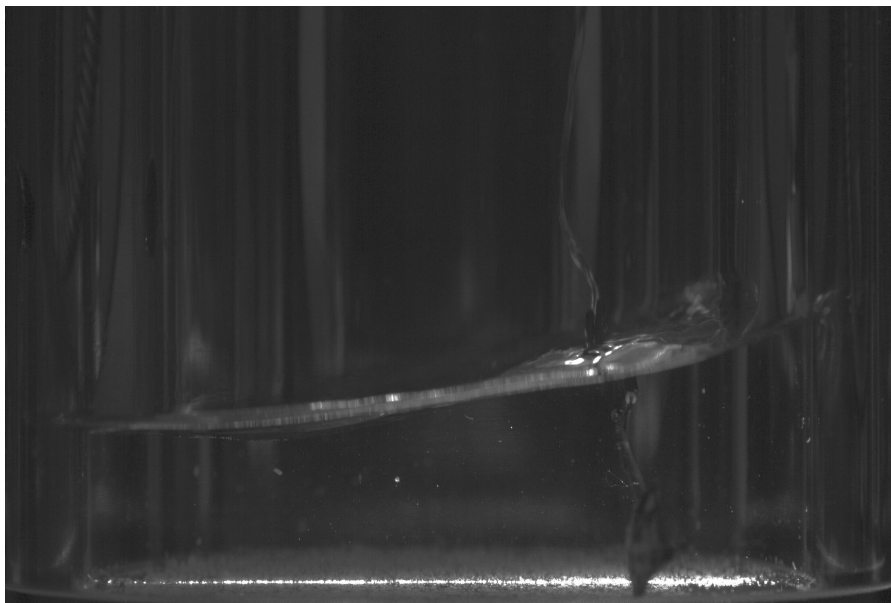
## 5.4 Cryogenics

The cryogenic experimental campaign was conducted to test the liquid nitrogen in the facility illustrated in chapter 3. The cryogenic campaign is time-demanding in terms of cool-down and keeping a stable temperature. During the execution of the experiment, some problems have been encountered, specifically during the filling of the reservoir. Probably humidity infiltrated in some pipes used to carry the liquid nitrogen from the tank to the cylinder, causing their freezing. For

this reason, the reservoir was filled for only about 2 *cm*, a too low height for sloshing visualizations. Nevertheless, images have been acquired just to visualize how the liquid nitrogen behaves under the imposed excitations. Two snapshots of the cryogenic experimental campaign are presented in the following figure for illustrative purposes only. In particular, figure (5.19)a depicts a snapshots of the interface configuration giving the planar signal in input. It is clear that in this case the *deep water conditions* explained in chapter 2 are not verified, because the  $LN_2$  reservoir is filled at a too-short height. Consequently, Miles' phase diagram is no more valid, this is the explanation why imposing the planar signal, it is observed a "swirl regime". Analogous considerations can be done considering figure (5.19)b, in this case it is imposed the chaotic regime. Nevertheless, an almost planar configuration is assumed by the interface.



(a)  $LN_2$  "planar" regime



(b)  $LN_2$  "chaotic" regime

**Figure 5.19:** Snapshots of  $LN_2$  giving in input two different signal, the planar the chaos

# Chapter 6

## Conclusions

The answer to the research question "how does viscosity affect damping?" was found through an experimental investigation. To reproduce the real case (a full-size tank filled with liquid hydrogen), different fluids having different viscosities were compared. The details about the experimental techniques are provided in chapter 3. In particular, the PIV technique was applied rather than the LeDaR one, due to visibility issues of the particles in the acquired images. The tools used to post-process the data acquired in the experiments are documented in chapter 4. A `Matlab` toolbox was used to elaborate PIV images to extract the instantaneous planar fluid velocity fields. Once these fields have been obtained, damping ratio estimation has been done comparing different methods. In particular, the logarithmic decrement method, and the two main data-driven decompositions: POD and DMD. However, DMD showed a poor ability to reconstruct the fluid velocity field. Results arising from these techniques have been compared with the ones predicted by the theoretical model and the empirical formula found in the literature and illustrated in chapter 2. In conclusion, the theoretical model can provide reliable results concerning the HFE7200 liquid, conversely, it fails to predict the behaviour of water, due to the different viscosity values. The work conducted so far should be further developed testing the theoretical model for other filling ratios  $h/R$ . Indeed, in this experimental campaign, this parameter has been kept constant to the value  $h/R = 1.5$ . However, testing other points could highlight some limits of this theoretical model unexplored at the moment. Moreover, experiments should be repeated for the cryogenic case to compare a wider range of tested fluids and to understand if the theoretical model works properly with liquids of different nature (cryogenics). The comparison between HFE7200 and water has highlighted that the theoretical model fails to predict results when the water is tested. There is still uncertainty on what is the degree of reliability in providing the liquid nitrogen damping ratios. This is the reason why experiments should be repeated.

# Appendix A

## Measurements repeatability

The most important results for each sloshing regime are described in Chapter 5. However, certain tests were recorded twice to ensure that the signals were consistent. Other results are displayed and compared in this appendix.

### A.1 Planar mode

Two liquids were tested in the planar mode: HFE7200 and water. At least two tests were conducted for each liquid, with one additional test conducted in the case of water. The damping maps associated to the velocity magnitude  $|\vec{V}|$  are presented in the following because they provide a more complete view of the damping distribution along the container.

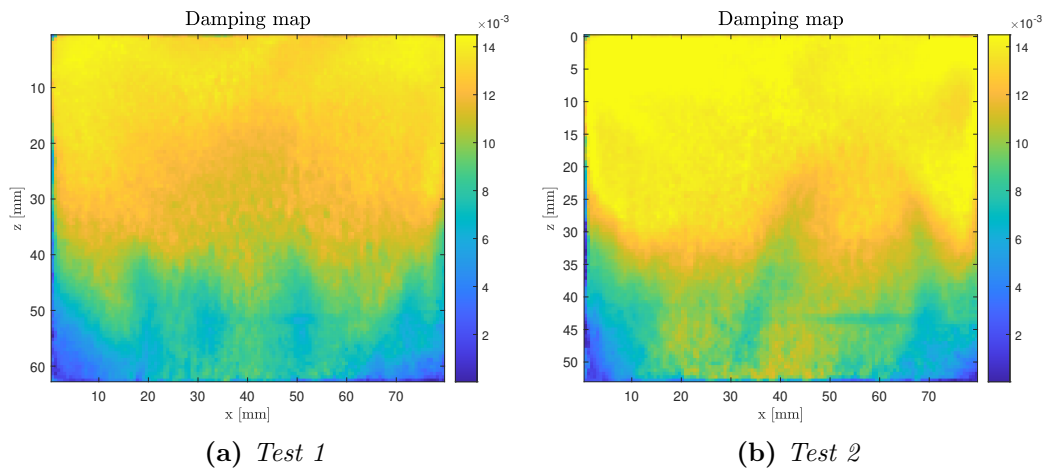


**Figure A.1:** Damping maps HFE7200 planar mode,  $|\vec{V}|$  velocity magnitude

Figure (A.1) shows that the damping ratio distribution is similar between the two tests. As discussed in chapter 5, the liquid experiences a stronger damping in the upper part of the reservoir because it is closer to the interface. While, proceeding towards the bottom, the liquid is almost at rest due to the no-slip conditions. There is a slight difference between the two tests: test 2 shows higher damping values in the first 30 mm of the container. The colorbar suggests that  $\delta \simeq 12 \cdot 10^{-3}$  in the first 30 mm of figure A.1.a, while  $\delta \simeq 14 \cdot 10^{-3}$  in the first 30 mm of figure A.1.b. This difference is normal because the starting conditions in each test are reproduced as closely as possible, but complete resemblance of the experiments cannot be achieved. Based on the two damping maps, it is possible to conclude that the repeatability of the planar mode signal is confirmed for HFE7200.

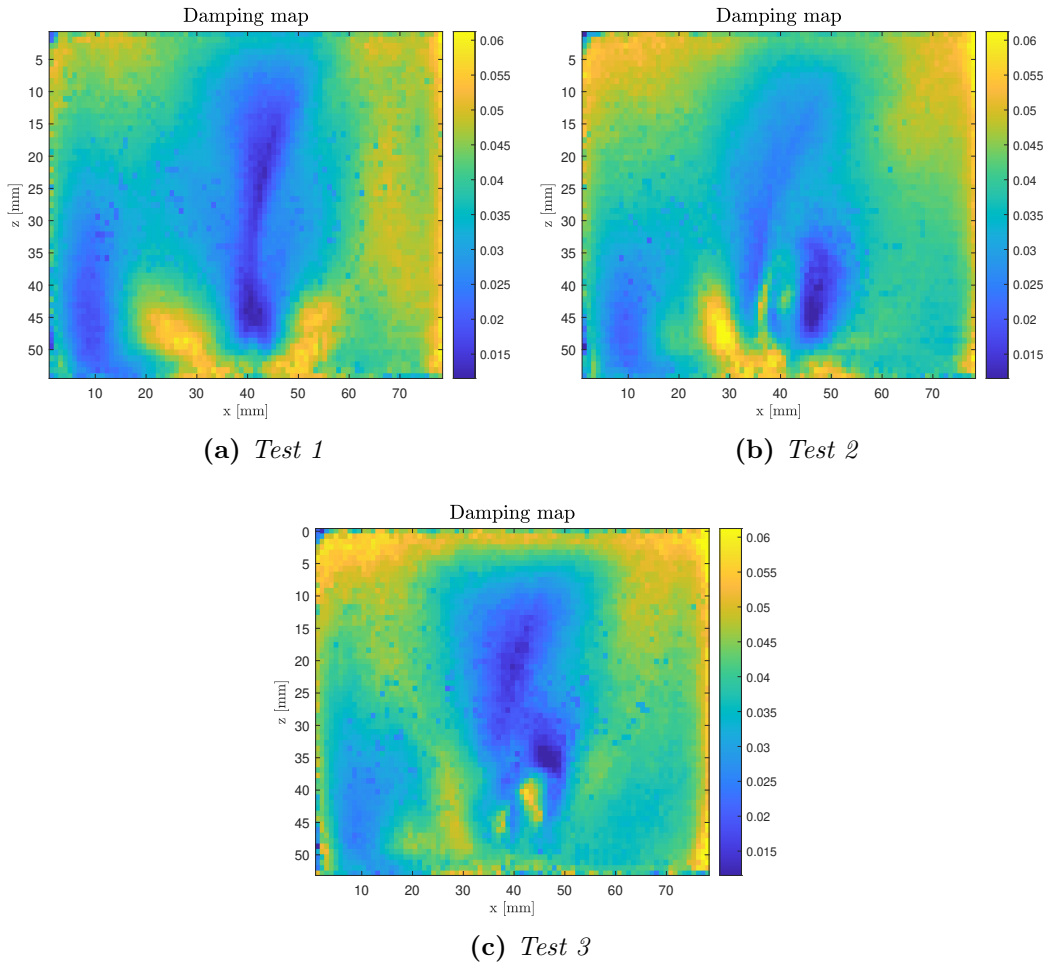


**Figure A.2:** Damping maps water planar mode,  $\vec{V}$  velocity magnitude

Considering figure (A.2), it is clear that the results are more sparse. In the

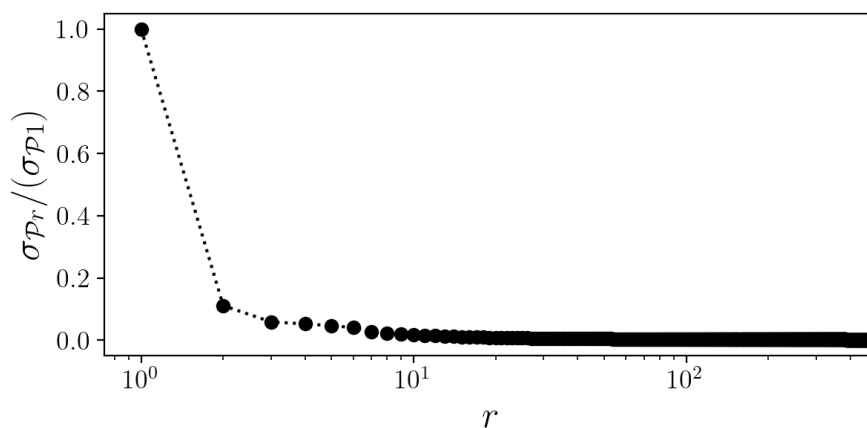
water case, damping ratio variability is more pronounced throughout the container, as previously stated in Chapter 5. This disparity can be attributed to two main reasons:

- when compared to HFE7200, water has a higher viscosity. This implies a higher damping ratio value and a shorter time required to damp the imposed motion. It was already mentioned in the results discussion that since water returns at rest conditions in about 10 s, this could have a negative impact on the results; meaning that a shorter time interval is considered when computing the velocity field through the cross-correlation algorithm, this might affect the fluid velocity fields and the damping ratio estimation as a consequence
- another issue concerns the experimental set-up. The seeding procedure, in particular, is one of the most critical parts of the experimental set-up, because it is difficult to obtain homogeneous seeding and to find the best particle combination that best reproduces the fluid's motion.

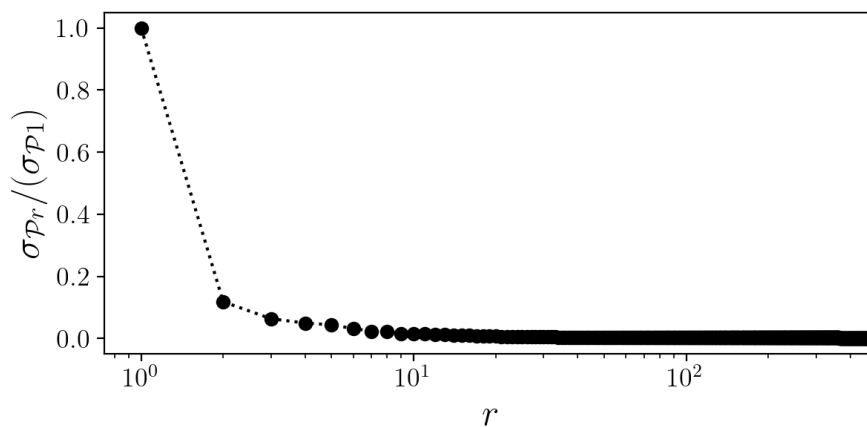
When the three maps are compared, test 1 and 2 are more similar in terms of the pattern shown in the damping map. Test 3, on the other hand, is quite different. However, the overall results for the three damping maps are unsatisfactory because a trend similar to HFE's maps was expected. The reasons could be those already mentioned.

## A.2 POD

The POD technique has been applied to all tests as well. The amplitude of modes in both HFE7200 tests is represented in Figure (A.3) The main difference is that mode 0 contains nearly 90% of the total energy, whereas the remaining modes have comparable energy content. In both cases, the first four modes were used to extract the spatial structures, temporal structures, and spectra, since they have the highest energetic contribution.

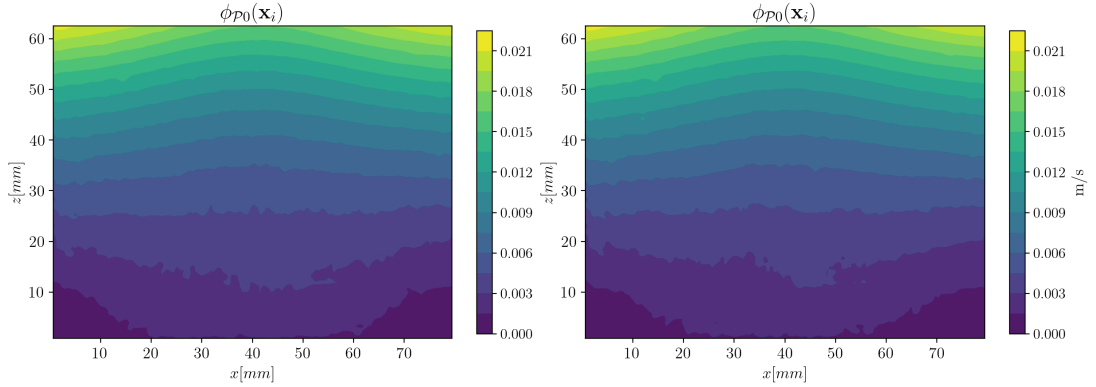


(a) HFE7200 test 1

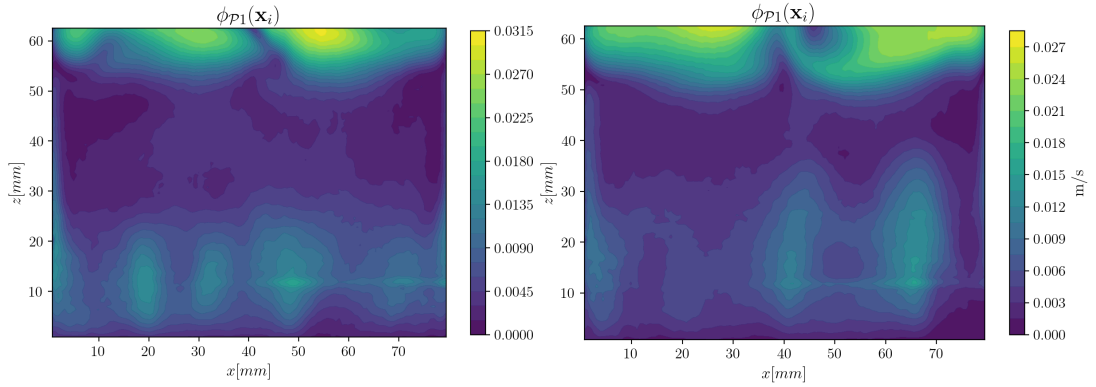


(b) HFE7200 test 2

**Figure A.3:** Modes' amplitude



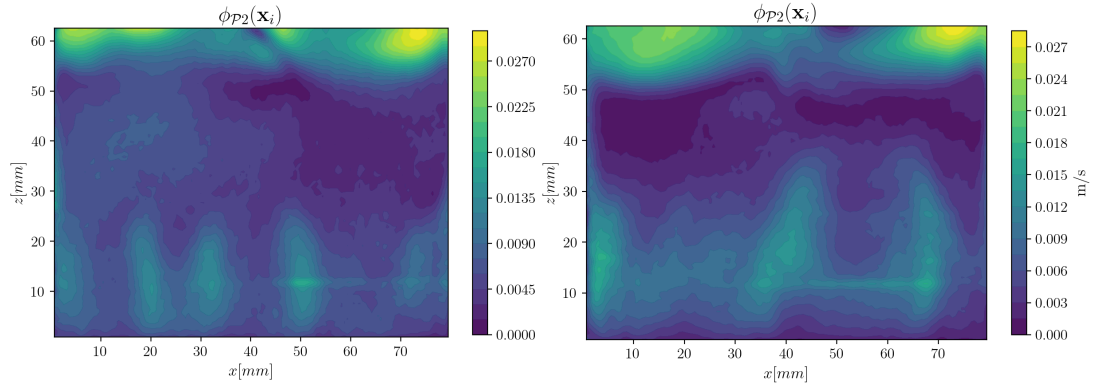
(a) HFE7200 test 1 spatial structure mode 0 (b) HFE7200 test 2 spatial structure mode 0



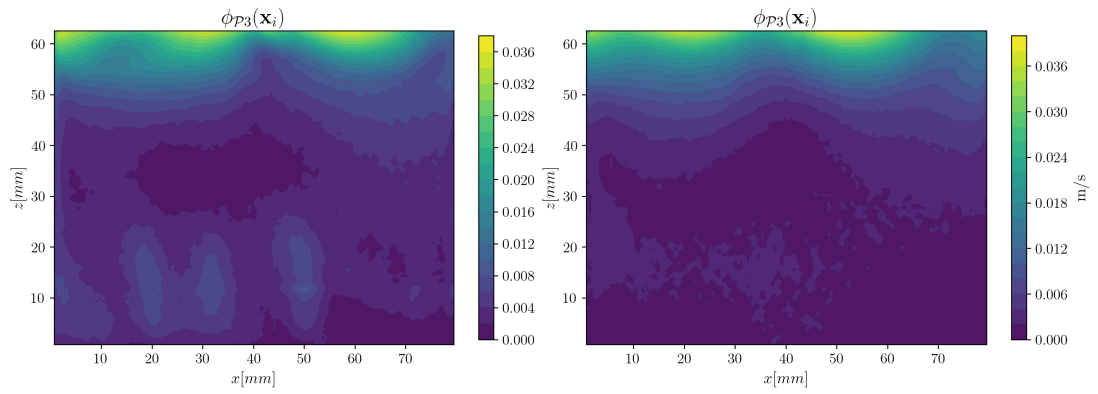
(c) HFE7200 test 1 spatial structure mode 1 (d) HFE7200 test 2 spatial structure mode 1

**Figure A.4:** Spatial structures planar mode. On the left HFE7200 test 1, on the right HFE7200 test 2

Figures (A.4) and (A.5) show the spatial structures of HFE7200. Comparing the two tests, the repeatability of each structure is respected in terms of pattern distribution.



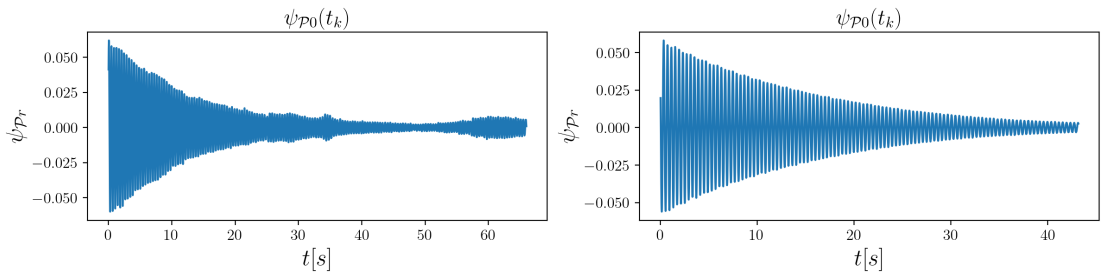
(a) HFE7200 test 1 spatial structure mode 2 (b) HFE7200 test 2 spatial structure mode 2



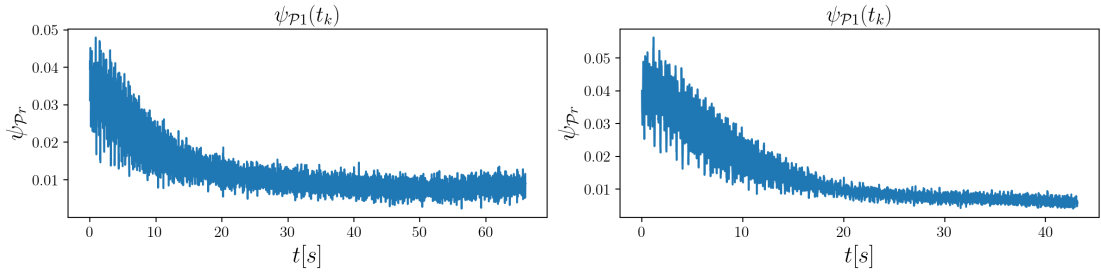
(c) HFE7200 test 1 spatial structure mode 3 (d) HFE7200 test 2 spatial structure mode 3

**Figure A.5:** Spatial structures planar mode. On the left HFE7200 test 1, on the right HFE7200 test 2

Figures (A.6) and (A.7) show the temporal structures of HFE7200. The reproducibility of each structure is also verified in this case.

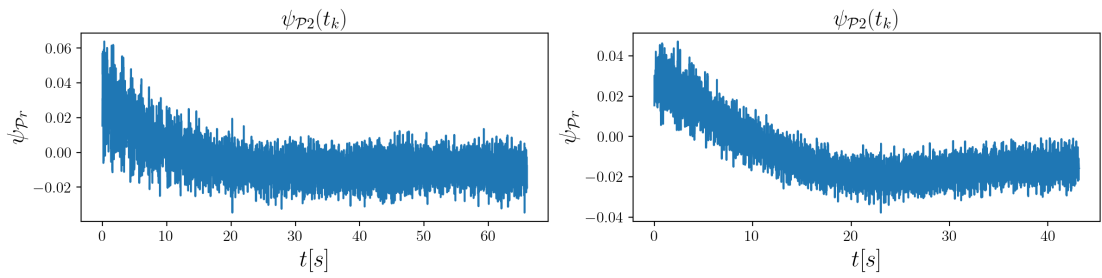


(a) HFE7200 test 1 temporal structure mode 0 (b) HFE7200 test 2 temporal structure mode 0

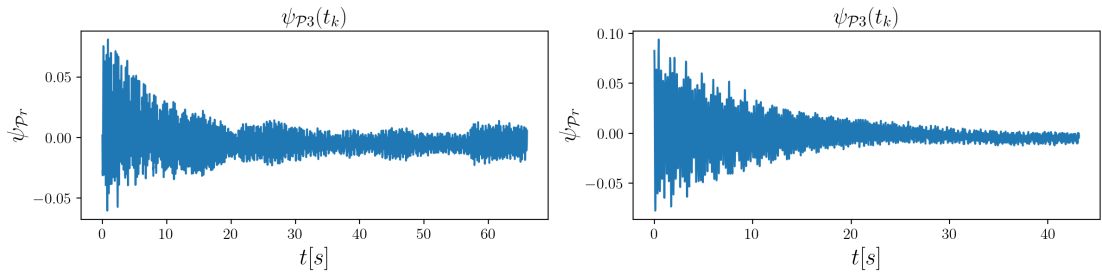


(c) HFE7200 test 1 temporal structure mode 1 (d) HFE7200 test 2 temporal structure mode 1

**Figure A.6:** Temporal structures planar mode. On the left HFE7200 test 1, on the right HFE720 test 2



(a) HFE7200 test 1 temporal structure mode 0 (b) HFE7200 test 2 temporal structure mode 0



(c) HFE7200 test 1 temporal structure mode 0 (d) HFE7200 test 2 temporal structure mode 0

**Figure A.7:** Temporal structures planar mode. On the left HFE7200 test 1, on the right HFE720 test 2

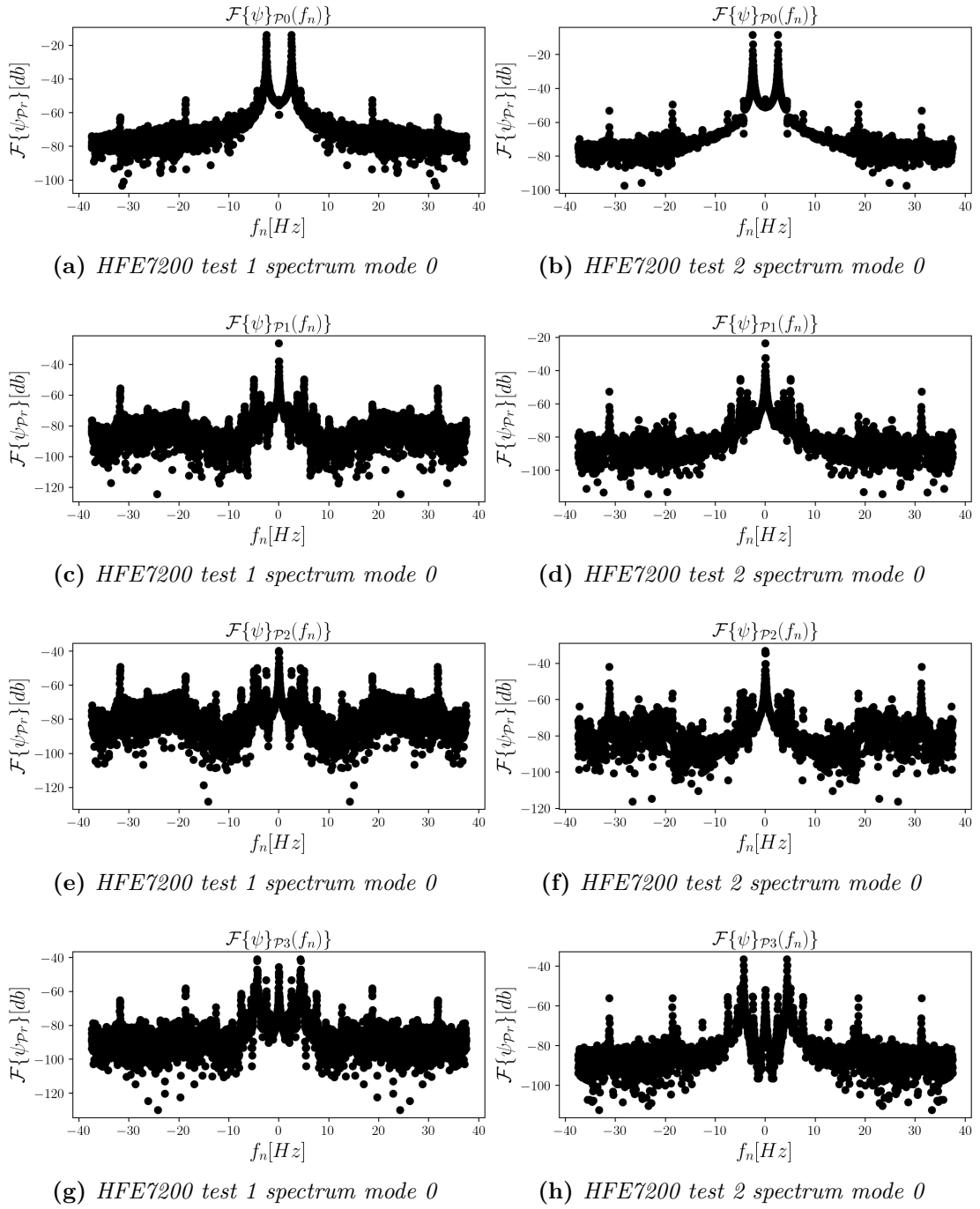


**Figure A.8:** Temporal structures' Fast Fourier Transform planar mode. On the left HFE7200 test 1, on the right HFE7200 test 2

In figure (A.9) the logarithmic decrement method has been applied to HFE7200 mode 0 of both tests. The damping ratio provided are similar, thus the repeatability of the temporal structures is once again confirmed.

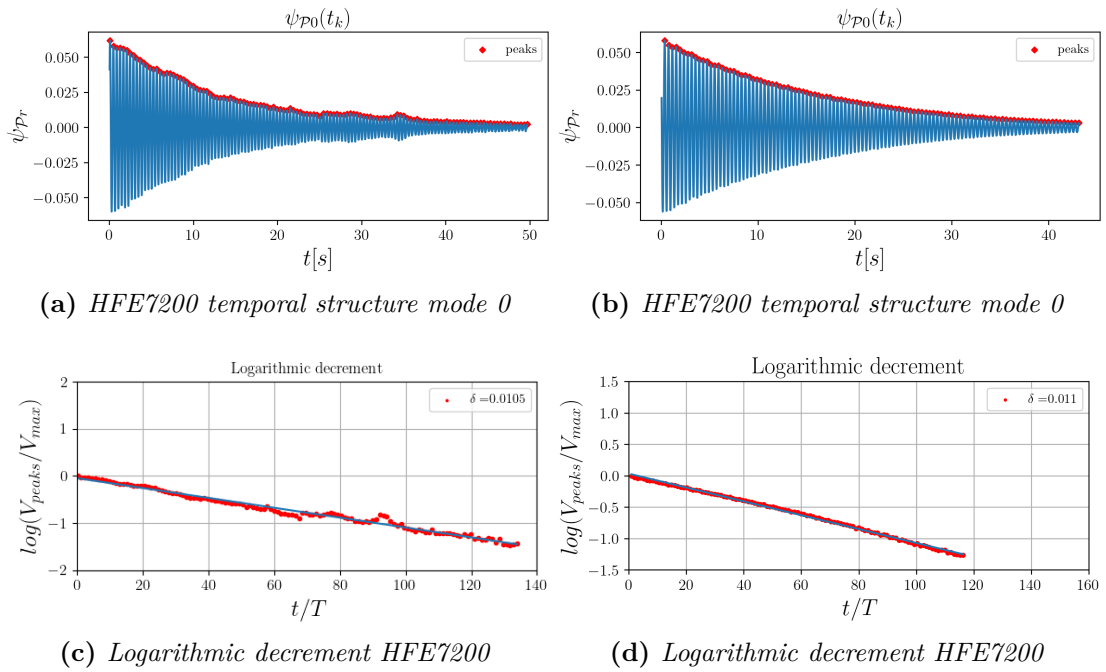
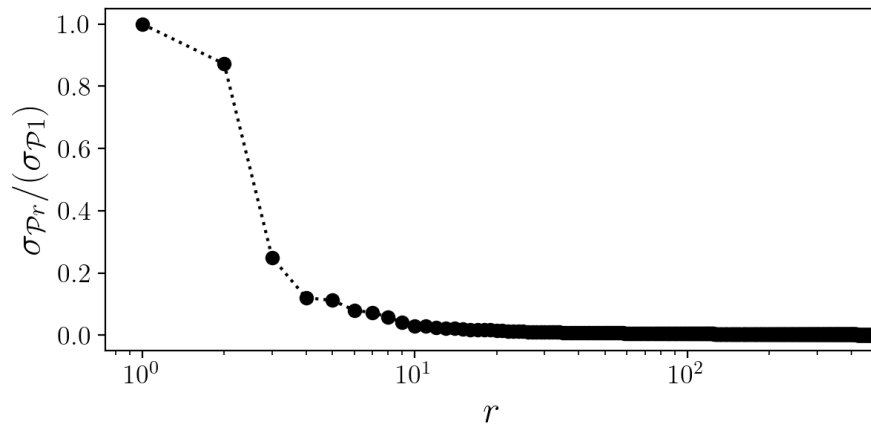
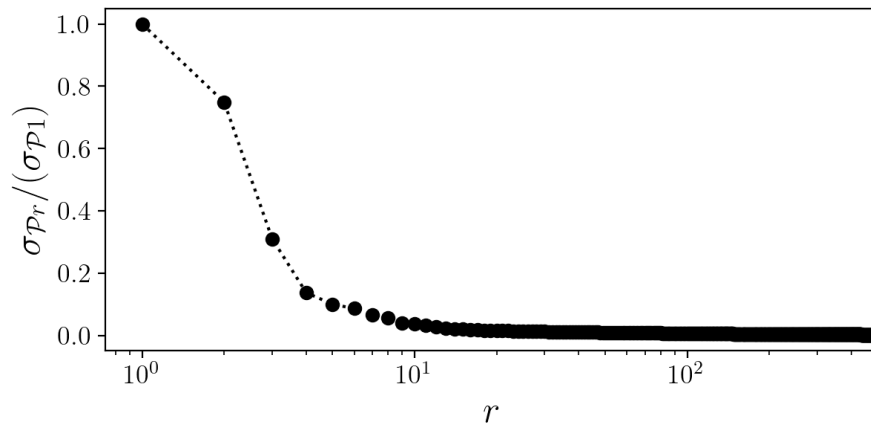


**Figure A.9:** Logarithmic decrement method. On the left HFE7200 test 1, on the right HFE7200 test 2

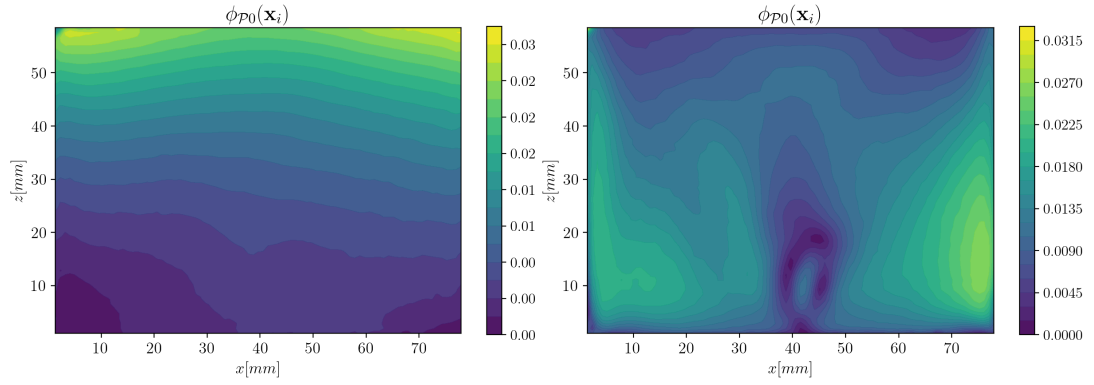


(a) Water test 2

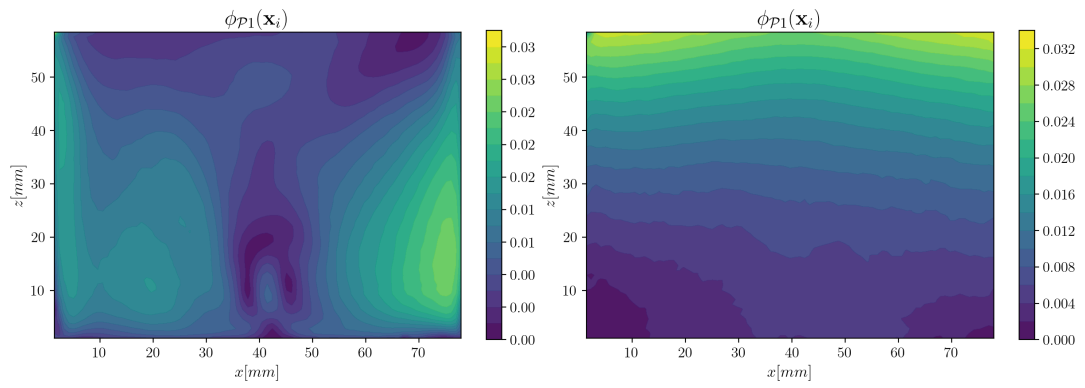


(b) Water test 3

Figure A.10: Modes' amplitude

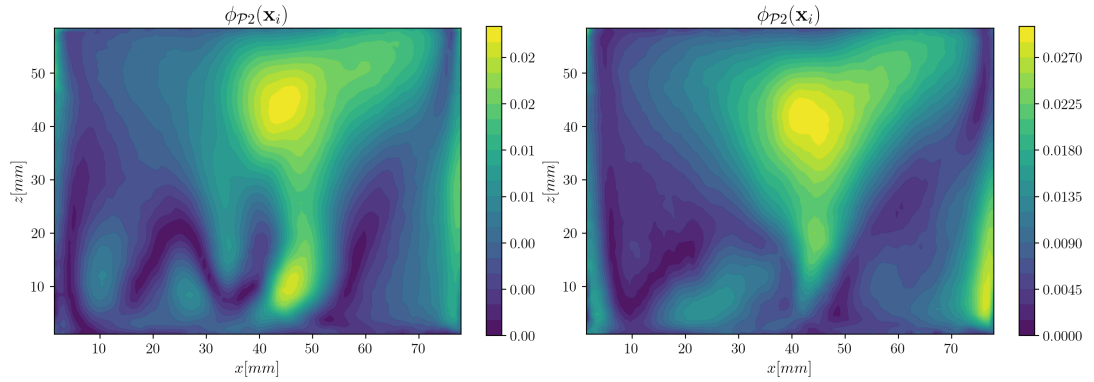


(a) Water test 2 spatial structure mode 0      (b) Water test 3 spatial structure mode 0

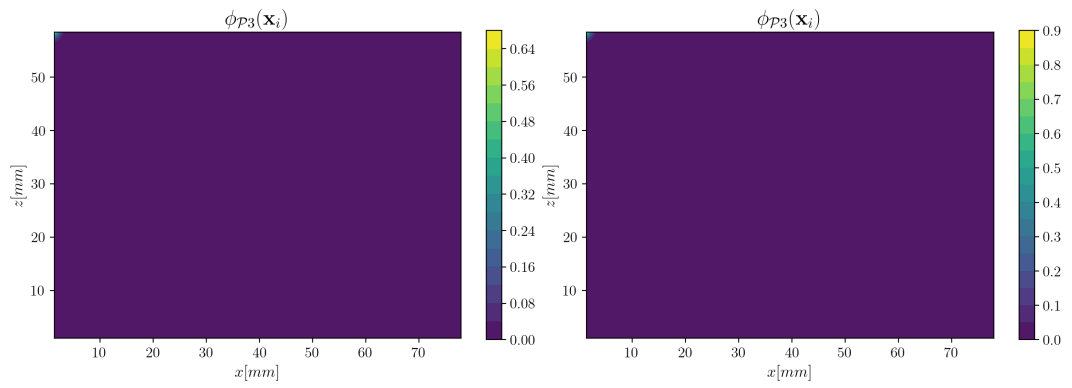


(c) Water test 2 spatial structure mode 1      (d) Water test 3 spatial structure mode 1

**Figure A.11:** Spatial structures planar mode. On the left water test 2, on the right water test 3



(a) Water test 2 spatial structure mode 2      (b) Water test 3 spatial structure mode 2



(c) Water test 2 spatial structure mode 3      (d) Water test 3 spatial structure mode 3

**Figure A.12:** Spatial structures planar mode. On the left water test 2, on the right water test 3

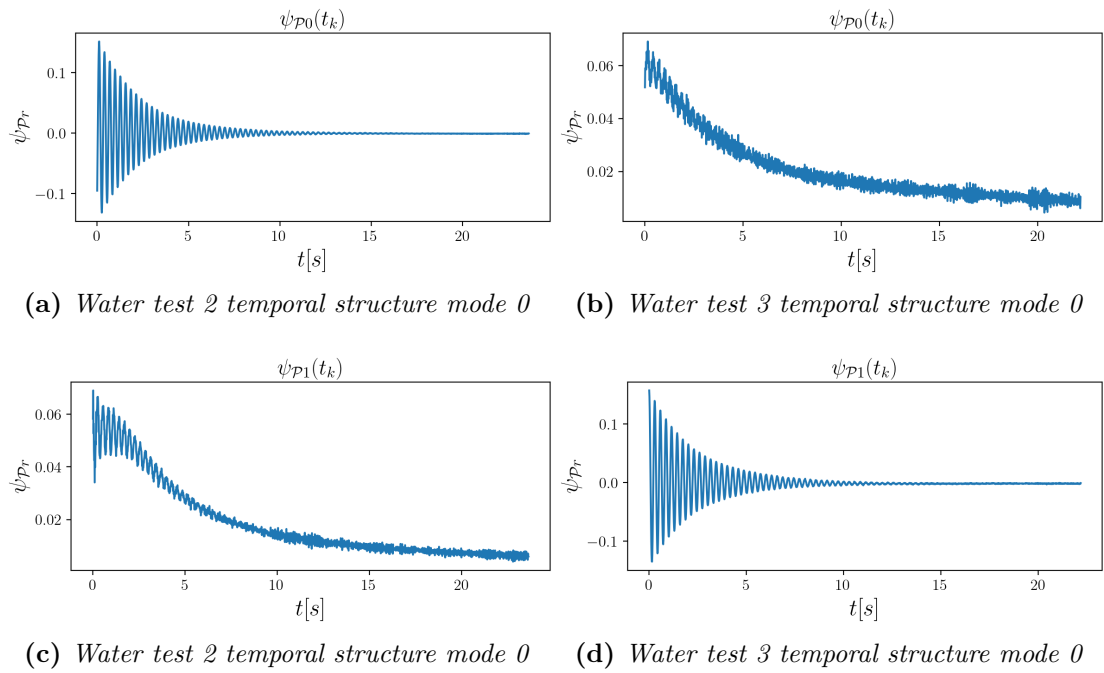


**Figure A.13:** Temporal structures planar mode. On the left water test 2, on the right water test 3

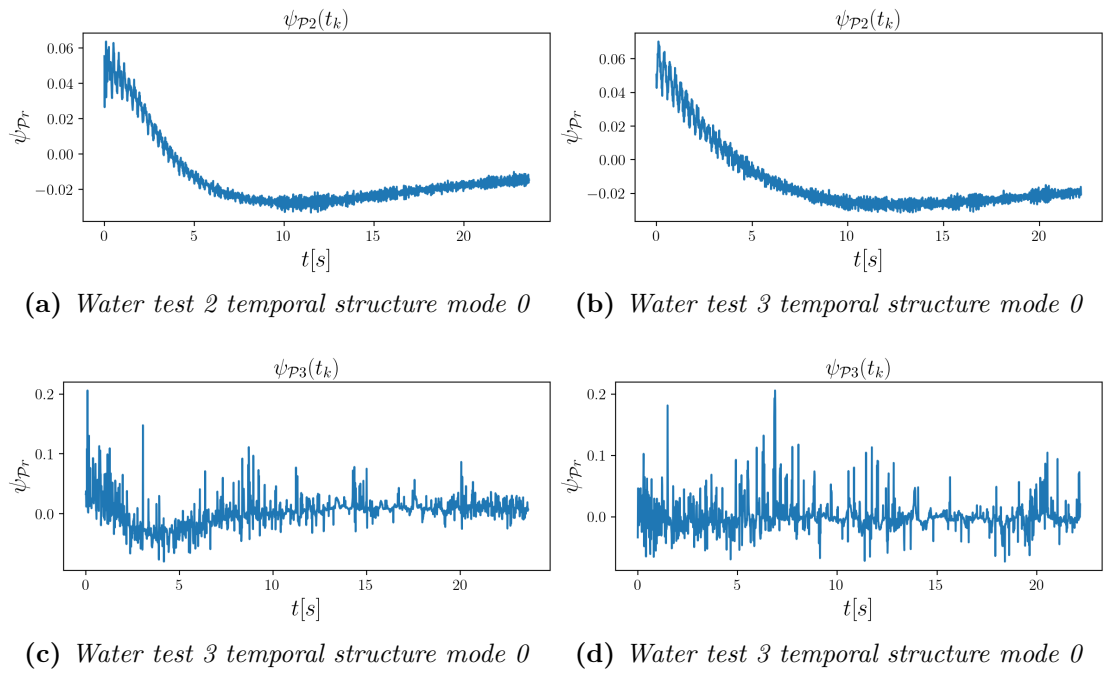


**Figure A.14:** Temporal structures planar mode. On the left water test 2, on the right water test 3

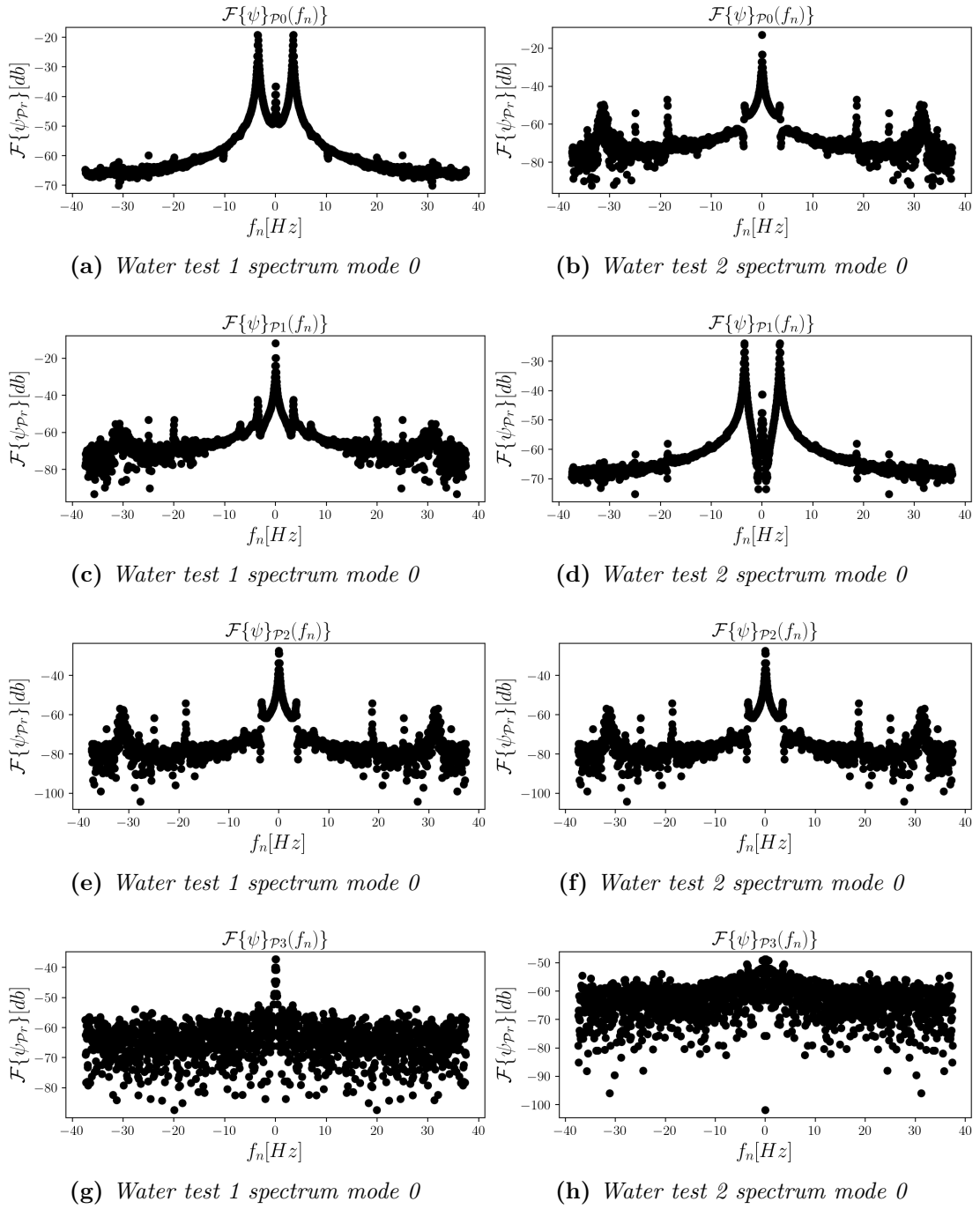


**Figure A.15:** Temporal structures' Fast Fourier Transform planar mode. On the left water test 2, on the right water test 3

In figure (A.16) the logarithmic decrement method has been applied on mode 1 of test 2 and 3. Besides the repeatability issues encountered in the damping maps, the logarithmic decrement method provides two different  $\delta$  values.

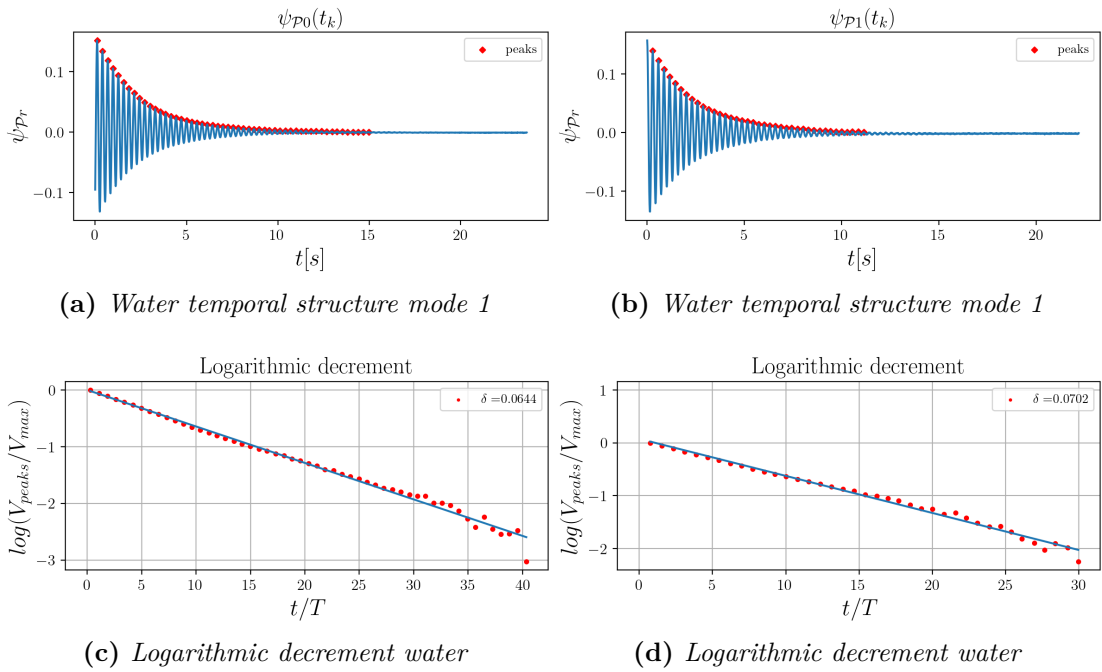


**Figure A.16:** Logarithmic decrement method. On the left water test 2, on the right water test 3

### A.3 Swirl mode

Only the HFE7200 was tested in the swirl mode. Two tests were carried out to ensure the signal's repeatability. The damping maps related to the velocity magnitude  $\vec{V}$ , are shown below because they provide a more complete view of the damping distribution on the transversal plane. Figure (A.17) shows that the damping ratio distribution is similar between the two tests. In this case, the signal's repeatability is confirmed.

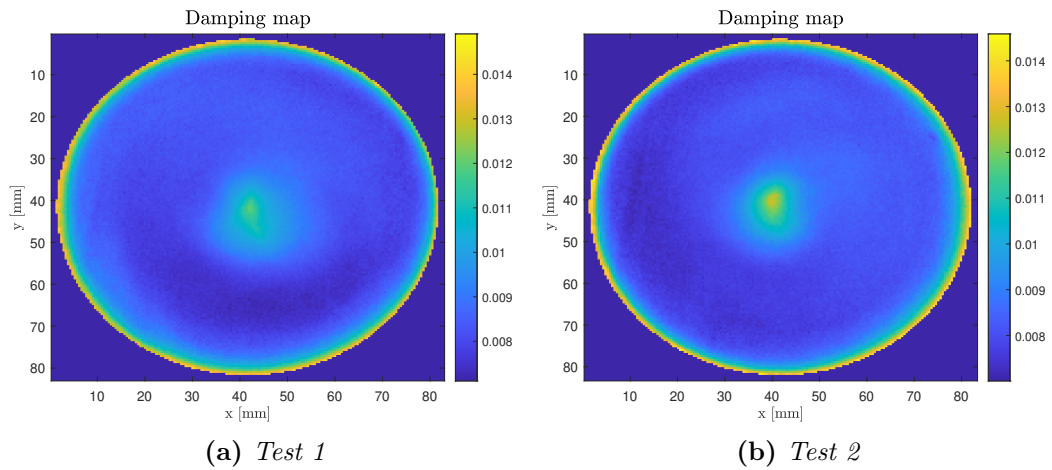
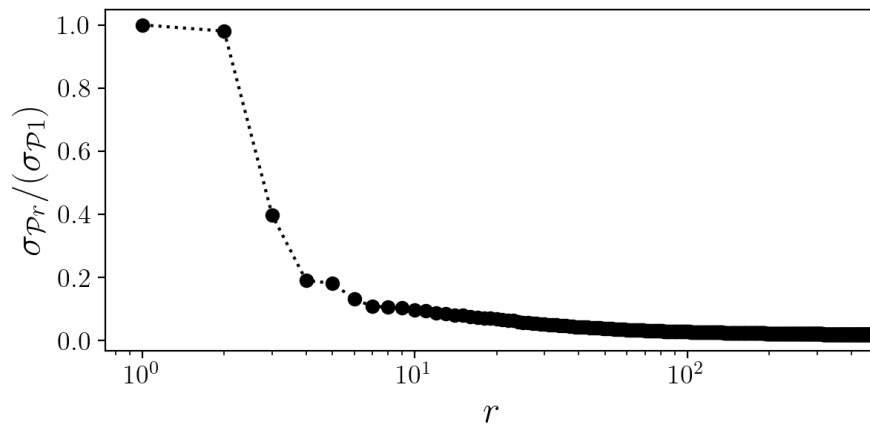


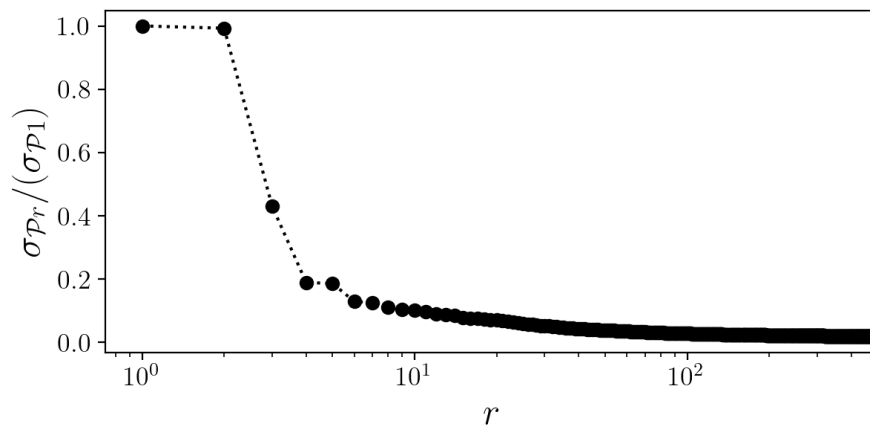
**Figure A.17:** Damping maps HFE7200 swirl mode,  $\vec{V}$  velocity magnitude

## A.4 POD

The POD technique has been applied to both tests as well. Figure (A.18) shows that the first two modes contain most of the energy in the swirl mode case. In terms of energy content, the first four modes are considered relevant for the current POD analysis.



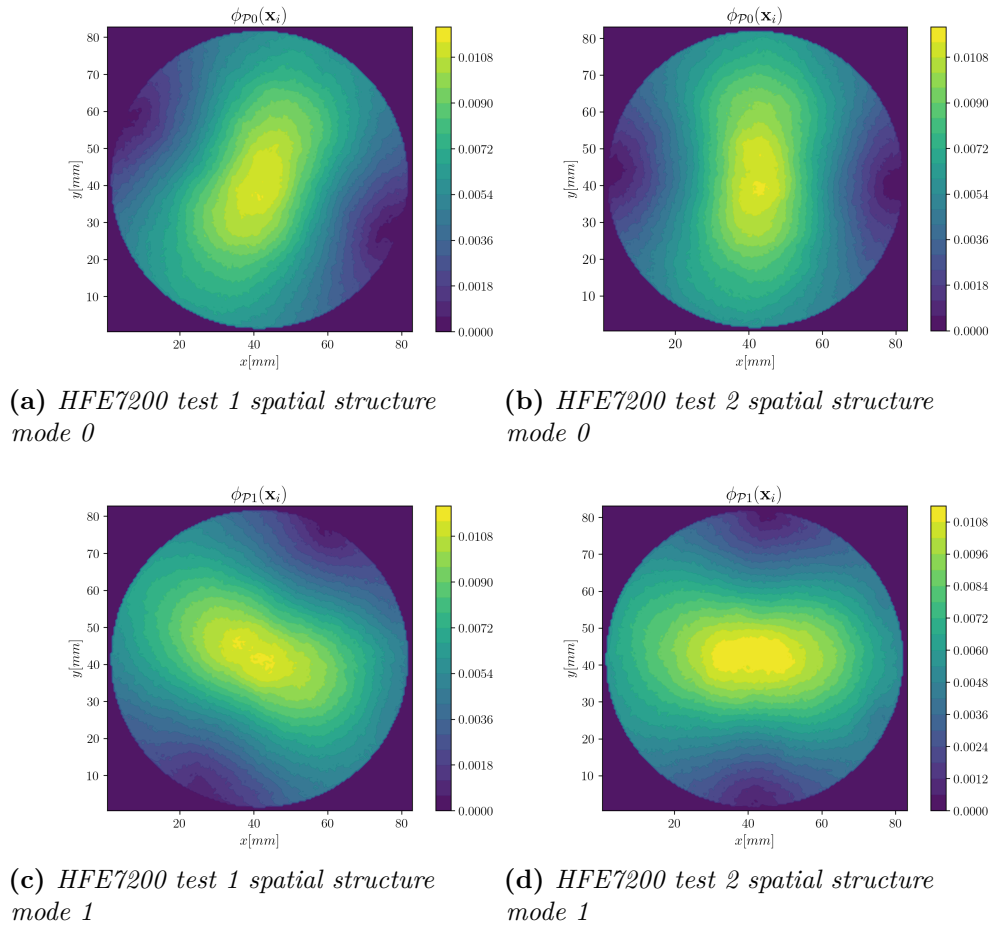
(a) HFE7200 test 1



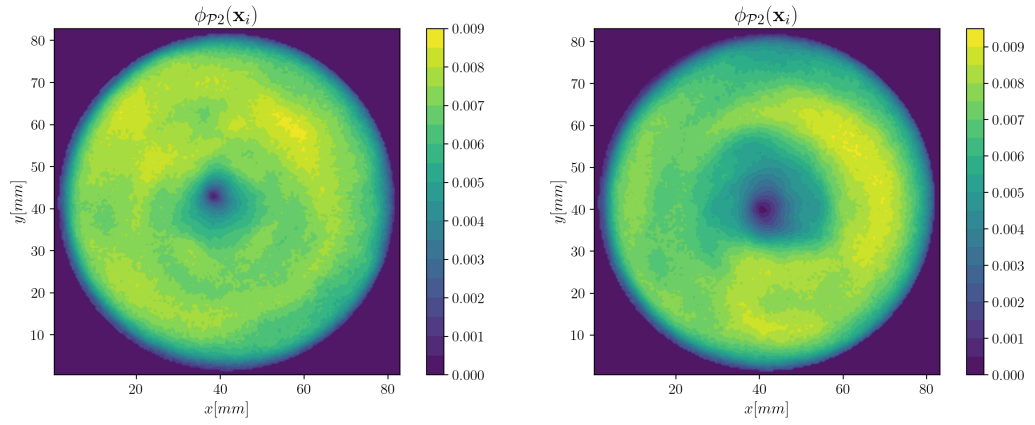
(b) HFE7200 test 2

Figure A.18: Modes' amplitude

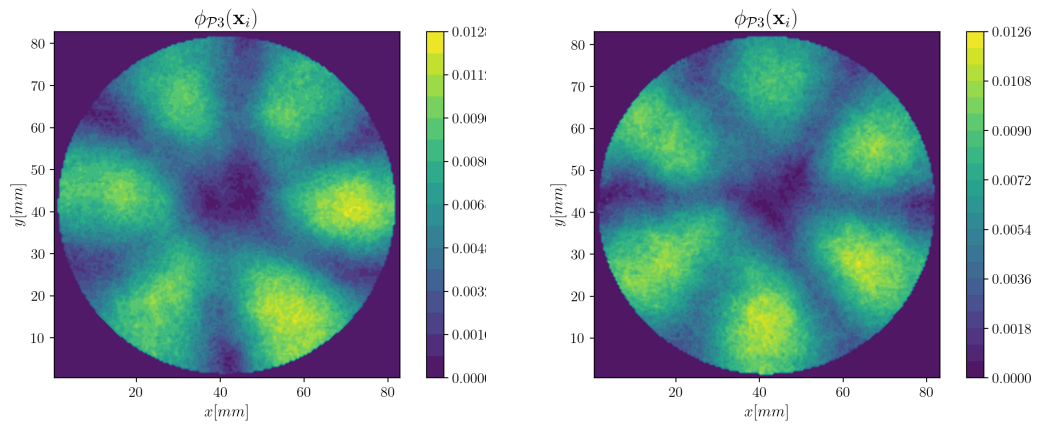
Figures (A.19) and (A.20) compare the spatial structures of the two tests. In terms of  $\Phi$  magnitude the repeatability is confirmed. Taking into account the spatial distribution, modes are slightly rotated one respect each other between the two tests.



**Figure A.19:** Spatial structures swirl mode. On the left HFE7200 test 1, on the right HFE7200 test 2



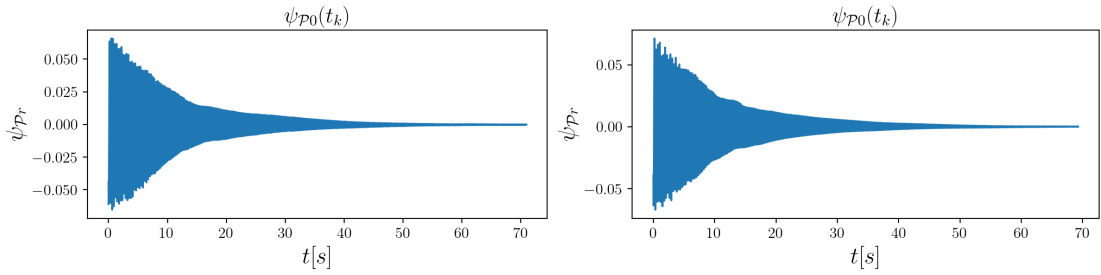
(a) *HFE7200 test 1 spatial structure mode 2* (b) *HFE7200 test 2 spatial structure mode 2*



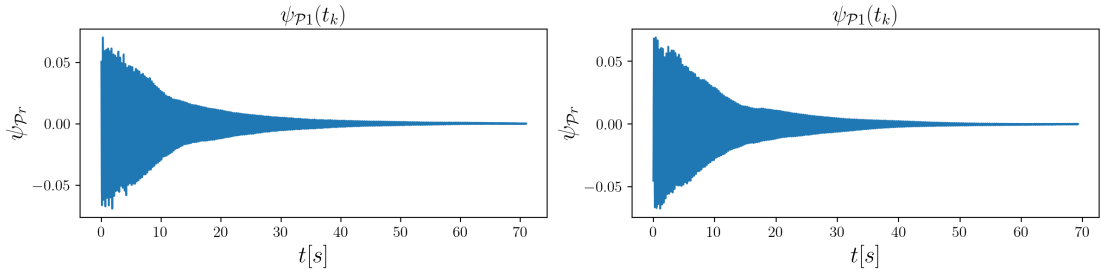
(c) *HFE7200 test 1 spatial structure mode 3* (d) *HFE7200 test 2 spatial structure mode 3*

**Figure A.20:** Spatial structures swirl mode. On the left HFE7200 test 1, on the right HFE7200 test 2

The temporal structures of the two tests are compared in figures (A.21) and (A.22). In both cases it can be noticed that mode 0 and 1 have a linear temporal decay. While mode 2 begins to decay after 10 s, its trend is nearly linear. Finally, mode 3 decays in a very short time (the first 10 s).

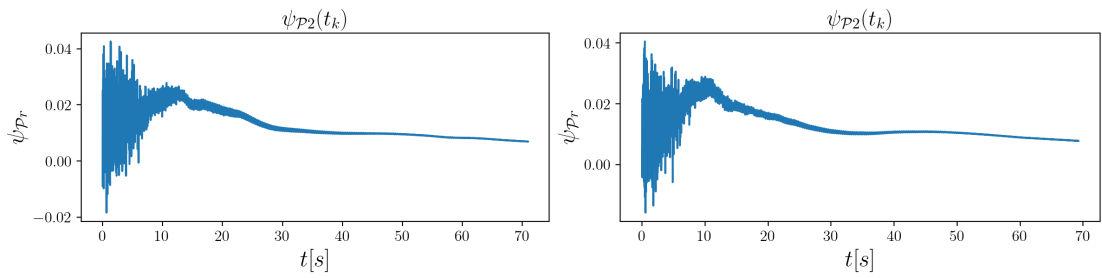


(a) HFE7200 test 1 temporal structure mode 0 (b) HFE7200 test 2 temporal structure mode 0

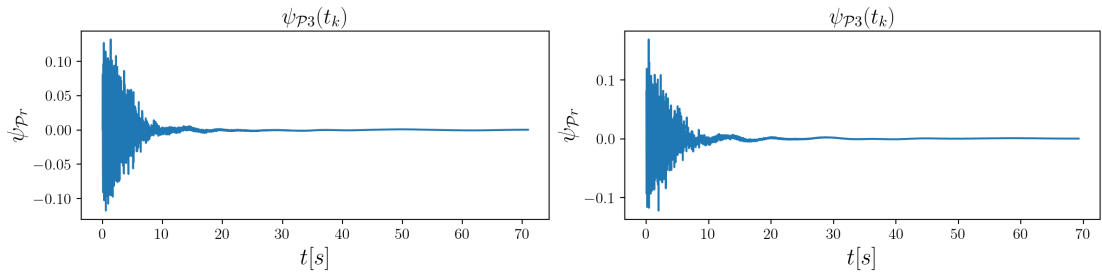


(c) HFE7200 test 1 temporal structure mode 1 (d) HFE7200 test 2 temporal structure mode 1

**Figure A.21:** Temporal structures swirl mode. On the left HFE7200 test 1, on the right HFE720 test 2



(a) HFE7200 test 1 temporal structure mode 0 (b) HFE7200 test 2 temporal structure mode 0



(c) HFE7200 test 1 temporal structure mode 0 (d) HFE7200 test 2 temporal structure mode 0

**Figure A.22:** Temporal structures swirl mode. On the left HFE7200 test 1, on the right HFE720 test 2

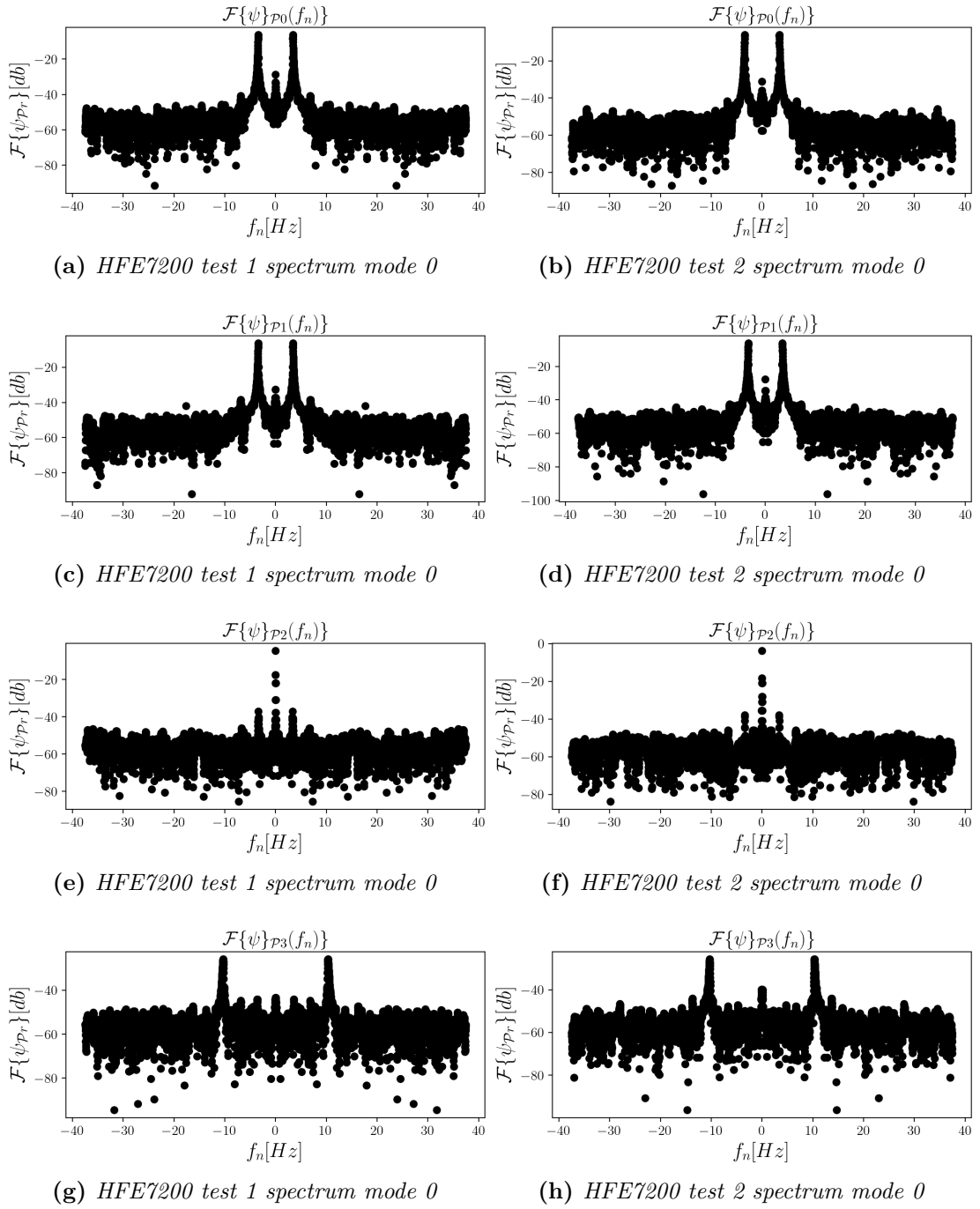


**Figure A.23:** Temporal structures' Fast Fourier Transform swirl mode. On the left HFE7200 test 1, on the right HFE7200 test 2

The logarithmic decrement method has been applied to the first three modes of both tests, as shown in figure (A.24). Considering a single test, the  $\delta$  value obtained is similar for modes 0 and 1, but it differs for mode 2. When each mode is compared between the two tests, the *delta* repeatability is confirmed in modes 0 and 2, while the results obtained for mode 1 are more variable.

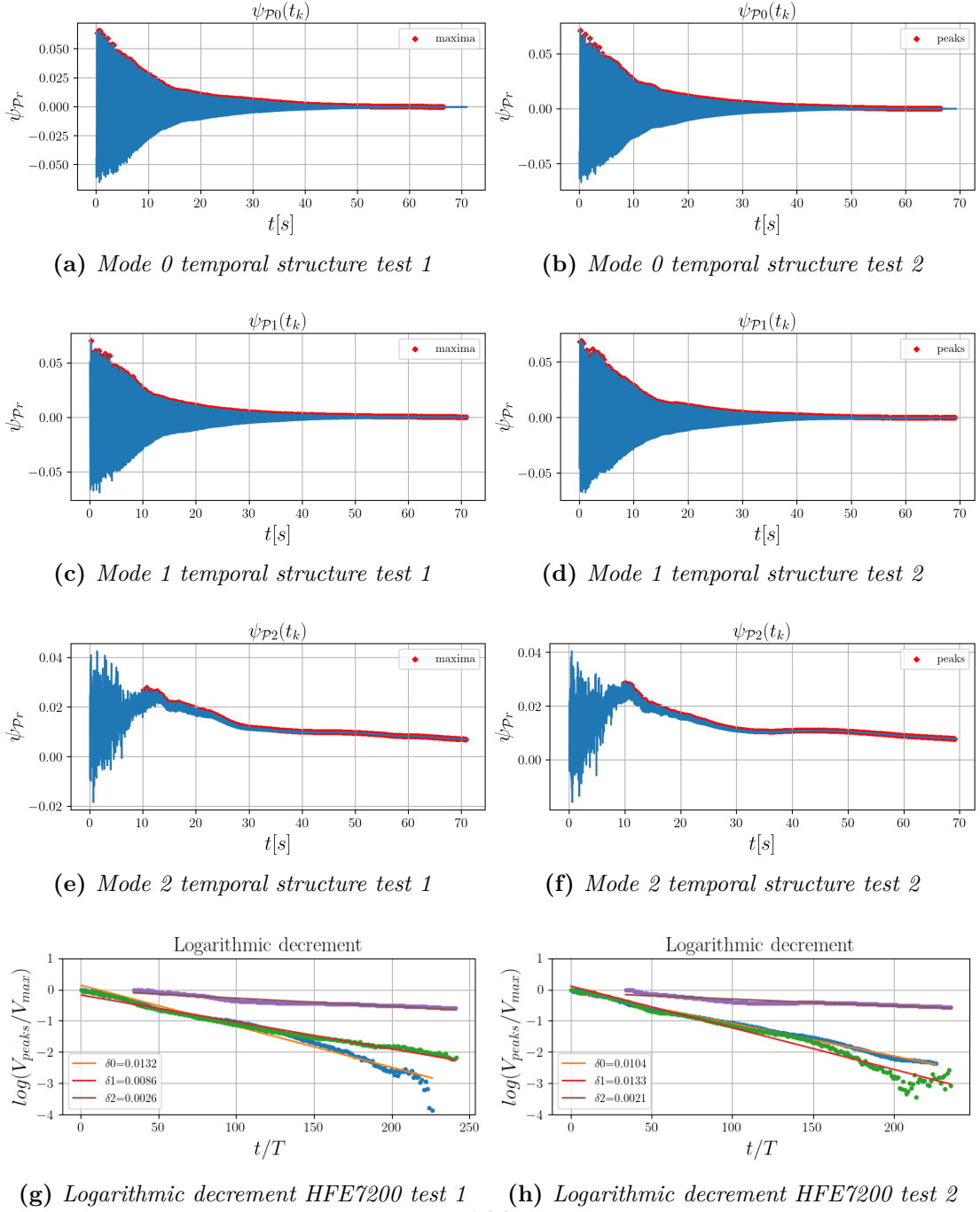


**Figure A.24:** Logarithmic decrement method. On the left HFE7200 test 1, on the right HFE7200 test 2

# Bibliography

- [1] Paul Fjeld. *The First Lunar Landing*. URL: <https://www.hq.nasa.gov/alsj/a11/a11.landing.html>. (accessed: 01.09.2016) (cit. on p. 1).
- [2] Space Launch Report. *Emeraude VE121 Data Sheet*. URL: <http://www.astronautix.com/e/emeraudeve121.html>. (accessed: 01.09.2016) (cit. on p. 1).
- [3] Space Launch Report. *Jupiter AM-1 Falcon Data Sheet*. URL: <http://www.astronautix.com/j/jupiterirbm.html>. (accessed: 01.09.2016) (cit. on p. 2).
- [4] Space Launch Report. *SpaceX Falcon Data Sheet*. URL: <https://www.space-launchreport.com/falcon.html>. (accessed: 01.09.2016) (cit. on p. 2).
- [5] John L. Sewall. *An experimental and theoretical study*. Tech. rep. 4166. Washington: NACA, Dec. 1957 (cit. on p. 2).
- [6] B. W. Graham and A. M. Rodriguez. *The characteristics of fuel motion which affect airplane dynamics*. Tech. rep. SM-14212. Santa Monica: Douglas, Nov. 1951 (cit. on p. 2).
- [7] Helmut F. Bauer. *Fluid oscillations in the containers of a space vehicle and their influence upon stability*. Huntsville, Alabama: NASA, 1964 (cit. on p. 3).
- [8] H. N. Abramson. *The Dynamic Behavior of Liquids in Moving Containers, with Applications to Space Vehicle Technology*. Special Publication (SP) NASA-SP-106. Washington, D.C.: NASA, 1966 (cit. on pp. 3, 10, 13).
- [9] John W. Miles. «Resonantly forced surface waves in a circular cylinder». In: *J. Fluid Mech.* 149 (May 1984), pp. 15–31 (cit. on pp. 3, 5).
- [10] John W. Miles. *On the sloshing of liquid in a cylindrical tank*. Tech. rep. AM 6-5. The Ramo-Wooldridge Corporation, 1956 (cit. on pp. 3, 4, 7).
- [11] D. G. Stephens and H. W. Leonard an T. W. Perry. *Investigation of the Damping of Liquids in Right-Circular Cylindrical Tanks Including the Effects of a Time-Variant Liquid Depth*. Tech. rep. TN D-1367. Washington, D.C.: NASA, 1962 (cit. on p. 4).

- [12] T. Mieda, K. Ishida, K. Jitu, and T. Chiba. «An experimental study of viscous damping in sloshing mode of cylindrical tanks». In: *SMiRT 12* (1993), pp. 231–236 (cit. on p. 4).
- [13] K. M. Case and W. C. Parkinson. «Damping of surface wave in an incompressible liquid». In: *J. Fluid Mech.* 2 (Mar. 1957), pp. 172–184 (cit. on p. 4).
- [14] H. N. Abramson and L. R. Garza. «Liquid frequencies and damping in compartmented cylindrical tanks». In: *J. Spacecr. Rockets* 2 (May 1965), pp. 453–455 (cit. on p. 4).
- [15] M. Utsumi. «Theoretical determination of modal damping ratio of sloshing using a variational method». In: *Journal of Vessel Pressure Technology Fluid* 133.011301 (Feb. 2011), pp. 1–10 (cit. on pp. 4, 11).
- [16] H. F. Bauer and W. Eidel. «Free oscillations and response of a viscous liquid in a right cylindrical container». In: *Aerosp. Sci. Technol.* 3 (Nov. 1999), pp. 495–512 (cit. on p. 4).
- [17] H. F. Bauer and M. Chiba. «Viscous oscillations in a circular cylindrical tank with elastic surface cover». In: *J. Sound Vib.* 303 (Jan. 2007), pp. 1–17 (cit. on p. 4).
- [18] H. F. Bauer and K. Komatsu. «Vibration of a hydroelastic system consisting of a sector shell and viscous liquid in zero gravity». In: *J. Fluids Struct.* 12 (Apr. 1998), pp. 367–385 (cit. on p. 4).
- [19] G. M. Horstmann, W. Herreman, and T. Weier. «Linear damped interfacial wave theory for an orbitally shaken upright circular cylinder». In: *J. Fluid Mech.* 891 (Feb. 2020), A22 1–A22 35 (cit. on p. 4).
- [20] X. Zheng, H. Zhang, Y. Ren, Ze-hongWei, and X. Song. «Rollover stability analysis of tank vehicles based on the solution of liquid sloshing in partially filled tanks». In: *Advances in Mechanical Engineering* 9(6) (Mar. 2017), pp. 1–26 (cit. on p. 5).
- [21] L. F. B. Martinez, R. Palma, F. Gomez, D. Vaishnav, and F. Canales. *High Frequency Sloshing - Energy Dissipation and Viscous Damping through CFD*. Tech. rep. 2017-01-1317. SAE International, Mar. 2017 (cit. on p. 5).
- [22] A. Simonini, L. Peveroni, and M. R. Vetrano. «Simultaneous interface position and bulk velocity measurements in cryogenic sloshing». In: *Aerospace Science and Technology* 90 (Apr. 2019), pp. 452–462 (cit. on pp. 5, 28).
- [23] R. A. Ibrahim. *Liquid sloshing dynamics*. Cambridge University Press, 2005 (cit. on p. 7).
- [24] M. C. Ruzicka. «On dimensionless numbers». In: *Chemical Engineering Research and Design* 86 (Mar. 2008), pp. 835–868 (cit. on p. 21).

- [25] A. Simonini, M. R. Vetrano, P. Colinet, and P. Rambaud. «Particle Image Velocimetry applied to water sloshing due to a harmonic external excitation». In: *17<sup>th</sup> International Symposium on Application of Laser Techniques to Fluid Mechanics*. Lisbon, Portugal, 2014 (cit. on p. 39).
- [26] M. A. Mendez, M. Balabane, and J.-M. Buchlin. «Multi-scale proper orthogonal decomposition of complex fluid flows». In: *J. Fluid Mech.* 870 (Mar. 2019), pp. 988–1036 (cit. on p. 48).
- [27] Miguel A. Mendez. «Statistical Treatment , Fourier and Modal Decompositions». In: *Fundamentals and Recent Advances in Particle Image Velocimetry and Lagrangian Particle Tracking , VKI Lecture Series*. Ed. by S. Discetti and M. A Mendez. von Karman Institute, 2021. ISBN: 978 -2 -87516 -181 -9 (cit. on p. 50).